LBL--29485

DE91 001806

Measurement of the Z-Boson Branching Fraction into Hadrons Containing Bottom Quarks

J. Frederic Kral

(Ph. D. Thesis)

Department of Physics
University of California

and

Physics Division
Lawrence Berkeley Laboratory
University of California
One Cyclotron Road
Berkeley, CA 94720

September 1990

MASTER

This work was supported by the Director, Office of Energy Research, Office of High Energy and Nuclear Physics, Division of High Energy Physics, of the U. S. Department of Energy under Contract No. DE-AC03-76SF00098.

DISTRIBUTION OF THIS DOCUMENT IS UNLIMITED

Measurement of the Z-Boson Branching Fraction into Hadrons Containing Bottom Quarks

J. Frederic Kral

(Ph. D. Thesis)

September 5, 1990

Abstract

We use the Mark II detector to study Z decays into bottom quark–anti-quark pairs, leading to the production of bottom hadrons. The Z bosons are formed in e^+e^- annihilation at the SLC at center-of-mass energies between 89 and 93 GeV. We identify events containing semileptonic decays of bottom hadrons by detecting isolated leptons, i.e. leptons with high transverse momenta relative to the nearest hadronic jet. Using isolated electrons and muons, we measure the B-hadron semileptonic branching ratio times the fraction of hadronic Z decays which contain bottom hadrons,

$$B(B \to Xl\nu) \cdot \frac{\Gamma(Z \to b\bar{b})}{\Gamma(Z \to \text{had})} = 0.025^{+0.010}_{-0.009} \pm 0.005,$$

where we have listed the statistical errors followed by the systematic error. Assuming $B(B \to Xl\nu) = 11\% \pm 1\%$, we measure $\Gamma(Z \to b\bar{b})/\Gamma(Z \to \text{had}) = 0.23^{+0.11}_{-0.09}$, in good agreement with the standard-model prediction of 0.22. We find $\Gamma(Z \to b\bar{b}) = 0.40^{+0.19}_{-0.16}$ GeV.

[redacted]

This work was supported by the United States Department of Energy under Contract No. DE-AC03-76SF00098.

To the memories

of

my Grandfathers

FARFAR HANS och MORFAR SVEN-GÖSTA

and

to their beliefs

in

Education

Ten Commandments

by Leo Szilard

1. *Recognize the connections of things and the laws of conduct of people, so that you may know what you are doing.*
2. *Let your actions be directed towards a worthy goal, but do not ask if they will reach it; they are models and examples, not means to an end.*
3. *Speak to all people as you do to yourself, with no concern for the effect you make, so that you do not shut them out from your world; lest in isolation the meaning of life slips out of sight and you lose belief in the perfection of the creation.*
4. *Do not destroy what you cannot create.*
5. *Do not eat unless you are hungry.*
6. *Do not covet what you cannot have.*
7. *Do not lie without need.*
8. *Honor children. Listen reverently to their words and speak to them with infinite love.*
9. *Do your work for six years; but in the seventh, go into solitude or among strangers, so that the recollection of your friends does not hinder you from being what you have become.*
10. *Lead your iife with a gentle hand and be ready to leave whenever you are called.*

Acknowledgements

THANKS to my thesis advisor, George Trilling, for taking personal interest in my work, for asking probing questions, for offering positive guidance, for masterfully steering me away from pitfalls, for being willing to let a five-minute meeting turn into a two-hour physics discussion and for patiently editing hundreds of pages of my often obscure prose into clear scientific discourse.

THANKS to the other members of my thesis committee, John Rasmussen and Jim Siegrist, for reading and improving this thesis.

THANKS to my teachers, Fred Levine, Howard Georgi and Larry Hall, for inspiring courses at Mamaroneck Public High School, Harvard University and U.C. Berkeley, respectively. Thanks to Jim Rohlf for starting me out in particle physics by sending me from comfy Harvard to crazy UA1 at CERN.

THANKS to my colleagues, Gerry Abrams, Siggi Bethke, Gary Feldman, Gerson Goldhaber, Chris Hearty, Mike Levi, Sven-Olof Holmgren, René Ong, Rick Van Kooten, Markus Schaad, Andrew Weir and Darien Wood for invaluable advice, help and friendship throughout the years. Thanks to Bill Ford, Don Fujino, Ken Hayes, John Jaros, Bruce Schumm, Steve Wagner and Paul Weber for teaching me Zen and the art of vertex chamber maintenance. Thanks to all the members of the Mark II for making it a pleasant learning environment as well as an exciting physics experiment.

THANKS to my good friend and fellow student, Storrs Hoen, for the recurrently fun physics discussions, perennially tasty Thursday dinners and continually warm friendship since our first day of graduate school. Thanks to my fellow students, Jayme De Luca and Jaipal Tuttle, for inspiration inside and outside school. Thanks to my good bud, Mike Samols, for crunchy chow, literate letters, super skiing, tonar trips and waynar windsurfing. Thanks to Jonas Davidsson, Nicole Gallagher and Brian

Kenet for enduring bonds across the globe. Thanks to Whitney Davis for adventure, brilliance and companionship. Thanks to Atessa Chehrazi for providing love and a home away from 'home.' Thanks to Beth Grossman for peaceful walks and genuine understanding. Thanks to everyone else who contributed to my four excellent years in the Bay Area.

THANKS to my friends at 1838 San Juan in Berkeley—especially warmly to Danny, Hilary and Josh Goldstine, George Putris and Nancy Schneider—for food, housing, movies, parties, swims and videos; for Christmas 1989 and each Thanksgiving dinner; for sharing the ups and the downs; and for offering lots of loving support.

THANKS to my parents and brother, Mamma, Pappa och Alex, for encouragement along the way. The journey leading to this thesis would not have been completed without you.

Contents

Abstract iii

Dedication v

Quotation vii

Acknowledgements ix

1 Introduction 1

1.1 Theoretical Background 2

1.1.1 Electroweak Couplings 2

1.1.2 $b\bar{b}$ Production in e^+e^- Annihilation 5

1.2 Experimental Method 7

2 The Mark II Detector at the SLC 11

2.1 SLAC Linear Collider 11

2.2 Mark II Detector 11

2.3 Central Drift Chamber 15

2.4 Time-of-Flight System 16

2.5 Mark II Solenoid 16

2.6 Liquid Argon Barrel Calorimeter 17

2.7 Endcap Calorimeter 18

2.8 Muon System 19

2.9 Luminosity Monitors 21

2.9.1 Small-Angle Monitor 21

2.9.2 Mini-Small-Angle Monitor 22
2.10 Extraction Line Spectrometer 23
2.11 Trigger and Data Acquisition Systems 24
2.12 Vertex Detectors 27
2.12.1 Silicon Strip Vertex Detector 27
2.12.2 Drift Chamber Vertex Detector 28

3 Monte Carlo Simulation **31**
3.1 QCD and Fragmentation Models 32
3.1.1 Hadronic Z-Decay Simulations 35
3.2 Heavy-Quark Fragmentation 36
3.2.1 Experimental Determination of Mean z 37
3.2.2 Heavy Quarks in Z Decays 39
3.3 B Decays 40
3.3.1 Measurements of Leptons from B Decay 42
3.3.2 Simulation of B Decay 45
3.4 Sources of Leptons in Hadronic Z Decays 45
3.5 Detector Simulation 46

4 Hadronic Z Decays **47**

5 Inclusive Lepton Analysis **51**
5.1 Track Isolation Criterion 51
5.2 Electron Identification 53
5.2.1 Method for Identifying Electrons 55
5.2.2 Calibration of the Electron Algorithm 56
5.2.3 Electron Identification Efficiency 58
5.2.4 Electron Misidentification Probability 59
5.3 Muon Identification 61
5.3.1 Method for Identifying Muons 61
5.3.2 Calibration of the Muon Algorithm 63
5.3.3 Muon Identification Efficiency 67

5.3.4 Muon Misidentification Probability 68

6 Branching Fraction to B Hadrons **75**

6.1 Event tagging efficiencies 75

6.2 r_b and $B(B \to Xl\nu) \cdot r_b$ 76

6.3 $\Gamma(Z \to b\bar{b})$, v_b and $B(Z \to b\bar{b})$ 78

7 Conclusion **79**

7.1 Measurements with Isolated Leptons 79

7.2 Mark II Vertex Tagging 81

A Muon Monte Carlo Corrections **89**

B Solving for the $b\bar{b}$ fraction **95**

C The Bottom-quark Cross Section **97**

C.1 Cross Section for $e^+e^- \to Z \to b\bar{b}$ 97

C.2 Measuring $\sigma_{\max}(Z \to b\bar{b})$ 98

Bibliography **101**

List of Tables

1.1 Properties of fundamental particles 3
1.2 Standard-model widths for Z decay 5
2.1 Liquid argon calorimeter strips 18
2.2 Muon system absorber geometry 21
3.1 Monte Carlo model parameters 36
3.2 $B(B \to Xl\nu)$ measurements at CESR and DORIS 44
3.3 $B(B \to Xl\nu)$ measurements at PEP and PETRA 45
4.1 Numbers of hadronic Monte Carlo events 49
5.1 Angular error in reconstructing parent hadron direction 52
5.2 Electron identification road widths 56
5.3 Median E/p for PEP Bhabha electrons 57
5.4 Numbers of MC tracks identified as electrons 59
5.5 Results of fit for muon-chamber resolution errors 65
5.6 Muon-chamber efficiency calculation 68
5.7 Numbers of MC tracks identified as muons 69
5.8 Probabilities for tracks to reach each muon system layer 70
6.1 Numbers of tagged Monte Carlo events 76
6.2 Predicted composition of tagged events 76
7.1 $B(B \to Xl\nu) \cdot r_b$ measurements at SLC and LEP 80
A.1 Fits for muon system punch-through probabilities 92
A.2 Correction of the predicted muon hit distribution 93
C.1 Measured luminosity and calculated cross section 99

List of Figures

1.1 Simple Feynman diagram 4
1.2 Leading diagram for e^+e^- annihilation 6
2.1 SLAC Linear Collider 12
2.2 Mark II detector 14
2.3 Central drift chamber cell geometry 15
2.4 LA channel ganging scheme 19
2.5 Angular coverage of calorimeters 20
2.6 Cross section of a muon module 20
2.7 Small-angle monitor module 22
2.8 Mini-small-angle monitor geometry 23
2.9 Extraction line spectrometer 23
2.10 Phosphorescent screen monitor 24
2.11 Charged particle trigger 26
2.12 Silicon strip vertex detector 28
2.13 Drift chamber vertex detector 29
3.1 Bottom-quark fragmentation in e^+e^- annihilation 33
3.2 Parton shower evolution 34
3.3 Peterson fragmentation function 38
3.4 Fragmentation variables 40
3.5 Spectator model B decay 41
3.6 Electron and muon momentum spectra from B meson decay 43
4.1 Hadronic and Leptonic Z-decay events 48
5.1 Electron p_t from decays of bottom and charm hadrons 53
5.2 The p_t for all tracks considered for lepton identification 54

5.3 Ratios E/p for PEP Bhabha electrons 57
5.4 Electron identification variables for Bhabha electrons 58
5.5 Electron identification variable in hadronic data and MC 60
5.6 The p_t spectrum for identified electrons 61
5.7 Hadronic Z-decay event with an isolated electron 62
5.8 Cosmic-ray muon hit-to-track distances 65
5.9 Cosmic-ray muon hit-correlation deviations 66
5.10 Muon identification variable in hadronic data and MC 71
5.11 The p_t spectrum for identified muons 72
5.12 Hadronic Z-decay event with an isolated muon 73
6.1 The p_t spectrum for lepton-tagged events 77
7.1 Vertex-tagged hadronic Z-decay event 83
7.2 Lepton-tagged hadronic Z-decay event 86
A.1 Result of fit for hadron punch through to pattern of muon hits 91
C.1 The radiatively corrected cross section 98

Measurement of the Z-Boson Branching Fraction into Hadrons Containing Bottom Quarks

Chapter 1

Introduction

Over the past 20 years, a great number of experimental discoveries have contributed to vast improvements in our theoretical understanding of particle physics. The experimental observations of neutral currents [Hasert 73], the charm quark [Aubert 74, Augustin 74], the third generation tau lepton [Perl 75] and bottom quark [Herb 77], electroweak interference [Prescott 78], the intermediate vector bosons $W^{\pm}$ [Arnison 83a, Banner 83] and Z [Arnison 83b, Bagnaia 83], and the absence of a light fourth generation neutrino [Abrams 89d, Decamp 89, Aarnio 89, Adeva 89, Akrawy 89], are important ingredients of the standard model of particle interactions. Experimental studies of Z decays can further probe the standard model of electroweak interactions between three generations of fermions [Glashow 61, Weinberg 67, Salam 68, Glashow 70, Weinberg 71, Weinberg 72, Kobayashi 73].

In this thesis we study Z decays to a pair of the heaviest kinematically available quarks, the bottom quarks—the first direct study of the Z coupling to a specific quark flavor. The study of these Z decays is possible through the clean formation of Z bosons in e^+e^- annihilation. We use isolated leptons produced in semileptonic bottom-hadron decays to distinguish Z decays to bottom quarks from Z decays to other flavors. The leptons are reconstructed in the Mark II detector at the Stanford Linear Accelerator Center (SLAC).

In this chapter we use the standard model to describe the production of bottom quarks through e^+e^- annihilation. This description serves as a theoretical background to the description of the experimental method which concludes the chapter.

1.1 Theoretical Background

The standard model describes the interactions of fermions via gauge bosons, incorporating a wealth of experimental data into our current understanding of particle physics. The model encompasses the electroweak and strong interactions for three generations of leptons and quarks. The first generation of leptons contains the electron (e^-) and the electron neutrino (ν_e) and their antiparticles (e^+ and $\bar{\nu}_e$). The electron and its heavier second and third generation cousins, the muon ($\mu^\pm$) and the tau lepton ($\tau^\pm$), carry electric charge and thus interact with photons (γ), the carriers of the electric force. These leptons, as well as the neutrino in each generation, feel the weak force mediated by the massive intermediate vector bosons ($W^\pm$ and Z^0). Quarks differ from leptons in that they interact through the strong force in addition to the electric and weak forces. This is because quarks carry the attribute called color, which is exchanged by gluons (g), the carriers of the strong force. Each quark generation contains a pair of quarks with one carrying the electric charge $+\frac{2}{3}$ and the other carrying $-\frac{1}{3}$ units of the positron charge. Thus we have the up (u) and down (d) quarks in the first generation, followed by the charm (c) and strange (s) quarks in the second generation and the top (t) and bottom (b) quarks in the third generation. The particles and their properties are listed in Table 1.1. The top quark has not yet been observed: it is too heavy to be produced in Z decays [Abrams 89e] and a search for it in $p\bar{p}$ collisions excluded masses between 40 and 77 GeV/c^2 at 95% confidence level [Abe 90].

1.1.1 Electroweak Couplings

The electroweak model symmetry group is $SU(2) \times U(1)$, spontaneously broken [Weinberg 67, Salam 68] to provide mass for the three vector particles, W^+, W^- and Z^0 [Glashow 61], while leaving the γ massless. The interactions between these force carriers and the fermions are identical for each generation, so that we can focus on the first generation without losing generality. The fermions in the first generation contain both left-handed (L) and right-handed (R) fields,

$$\nu_{eL} \quad e^-_L \quad e^-_R \quad u_L \quad d_L \quad u_R \quad d_R. \tag{1.1}$$

Gauge bosons					
Type	Charge	Mass (GeV/c^2)	Type	Charge	Mass (GeV/c^2)
γ	0	$< 3 \times 10^{-36}$	Z	0	91
W	± 1	80	g	0	~ 0
Fermions					
Flavor	Charge	Mass (GeV/c^2)	Flavor	Charge	Mass (GeV/c^2)
ν_e	0	$< 17 \times 10^{-9}$	u	$+2/3$	$\sim 5.6 \times 10^{-3}$
e	-1	0.51×10^{-3}	d	$-1/3$	$\sim 9.9 \times 10^{-3}$
ν_μ	0	$< 0.27 \times 10^{-3}$	c	$+2/3$	~ 1.4
μ	-1	0.11	s	$-1/3$	~ 0.20
ν_τ	0	$< 35 \times 10^{-3}$	t	$+2/3$	> 77
τ	-1	1.8	b	$-1/3$	~ 4.7

Table 1.1: The electrical charges and masses of the particles in the standard model [Hernández 90]. Each fermion has a corresponding anti-fermion with opposite charge.

For every fermion, there is an anti-fermion with opposite electric charge and handedness. Right-handed neutrinos are omitted since there is no experimental evidence for their existence. The left-handed fields are $SU(2)$ doublets while the right-handed fields are $SU(2)$ singlets [Weinberg 67, Glashow 70]. For simplicity we have ignored the fact that for each type of quark, there are actually three quarks: one for each color, the charge of the strong interaction. Because the quarks have mass, the mass eigenstates acted upon by the strong interaction are different from the weak eigenstates. The matrix describing the rotation of left-handed quarks from mass states into weak states is chosen to operate on the charge $-\frac{1}{3}$ quarks. For three generations of quarks, the nine complex numbers in the 3×3 unitary matrix V are related such that only four parameters are required to describe the rotation—three angles and one phase in the Kobayashi and Maskawa (KM) convention [Kobayashi 73]. The first generation weak state is $d'_L = V_{ud} d_L + V_{us} s_L + V_{ub} b_L$. Thus, within the $SU(2) \times U(1)$ model, the fermions of the first generation are neatly organized as

$$\begin{pmatrix} \nu_{eL} \\ e^-_L \end{pmatrix} \quad e^-_R \quad \begin{pmatrix} u_L \\ d'_L \end{pmatrix} \quad u_R \quad d_R. \tag{1.2}$$

The electroweak model specifies how each of the four types of force-carrying boson couples to these fermions [Weinberg 71]. We picture the coupling in terms of the simple Feynman diagram in Figure 1.1, depicting a vertex with a boson, a fermion and

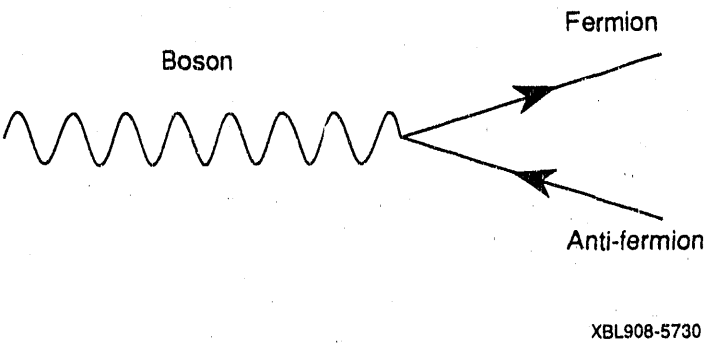

Figure 1.1: A simple Feynman diagram showing the coupling between a boson, a fermion and an anti-fermion.

an anti-fermion. The photon couples to both left-handed and right-handed fermions, with a vector coupling of strength proportional to the charge of the fermions, eQ, where Q is given in units of the positron charge. For example, photons undergoing pair-conversion in a material couple to electrons via the vertex $\gamma\, e^+\, e^-$. The charged W bosons couple to the weak charge of the left-handed doublets, with a coupling of strength $g/\sqrt{2}$. The value of the weak charge, $g = 0.65$, is calculated from the Fermi coupling constant, $G_F = \sqrt{2}g^2/8M_W^2 = 1.2\times10^{-5}$ GeV^{-2}. As an example, the W was first observed through its coupling to the electron, $W^-\, e^+\, \nu_e$. Like the photon, the Z couples to both right-handed and left-handed charged fermion–anti-fermion pairs. The coupling is $-eQ\tan\theta_W$, where the electric charge is related to the weak charge by $e = g\sin\theta_W$ and θ_W is the weak mixing angle defined by $\cos\theta_W = M_W/M_Z$. In addition to the electromagnetic force, the Z carries the neutral component of the weak force. Like the W, the Z couples to left-handed fermions, with a strength of $gT_3/\cos\theta_W$, where T_3 is the third component of weak isospin for fermions in the weak doublets. For the upper members of the doublets, $T_3 = +\frac{1}{2}$, while for the lower members, $T_3 = -\frac{1}{2}$. The coupling thus leads to Z bosons coupling to a pair of neutrinos, $Z^0\, \nu\, \bar{\nu}$, inaccessible for virtual photons.

f_i	c_{ew}	$\times$	c_s	$\times$	n_c	$\times$	Γ_0	$=$	Γ_i	Γ_{L+R}
ν_L	0.25	$\times$	1	$\times$	1	$\times$	0.6629	$=$	0.166	0.166
e_L	0.0729	$\times$	1	$\times$	1	$\times$	0.6629	$=$	0.048	
e_R	0.0529	$\times$	1	$\times$	1	$\times$	0.6629	$=$	0.035	0.083
u_L	0.1202	$\times$	1.039	$\times$	3	$\times$	0.6629	$=$	0.248	
u_R	0.0235	$\times$	1.039	$\times$	3	$\times$	0.6629	$=$	0.049	0.297
d_L	0.1792	$\times$	1.039	$\times$	3	$\times$	0.6629	$=$	0.370	
d_R	0.0059	$\times$	1.039	$\times$	3	$\times$	0.6629	$=$	0.012	0.383

Table 1.2: The standard-model partial widths in GeV for Z decay to pairs of fermions in the first generation. The partial width $\Gamma_i = c_{ew} c_s n_c \Gamma_0$, where $c_{ew} = (T_3 - Q \sin^2\theta_W)^2$ is the electroweak coupling using $\sin^2\theta_W = 0.230$ [Cahn 90], $c_s = 1 + \alpha_s/\pi$ is the first-order strong-interaction correction for quarks using $\alpha_s = 0.124$ [Akrawy 90, Komamiya 90], n_c is the number of quark colors and $\Gamma_0 = G_F M_Z^3/3\sqrt{2}\pi$ is calculated using $G_F = 1.166 \times 10^{-5}$ GeV^{-2} and $M_Z = 91.17$ GeV$/c^2$ [Fernandez 90]. The predicted total width is 2.49 GeV, with 1.74 GeV coming from the five accessible quarks u, d, s, c and b.

Using these couplings, we calculate the Z-boson partial widths and branching fractions predicted by the standard model. The partial width for Z decay into a left-handed fermion–anti-fermion pair is

$$\Gamma(Z \to f_L \bar{f}_R) = \frac{M_Z}{24\pi}\left(\frac{gT_3}{\cos\theta_W} - eQ\tan\theta_W\right)^2 = \frac{G_F}{\sqrt{2}}\frac{M_Z^3}{3\pi}(T_3 - Q\sin^2\theta_W)^2. \quad (1.3)$$

The width into a right-handed pair is obtained with $T_3 = 0$. Table 1.2 lists the predicted standard-model widths for Z decay into the first-generation fermions (Equation 1.2). When these partial widths are divided by the total width for Z decay to all three generations of fermions in Table 1.1, $\Gamma_Z = 2.5$ GeV, we get the predicted Z-boson branching fractions of 6.7% for $\nu\bar{\nu}$, 3.4% for e^+e^-, 11.9% for $u\bar{u}$ and 15.4% for $d\bar{d}$.

1.1.2 $b\bar{b}$ Production in e^+e^- Annihilation

With the theory of the electroweak model described above, we investigate the final states resulting from e^+e^- annihilation. An electron and a positron annihilate into a

combination of the two accessible states, a virtual photon and Z, as shown schematically in Figure 1.2. At energies below the 91-GeV/c^2 Z mass [Abrams 89a], the

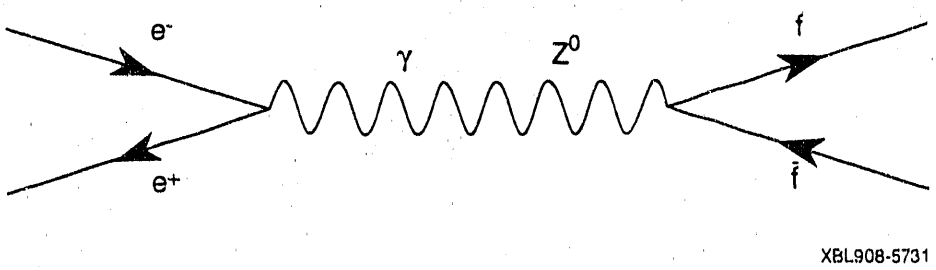

Figure 1.2: Leading Feynman diagram for e^+e^- annihilation to a fermion–anti-fermion pair.

influence of the Z boson on the rate of production of final-state particles diminishes with decreasing e^+e^- center-of-mass energy.

Thus, at the center-of-mass energy of the SLAC storage ring PEP, $E_{\rm cm} = 29$ GeV, the rate of fermion pair production is almost entirely characterized by single photon exchange. As a common yardstick for comparisons, we express the rates of particle production through e^+e^- annihilation in terms of the point cross-section for muon pair production,

$$\sigma_{\rm pt} = \frac{4\pi\alpha^2}{3s}, \tag{1.4}$$

where α is the fine structure constant $e^2/4\pi = 1/137$ and $s = {E_{\rm cm}}^2$ is the square of the center-of-mass energy. Each factor of α results from one of the two vertices of the interaction. Since the rate is proportional to the square of the electric charge of the final state fermions, it is now simple to calculate the rate of quark production,

$$R = \frac{\sigma(e^+e^- \to {\rm had})}{\sigma_{\rm pt}} \approx 3\sum_q Q_q^2, \tag{1.5}$$

where the factor 3 arises from the sum over the colors of the final-state quark–anti-quark pairs, and where we have ignored corrections for strong and weak interactions. Experimentally we do not detect free quarks, since quarks are confined by the strong interaction into color-singlet states, hadrons. For the five quarks that are currently accessible in e^+e^- annihilation experiments, u, d, s, c and b, the predicted rate

$R \approx 11/3$. The expected fraction of hadronic final states which come from $b\bar{b}$ quarks is approximately

$$f_b = \frac{1^2}{2^2 + 1^2 + 1^2 + 2^2 + 1^2} = \frac{1}{11} = 0.091. \tag{1.6}$$

At energies near the peak of the Z resonance, the rates of particle production from e^+e^- annihilation are described by the radiatively corrected Breit-Wigner Z^0 line shape.* Near the peak of the Z, the quarks produced in e^+e^- annihilation come predominantly from Z^0 exchange. This is illustrated by the large value of R at the Z mass,

$$R = \frac{9}{\alpha^2} B(Z \to e^+e^-) B(Z \to \text{had}) \times \delta = 4000 \times 0.74 = 2900, \tag{1.7}$$

where the branching fractions used are the standard-model values from page 5 in Section 1.1.1, and where the factor δ is the substantial correction due to initial-state radiation from Section C.1. We calculate the fraction of hadronic Z decays which contain bottom hadrons from the neutral-current coupling constants of the electroweak model. The rates of production of quarks are proportional to the sums of the squares of the relevant vector and axial coupling constants. At tree level, single photon exchange has a vector coupling proportional to Q while Z^0 exchange has an axial coupling $a = 2T_3$ and a vector coupling $v = 2T_3 - 4Q\sin^2\theta_W$. With $\sin^2\theta_W = 1 - M_W^2/M_Z^2 = 0.23$ [Abe 89a, Abe 89b], these couplings result in $a^2 + v^2 = 1.48$ for charge $-\frac{1}{3}$ quarks and $a^2 + v^2 = 1.15$ for charge $+\frac{2}{3}$ quarks. The expected $b\bar{b}$ fraction is approximately

$$r_b = \frac{1.48}{1.15 + 1.48 + 1.48 + 1.15 + 1.48} = \frac{1.48}{6.74} = 0.22. \tag{1.8}$$

Thus, the standard model predicts that the bottom-quark fraction in hadronic events produced through e^+e^- annihilation is considerably larger near the Z peak than at lower energies.

1.2 Experimental Method

The Mark II detector at the SLAC Linear Collider (SLC) is the first experiment to study Z boson production from e^+e^- annihilation [Abrams 89a], and to study the

*Figure C.1 is a plot of the Z^0 line shape, $\sigma(E_{\text{cm}})$ (Equation C.5).

hadronic decays of the Z [Abrams 89c]. The study of leptons in hadronic Z decays recorded with the Mark II detector at the SLC is an opportunity to understand the sources of leptons at this high energy and to measure the coupling of Z bosons to b quarks. In the absence of sources of leptons from new physics, such as new heavy quarks, we use the leptons to measure the fraction of $b\bar{b}$ events in hadronic Z decays, $r_b = \Gamma(Z \to b\bar{b})/\Gamma(Z \to \text{had})$.

The signals from bottom quarks recorded in the detector come from the decay products of bottom hadrons; hence the experimental task is to use these decay products to find a signal, to relate it to the original Z decay process and to estimate backgrounds to the signal.

Hadronic events produced in e^+e^- annihilation consist of jets of hadrons, with a small fraction of leptons that are products of weak decays of hadrons. A signal for heavy quarks, first used by the Mark II experiment at the PEP storage ring [Nelson 83a], is the presence of leptons having high transverse momenta with respect to the directions of the hadronic jets, which approximate the directions of the parent b quarks. The relatively large mass of the b quark results in higher transverse momenta of leptons in b jets than in $udsc$ jets.

To relate the lepton transverse momentum spectra to the parent b quarks, we need to understand both the strong interactions responsible for turning b quarks into B hadrons and the weak interactions responsible for the semileptonic decay of B hadrons. The strong interactions are described by models which simulate the production of quarks and gluons and their subsequent fragmentation into hadrons. The parameters of these models are tuned to data from e^+e^- experiments at the PEP storage ring and at the PETRA storage ring located at the German laboratory DESY. The semileptonic weak decays of B hadrons are simulated using data from e^+e^- experiments at the CESR storage ring located at Cornell University and at the DORIS storage ring located at DESY.

Electrons and muons are identified in the Mark II detector with algorithms designed using samples of known leptons. Using a simulation of the response of the detector to different types of particles, which incorporates data taken with the Mark II at the PEP storage ring, we estimate the efficiencies for identifying real leptons, and

the efficiencies for misidentifying hadrons as leptons.

We extract r_b from a sample of $b\bar{b}$ events tagged with isolated leptons, defined to be leptons having high transverse momenta with respect to the nearest jet formed by the other particles in the event. For this measurement we count the number of hadronic events observed and the number of these events tagged by an isolated lepton. We determine r_b from these numbers and the respective efficiencies for observing $udsc$ and $b\bar{b}$ events in the hadronic event sample as well as the tagged subsample. Since we tag bottom hadrons with leptons, we measure the product of the B-hadron semileptonic branching ratio and the $b\bar{b}$ fraction in hadronic Z decays, $B(B \to Xl\nu) \cdot r_b$. Using the value for r_b, we estimate the Z-boson partial width $\Gamma(Z \to b\bar{b})$, vector coupling constant v_b and branching fraction into bottom hadrons $B(Z \to b\bar{b})$.

In the following chapter, we describe the apparatus used, the Mark II detector at the SLC. Chapter 3 describes the Monte Carlo (MC) simulation of the data, including models for fragmentation and B decays and the simulation of signals in the detector. The efficiencies for selecting hadronic events are computed in Chapter 4. We then turn to leptons produced in hadronic events in Chapter 5. After a description of our track isolation criterion, we show the methods for identifying electrons and muons and for estimating the backgrounds. In Chapter 6, we calculate the efficiencies for tagging bottom-quark events with isolated leptons. We then determine r_b, $B(B \to Xl\nu) \cdot r_b$, $\Gamma(Z \to b\bar{b})$, v_b, $B(Z \to b\bar{b})$ and the errors on these quantities. Finally, in Chapter 7, we summarize other measurements of the $Z \to b\bar{b}$ coupling constants, including the recent measurements by experiments at the LEP storage ring located at the European Laboratory for Particle Physics (CERN), and indicate future directions for further study of bottom quarks produced in Z decay. As an example, we show data recorded with the Mark II vertex detectors, which tag bottom hadrons by virtue of their long lifetimes.

Chapter 2

The Mark II Detector at the SLC

2.1 SLAC Linear Collider

The e^+e^- collisions recorded with the Mark II detector were produced with the SLAC Linear Collider (SLC). As a single-pass electron positron collider, the SLC is the first accelerator of its kind. The paths of the electron and positron bunches are illustrated in Figure 2.1. After accelerating along the 2-mile-long linear accelerator, the electron bunch and the positron bunch, each containing about 10^{10} particles, travel separately into either of the two 1-km arches. The bunches are focussed to rms radii of about 3 μm at the interaction point, where they collide inside the Mark II and then travel to beam dumps. Positrons are produced by a third bunch, the electron scavenger bunch, which collides with a target after being accelerated down most of the linear accelerator. The collision rate was 60 Hz during most of the 1989 run. The rate was increased to 120 Hz in January 1990 by accelerating the scavenger bunch in the same cycle as the electron and positron bunches. The luminosity during the last months of data-taking during 1989 was typically 1×10^{28} cm^{-2}s^{-1}, corresponding to the production of about one Z^0 per hour at the peak.

2.2 Mark II Detector

The Mark II detector is a general purpose magnetic detector for the study of e^+e^- collisions, modelled after the Mark I SLAC-LBL Magnetic Detector at the SPEAR

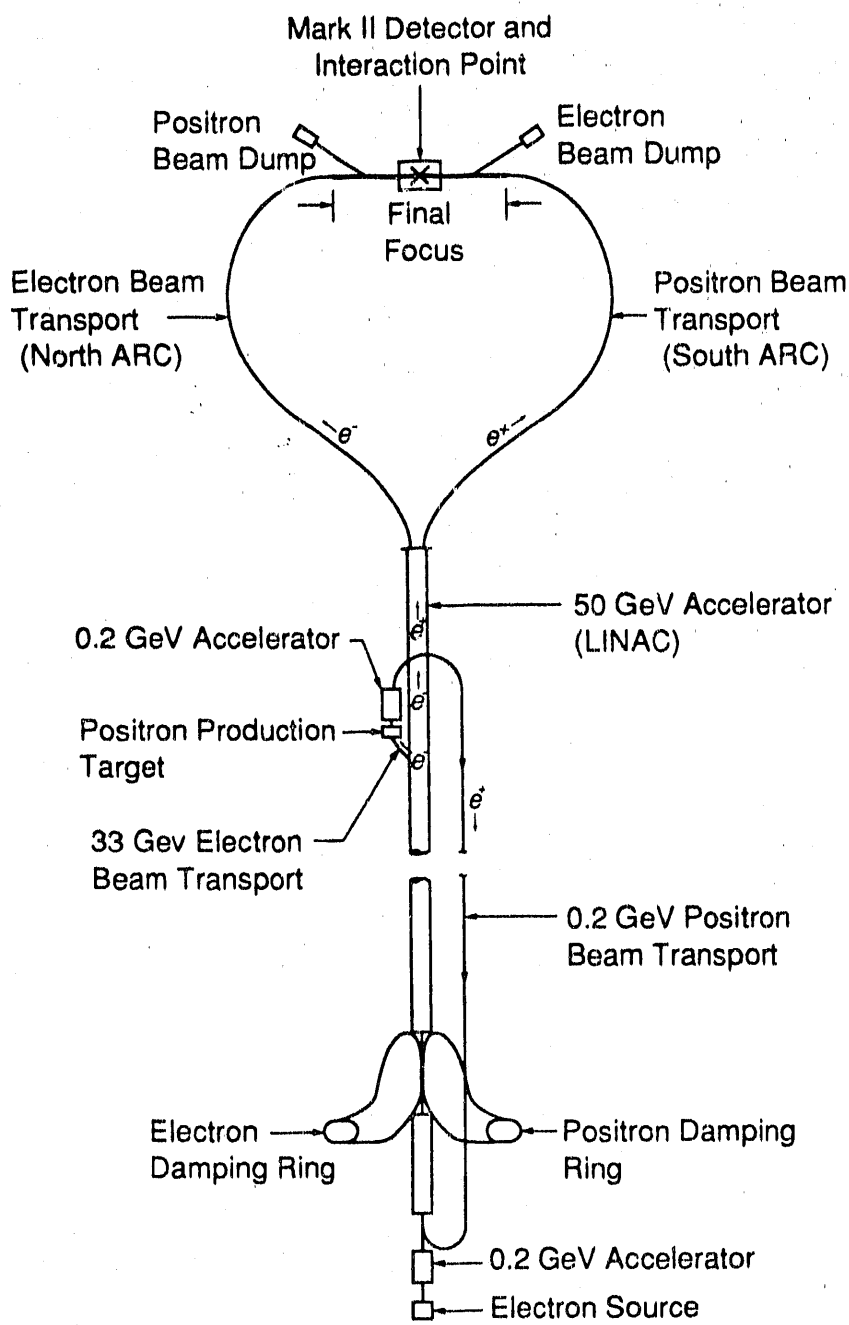

Figure 2.1: Schematic layout of the SLAC Linear Collider.

storage ring. During the years 1978 and 1979, the Mark II was used at SPEAR for e^+e^- collisions produced with center-of-mass energies between 3 and 7 GeV. The Mark II was then moved to the PEP storage ring, where it recorded 205 pb^{-1} of data at the energy of 29 GeV between the years 1981 and 1984. In preparation for SLC data-taking, the Mark II was upgraded and subsequently run at PEP during the Fall and Winter of 1985–86, accumulating an additional 30 pb^{-1} of data. We shall refer to this PEP data set in our analysis of Z decays recorded at the SLC since it provides important information on the performance of the upgraded detector [Abrams 89b]. During the Summer of 1986, the detector was moved to the SLC collision hall, where it was used to help monitor the commissioning of the SLC which was started during the Summer of 1987. For the measurement of the $b\bar{b}$ fraction, we use data recorded from April 1989, when the first hadronic Z decay was obtained, until November 1989, at which time 20.0 nb^{-1} had been accumulated in the energy range 89 to 93 GeV. We also show results from the 1.4 nb^{-1} of data recorded with the newly installed vertex detectors during January 1990.

The components of the Mark II detector surround the beam pipe in a cylindrical geometry as illustrated in Figure 2.2. The figure defines the Mark II coordinate system with the positive z direction along the electron beam and the y-axis pointing upwards. Moving at large angle to the beam line, in order of increasing radial distance from the beam pipe, the Mark II consists of the central drift chamber, the time-of-flight system, the solenoid magnet, the liquid argon barrel calorimeter and the muon system, whose steel serves both as hadron absorber and magnetic flux return. We describe these components as well as the endcap calorimeter, the luminosity monitors, the extraction line energy spectrometer and the trigger and data acquisition systems. All of these components were newly constructed for the upgrade of the Mark II, except for the liquid argon calorimeter, the muon system and parts of the trigger and data acquisition systems. The detector has been described in more detail elsewhere [Abrams 89b] and we emphasize here the detector elements used for lepton identification, namely the central drift chamber, the liquid argon calorimeter and the muon system. The final section of this chapter describes the vertex detectors that were added inside the central drift chamber after the 1989 run.

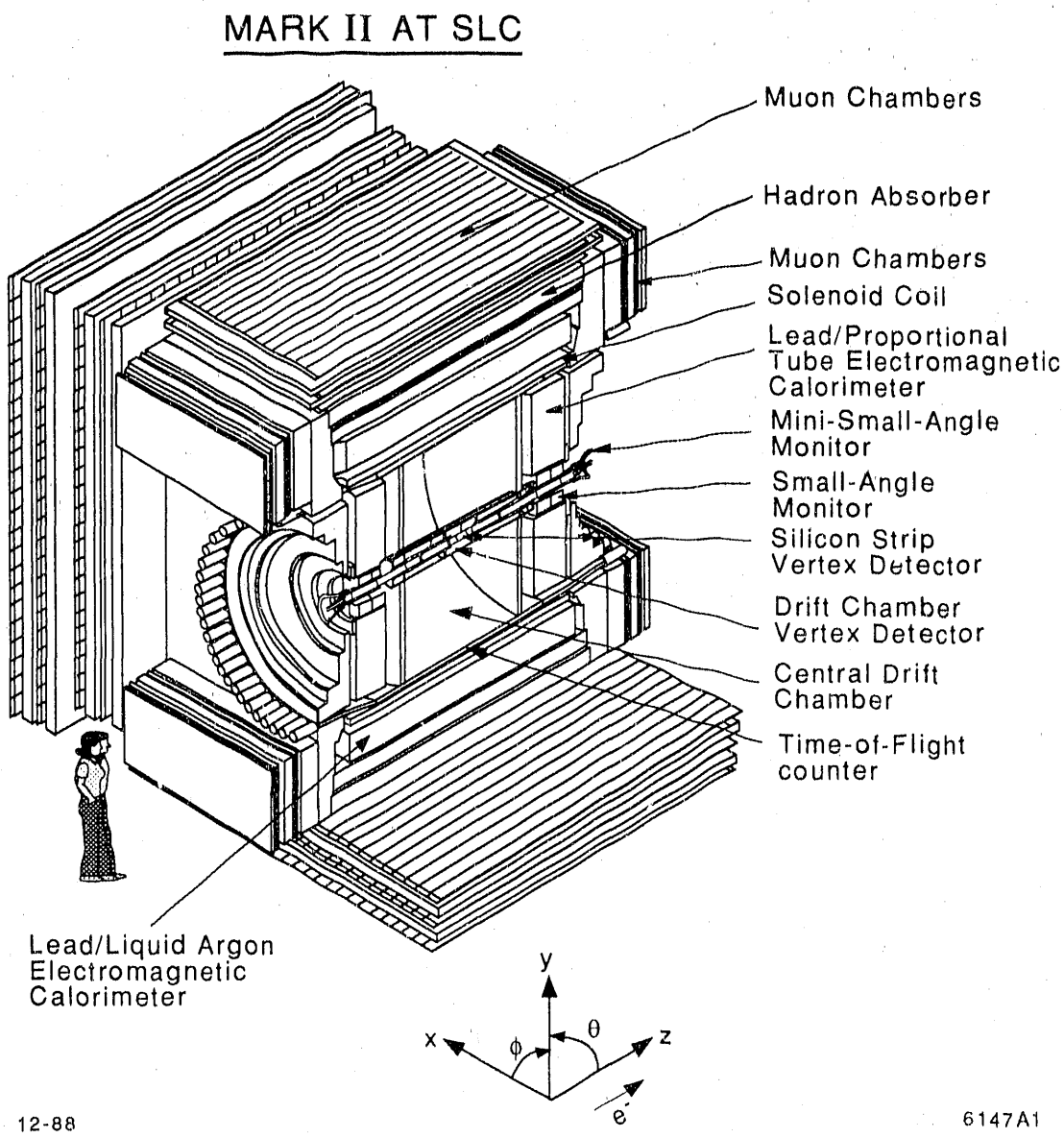

Figure 2.2: Cut-away view of the Mark II detector showing major components.

2.3 Central Drift Chamber

The central drift chamber (DC) provides pattern recognition, momentum measurement and multiple ionization energy loss measurements for charged particles in the angular region $|\cos\theta| < 0.92$, where θ is the polar angle measured with respect to the beam axis. The chamber consists of 12 cylindrical layers extending from 19 cm to 152 cm in radius, each containing between 26 and 136 sense-wire cells with the shortened jet-chamber geometry shown in Figure 2.3. The six sense wires in each

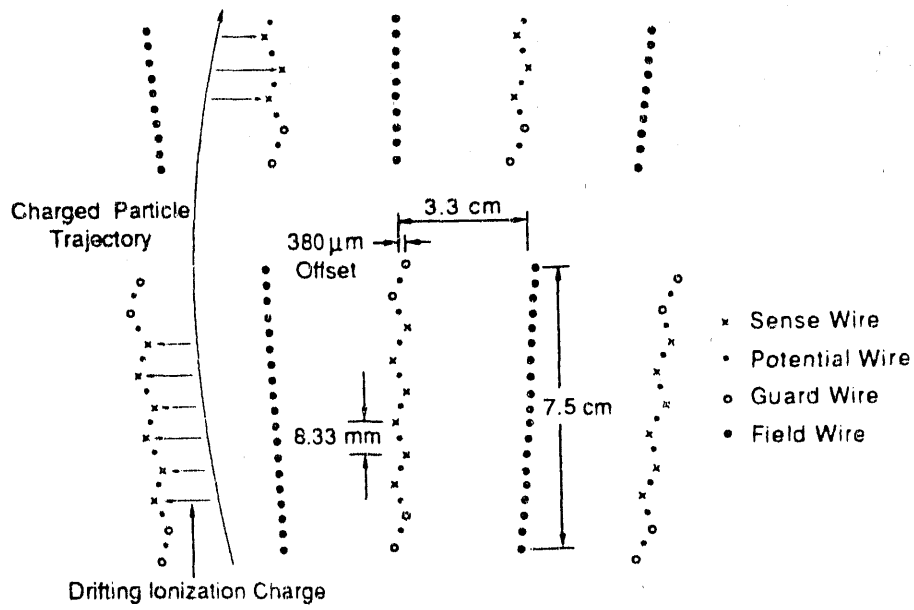

Figure 2.3: Central drift chamber cell design.

cell are staggered $\pm 380\ \mu m$ from the cell axis to resolve left-right ambiguities. The electric field between the sense and field wires is optimized by appropriate potentials on the guard and potential wires. To provide measurements of the z coordinates of tracks, the orientations of sense wires in successive layers alternate between running parallel along the z-axis (axial layers) and at $\pm 3.8°$ to it (stereo layers). The active length of the chamber is 2.30 m.

The signals from the sense wires are amplified and then digitized in two different systems of FASTBUS crates. Timing signals are sent to TDCs, which have a least count of 2 ns, while pulse shapes are recorded with Flash-ADCs, which have a least

count of 10 ns. The recorded FADC pulse shapes improve the pattern recognition and double hit separation given by the TDCs, and provide ionization loss measurements used for charged particle identification.

The chamber is operated with HRS gas (89% Ar, 10% CO_2 and 1 % CH_4) slightly above 1 atm in a magnetic field of 4.75 kG. The momentum resolution is $\sigma_p/p = 0.0046p$, where p is the momentum in GeV/c. The resolution was determined using events from the Bhabha scattering process $e^+e^- \rightarrow e^+e^-$, recorded at PEP where the beam energy was 14.5 GeV. For tracks constrained to originate from the e^+e^- interaction point, the resolution improves to $\sigma_p/p = 0.0031p$. Multiple scattering in the drift chamber contributes an additional 1.4% to the momentum resolution. The single-wire position resolution averaged over the cell width is 170 μm. The dE/dx resolution obtained from using a truncated mean of 75% of, at most, 72 charge measurements is 7.2%.

The position and momentum measurements of charged tracks in the central drift chamber are used to help identify electrons in the liquid argon calorimeter and muons in the muon system.

2.4 Time-of-Flight System

The time-of-flight system records timing information useful for reconstructing cosmic rays that monitor the detector performance and for identifying charged particles. It consists of 48 scintillator counters arranged in a cylinder of inner radius 152 cm, between the central drift chamber and the magnet coil, covering a solid angle of 70% of 4π. The timing information from the counters has an average resolution of 221 ps for PEP Bhabha events.

2.5 Mark II Solenoid

The Mark II solenoid is a conventional cylindrical coil located between the time-of-flight counters and the liquid argon calorimeter modules. The conductor is aluminum, 1.3 radiation lengths thick, extending from 156 cm to 171 cm radially and 405 cm along

z. Inside the tracking volume, the magnetic field strength of 4.75 kG is uniform to within 3% and is known with an error of less than 0.1% using calibration information from two Hall probes.

2.6 Liquid Argon Barrel Calorimeter

The liquid argon (LA) barrel calorimeter, which contains 14 radiation lengths over 64% of 4π, samples electromagnetic energy deposits and is used for electron identification. It is composed of eight cryostat modules, each measuring about $1.5 \times 3.8 \times 0.21$ m^3. They are arranged in an octagon outside the magnet coil and cover $|\cos\theta| < 0.68$, with gaps between the modules of 3° in the azimuthal angle, ϕ. The modules consist of alternating layers of 2-mm lead sheets and lead strips with 3-mm gaps filled with liquid argon.

The orientations of the strips can be along the beam axis (F), perpendicular to it (T), or at 45° to it (U), as listed in Table 2.1. Groups of layers with the same strip orientation are ganged together to form the six readout channels (F1, T1, U, F2, T2 and F3) shown in Figure 2.4. In addition, there is a pair of liquid argon gaps formed by 1.6-mm aluminum sheets and readout strips. These strips measure energy loss in the 2 radiation lengths of material preceding the lead stack, including the magnet coil. The signals from the readout strips are amplified and followed by sample-and-hold modules which store the peak charge. The charge is processed in CAMAC crates housing BADCs. A BADC is a 12-bit ADC incorporated in a 16-bit microprocessor which performs pedestal subtractions, gain corrections and threshold cuts.

The energy resolution is about $\sigma_E/E = 0.14/\sqrt{E(\mathrm{GeV})}$. From Bhabha events at PEP, the measured resolution is $\sigma_E/E = 4.6\%$, slightly degraded due to saturation in the readout electronics for the massless trigger gap. The measured position resolutions are $\sigma_\phi = 3$ mrad and $\sigma_z = 8$ mm.

Strip Layer	Measured Coordinate	Number of Strips	Strip Width (cm)
Trigger	ϕ	36	3.5
1	ϕ	38	3.5
2	θ	100	3.5
3	u	70	5.4
4	ϕ	38	3.5
5	θ	100	3.5
6	u	70	5.4
7	ϕ	40	3.5
8	θ	100	3.5
9	u	70	5.4
10	ϕ	40	3.5
11	θ	100	3.5
12	θ	100	3.5
13	θ	100	3.5
14	ϕ	40	3.5
15	ϕ	40	3.5
16	ϕ	40	3.5
17	ϕ	40	3.5
18	ϕ	40	3.5

Table 2.1: Orientation, width and number of strips per layer in each LA module.

2.7 Endcap Calorimeter

The endcap (EC) calorimeters complement the LA calorimeter by detecting electromagnetic energy in the angular range $0.70 < |\cos\theta| < 0.95$ as illustrated in Figure 2.5. The first layers of the two lead/proportional tube calorimeters are located ± 1.37 m in z from the interaction point. Each EC calorimeter contains 36 layers of 0.28-cm-thick lead sheets alternating with planes of 191 proportional tubes, for a total thickness of 18 radiation lengths. The tubes in each plane form an annulus with radii 40 cm and 146 cm. A tube is made of aluminum with a cross section of 0.9×1.5 cm^2 and has a 50-μm diameter wire strung through its center. The first 20 tube planes alternate

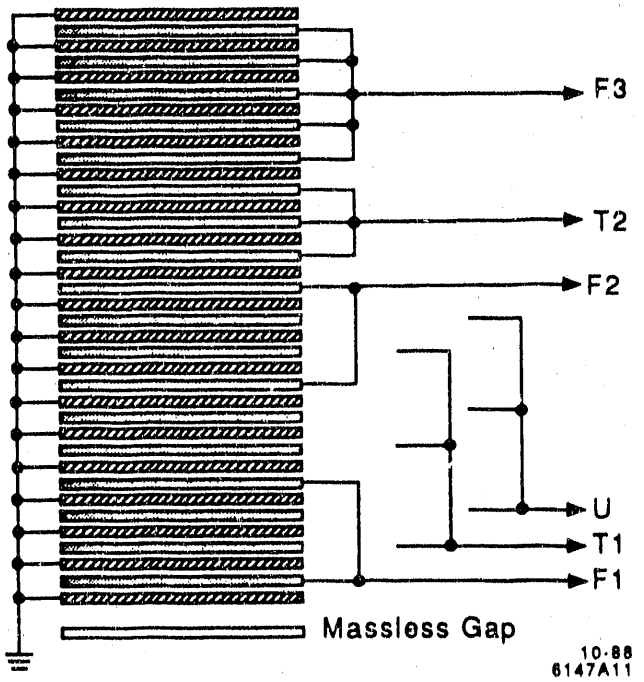

Figure 2.4: Ganging scheme for electronic channels in the LA calorimeter. Particles enter from the bottom, through the massless gap.

between being oriented vertically (X), horizontally (Y), canted $-45°$ (U) and canted $+45°$ (V) while the last 16 planes alternate X and Y layers. Groups of tubes are ganged together to form readout channels making 10 measurements along the depth of the calorimeter, in the projection from the interaction point.

The calorimeters are operated with HRS gas slightly above atmospheric pressure. The quality of the gas is monitored through analysis of the pulse height spectrum from ^{55}Fe sources on four small tubes located at the inlet and outlet of the two EC calorimeters. The energy resolution is measured with PEP Bhabha events to be $\sigma_E/E = 0.22/\sqrt{E(\mathrm{GeV})}$. Since the PEP operation, the number of dead channels has been reduced and the tightness of the gas system has been increased. The measured position resolution is 0.3 cm in both the x and the y directions.

2.8 Muon System

The muon system is used to identify muons over 45% of 4π. Surrounding the LA calorimeter are four walls of hadron absorber and proportional tubes. Each wall

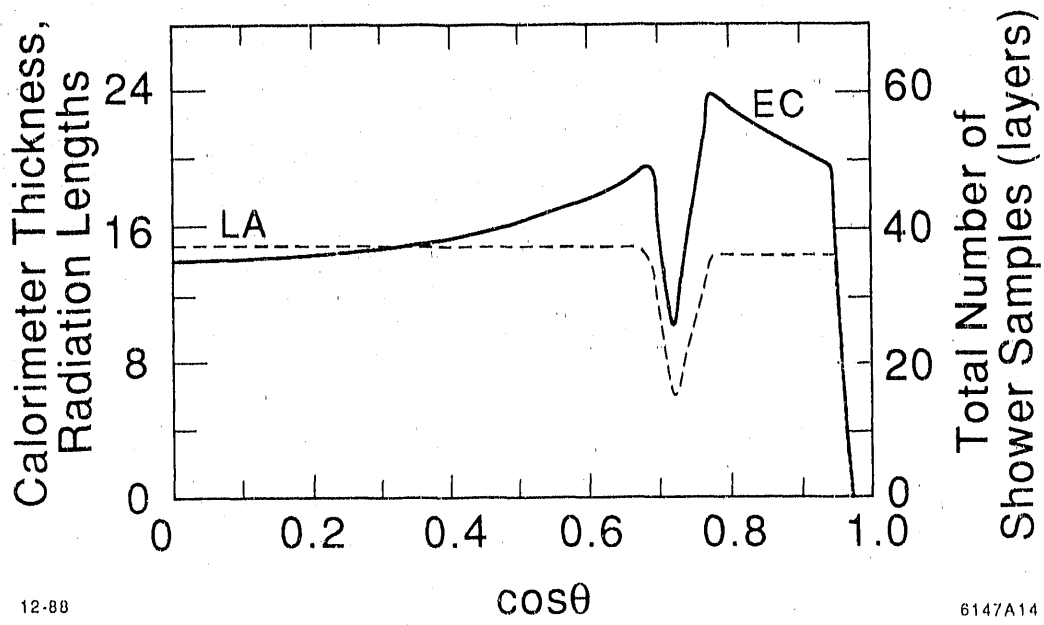

Figure 2.5: Total calorimeter thickness (solid line) and number of sampling layers (dashed line) versus $\cos\theta$.

contains four layers of tubes preceded by iron plates. The outer layer of tubes is separated from the center of the Mark II by 7 nuclear interaction lengths. The location and thickness of the absorber material are given in Table 2.2.

Extruded aluminum modules with eight triangular proportional tubes, illustrated in Figure 2.6, run the full length of the hadron absorber. The tubes of the innermost

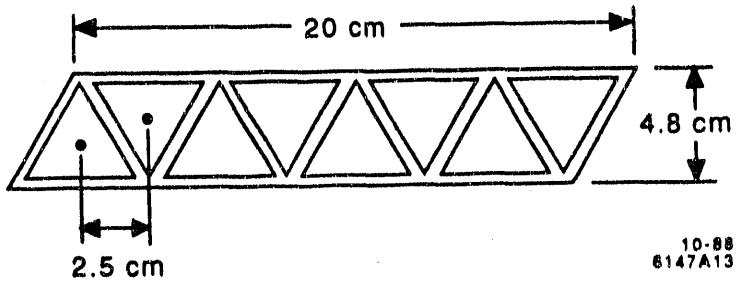

Figure 2.6: Cross section of a muon proportional tube module.

layer are oriented perpendicular to the beam axis to measure the polar coordinate, θ, while the tubes of the outer three layers are oriented parallel to the beam axis to

	East		Top		West		Bottom	
Layer	d (m)	λ	d (m)	λ	d (m)	λ	d (m)	λ
Before 1		1.17		1.17		1.17		1.17
1	3.2	1.38	2.5	1.38	3.2	1.38	2.5	1.38
2	3.6	1.40	2.8	1.40	3.6	1.40	2.8	1.40
3	4.0	1.85	3.2	1.81	4.0	1.85	3.2	1.85
4	4.5	1.49	3.6	1.40	4.5	1.49	3.6	1.85
Total		7.28		7.16		7.28		7.65

Table 2.2: Muon absorber geometry: d is the perpendicular distance of the absorber from the interaction point and λ is the thickness of the absorber in interaction lengths.

measure the azimuthal coordinate, ϕ. The 45-μm wires at the center of each tube are separated by 2.5 cm, a distance comparable to a typical multiple-scattering deviation for a particle passing through each layer of absorber. The signals from each of the 3264 wires of the muon system are discriminated and read out digitally.

2.9 Luminosity Monitors

Two luminosity monitors detect e^+e^- (Bhabha) scattering events at small and well-defined angles on both sides of the interaction point. The small-angle monitor (SAM) covers the angular range $50 < \theta < 160$ mrad on both sides and the mini-small-angle monitor (Mini-SAM) covers $15.2 < \theta < 25.0$ mrad and $16.2 < \pi - \theta < 24.5$ mrad.

2.9.1 Small-Angle Monitor

There are four SAM modules, two on each side of the interaction point. Each module consists of nine layers of drift tubes for tracking and a six-layer lead-proportional-tube sandwich for measuring the electron and positron energies and positions. The layout and location of a SAM module is shown in Figure 2.7. The total thickness of each SAM is 14 radiation lengths. Both the drift and proportional wire planes are constructed from square aluminum tubes 9.5 mm wide containing a 38-μm-diameter wire in the center. The wire planes alternate between being oriented horizontally (Y),

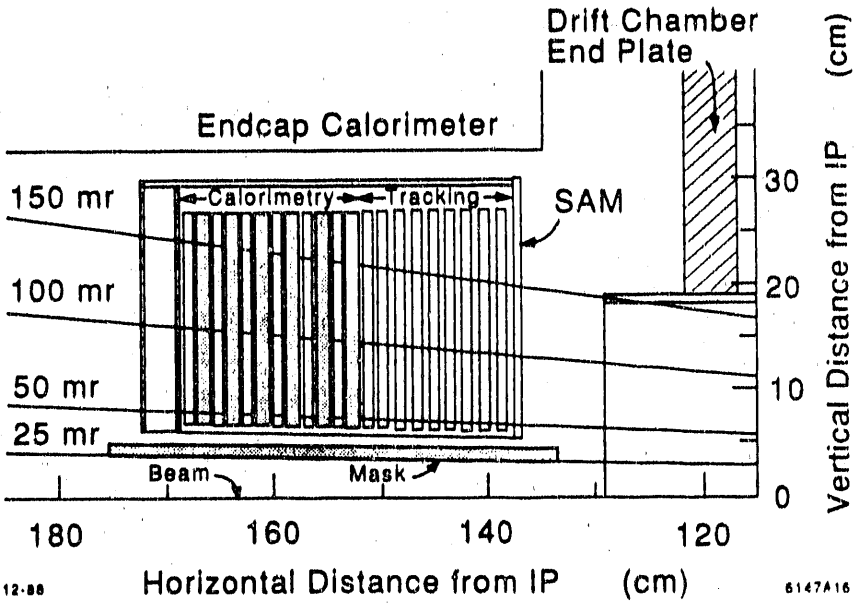

Figure 2.7: Side view of one of the four SAM modules showing its location inside the Mark II detector.

canted +30° (U) and canted −30° (V).

The energy resolution measured with a beam of positrons in the range 5–15 GeV is $\sigma_E/E = 0.45/\sqrt{E(\mathrm{GeV})}$. Using the calorimeter section of the SAM, the estimated systematic error on the luminosity measurement due to detector resolution and reconstruction effects is 2%.

2.9.2 Mini-Small-Angle Monitor

The Mini-SAM consists of two tungsten-scintillator sandwiches divided into four azimuthal quadrants. Each quadrant consists of six layers of scintillator preceded by tungsten slabs, for a total thickness of 15 radiation lengths and an expected energy resolution of $\sigma_E/E = 0.35/\sqrt{E(\mathrm{GeV})}$. Bhabha events are identified as back-to-back coincidences of large energy deposits in two adjacent azimuthal quadrants, as illustrated in Figure 2.8. The angular acceptance is defined by conical tungsten masks with thicknesses of 15 radiation lengths. Because misalignments in the masks limit the usefulness of the Mini-SAM for measuring the absolute luminosity, it is calibrated relative to SAM events recorded in a precise angular region.

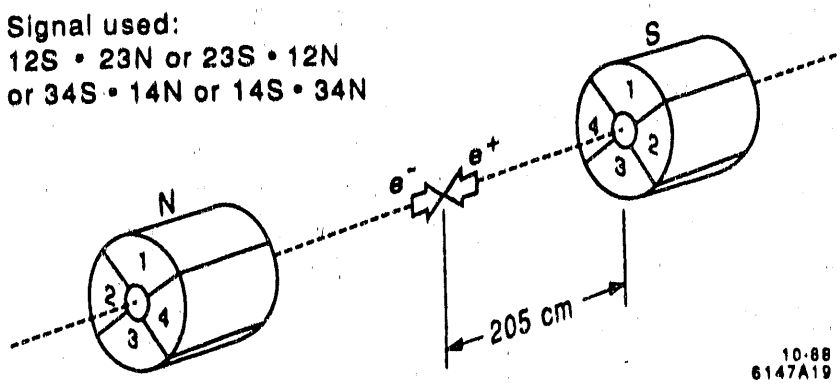

Figure 2.8: Geometry of the Mini-SAM. As an example in the 'Signal Used' definition, 12S means that the signal sum of quadrants 1 and 2 exceed a Bhabha threshold in the south monitor.

2.10 Extraction Line Spectrometer

The extraction line spectrometers measure the energies of the electron and positron beams in the extraction lines to the beam dumps, 150 m downstream of the interaction region. These spectrometers record the magnetic deflection of each beam by detecting narrow swaths of synchrotron light emitted before and after the beams pass through precision spectrometer magnets. The layout of the extraction line is shown in Figure 2.9. The separation and thickness of the two synchrotron swaths are measured

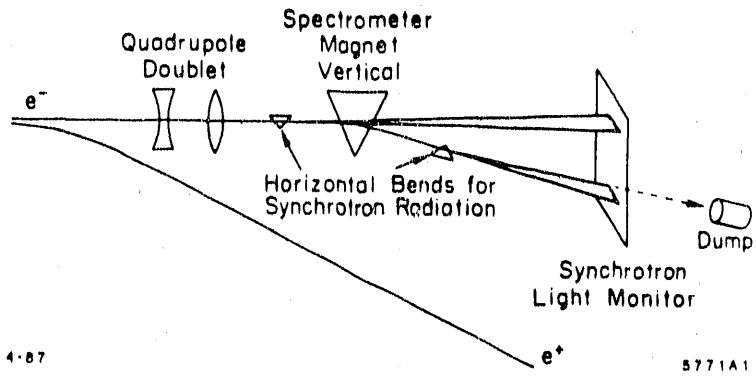

Figure 2.9 Conceptual design of the extraction line spectrometer system.

by a phosphorescent screen monitor consisting of two identical target and camera systems. The target consists of an array of fiducial wires on a phosphorescent screen which emits light when hit by the synchrotron beam. The image of the target from

the camera system is digitized and used to determine the location of the synchrotron swath. The targets are mounted at a fixed distance from each other on a support structure, shown in Figure 2.10, composed of an iron-nickel alloy with low thermal

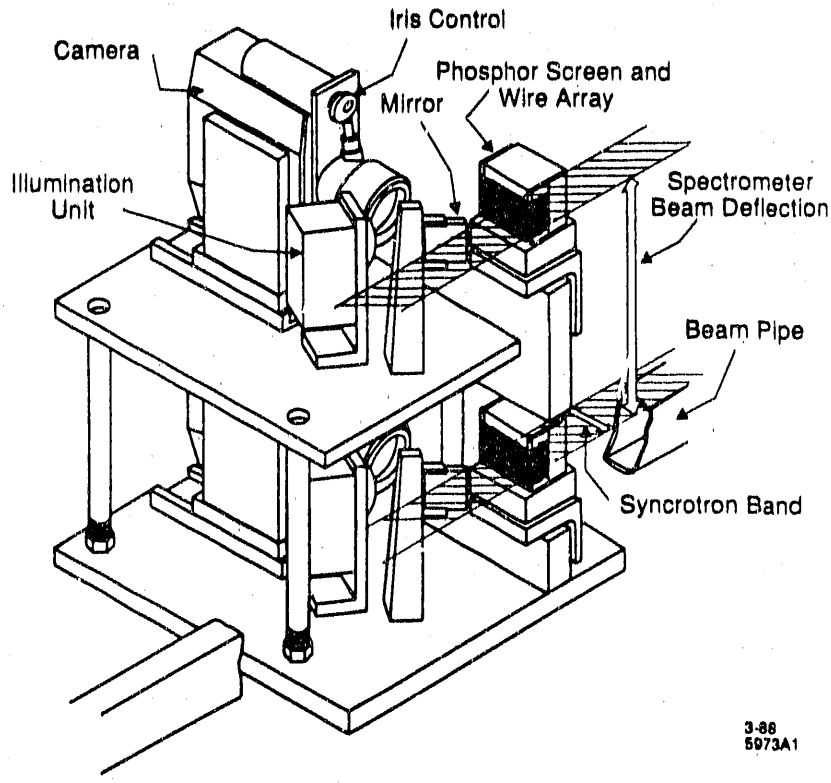

Figure 2.10: Schematic view of the phosphorescent screen monitor.

expansion coefficient.

Knowledge of the separations of the synchrotron swaths and of the magnetic field strength of the precision magnets determine the mean center-of-mass energy for every pulse to an accuracy 35 MeV. Analysis of the thickness of the synchrotron stripes yields the center-of-mass energy spread, typically 250 MeV.

2.11 Trigger and Data Acquisition Systems

The trigger system selects events for readout by the data acquisition system. Both primary and secondary triggers are satisfied for the events that are logged to tape for offline analysis.

There are two primary trigger signals used during data-taking with SLC beams. The first is the data primary trigger, which is the SLC beam crossing signal, occurring every 17 ms during operation at 60 Hz. The second is the cosmic primary trigger, which is activated by time-of-flight counter signals, checked every 2.4 μs. The cosmic ray events thus recorded are used to evaluate the performance of the detector. During dedicated cosmic ray runs, only the cosmic primary trigger is on.

The secondary trigger is activated by signals from the tracking or calorimeter systems or by signals generated at random for accelerator background studies and it is inhibited by signals from the SLC, indicating the failure of a klystron in the linear accelerator. The trigger decision is made within 8 ms of a primary trigger by the master interrupt controller (MIC) module, thus allowing for beam data-taking at 120 Hz without dead-time. Three independent triggers from the tracking and calorimeter systems offer a degree of redundancy to measure the relative triggering efficiencies of the different systems, the charged particle trigger, the software trigger and the Bhabha trigger.

The charged particle trigger uses a fast track-finding processor to count the number of charged tracks traversing the drift chamber. A trigger is formed when at least two tracks are found by pattern recognition done on hits in cells from 11 layers of the DC, all but the outermost axial layer. A cell is considered hit when at least four of the six sense wires in the cell have signals detected by the TDCs. The pattern of hits in each layer is loaded into a shift register and transferred serially into special hardware curve-finding or "curvature" modules as shown in Figure 2.11. Each curvature module is programmed to identify patterns of hits falling within a specific range of radii of curvature. Tracks are defined requiring hits in at least 4 out of the 6 stereo layers and at least 8 out of the 11 instrumented layers. All tracks found by all curvature modules within $\sim 10^\circ$ of azimuth of each other are counted as a single track. In addition, a trigger is formed when a coplanar track finder (CTF) finds two tracks that are back-to-back. The CTF uses two curvature modules to find tracks within $\pm 11^\circ$ in azimuth. The charged particle trigger is formed in approximately 60 μs. For cosmic ray runs, the secondary trigger requirement simply consists of at least one charged track with 6 out of 11 layers hit or a back-to-back track.

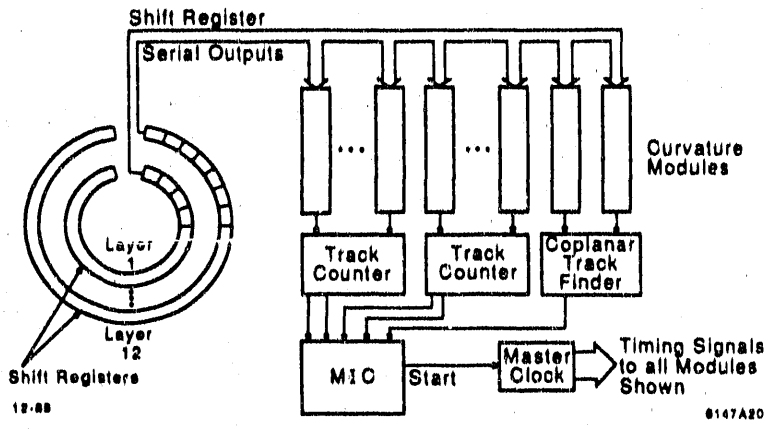

Figure 2.11: Block diagram of the charged particle trigger.

The software trigger uses a SLAC scanner processor (SSP) to find clusters of energy pointing towards the interaction point from the LA and EC calorimeters. The signals from the EC and LA calorimeters are summed in groups of eight adjacent channels and then digitized by FASTBUS ADCs. The SSP uses the digitized data to define hits based upon software thresholds. It then finds clusters by using the hits to index a table of pre-calculated patterns. The software trigger fires on a single shower depositing at least 3.3 GeV in the LA or 2.2 GeV in the EC.

The Bhabha trigger identifies large back-to-back electromagnetic showers using calorimetric information from the LA, EC, SAM and Mini-SAM. The total deposited energy is summed up for each of the ten LA and EC modules, using groups of eight adjacent channels summed at the detector, for the two SAM modules and for the eight mini-SAM modules. The sums are compared to individual thresholds for each module, typically 10 to 20 GeV in the LA and EC, 6 GeV in the SAM and 20 GeV in the mini-SAM. A trigger is fired if energy deposits located in back-to-back modules exceed the thresholds. The thresholds were chosen so as not to limit the data acquisition rate.

The data acquisition system reads CAMAC and FASTBUS data, merges raw data with results from online event tagging, analyzes events, logs data to tape and monitors the detector and electronics under the control of the operators of the Mark II. Event acquisition begins with the primary trigger signal which starts the trigger logic and BADC processing. If a secondary trigger is received, a VAX 8600 reads data from

the entire CAMAC system and awaits a signal from the master system SSP that the FASTBUS system is ready to accept the next event. When the signal is received, the trigger is reset. FASTBUS data are subsequently read into the VAX, combined with CAMAC data and a simple event tagging algorithm is executed. The event is then placed into a global buffer where consumer processes, such as the online analysis program, sample the complete events. The tape logging process is the final consumer of all events.

2.12 Vertex Detectors

Two vertex detectors were recently installed near the center of the Mark II to improve on the charged-track pattern recognition and impact-parameter measurements provided by the central drift chamber. The silicon strip vertex detector (SSVD) provides track position measurements between 2.8 and 3.7 cm from the beam axis over a solid angle comparable to that of the DC, while the drift chamber vertex detector (DCVD) measures track positions for radii between 5 and 17 cm over 85% of 4π. The vertex detectors began taking SLC data during January 1990.

2.12.1 Silicon Strip Vertex Detector

The SSVD consists of two hemi-cylindrical modules with 36 independent silicon strip modules forming three radial layers as illustrated in Figure 2.12. Each module contains 512 detector strips of 300-μm thickness oriented parallel to the beam axis and hence measuring only the r and ϕ coordinates of tracks. The charge deposited on each strip is stored in custom 128-channel VLSI chips located on the modules and subsequently read out serially to BADCs.

Tests of the modules with X-ray sources and particle beams showed that they have a spatial resolution of better than 5 μm and a two-track separation of approximately 150 μm. The impact-parameter resolution expected from combining DC and SSVD hits is $\sim$ 10 μm with a contribution of $36/p(\mathrm{GeV}/c)$ μm from multiple scattering. The SSVD is calibrated by using tracks from Z-decay events.*

*The rate for usable cosmic-ray events in the SSVD is predicted to be less than 3 per day. This

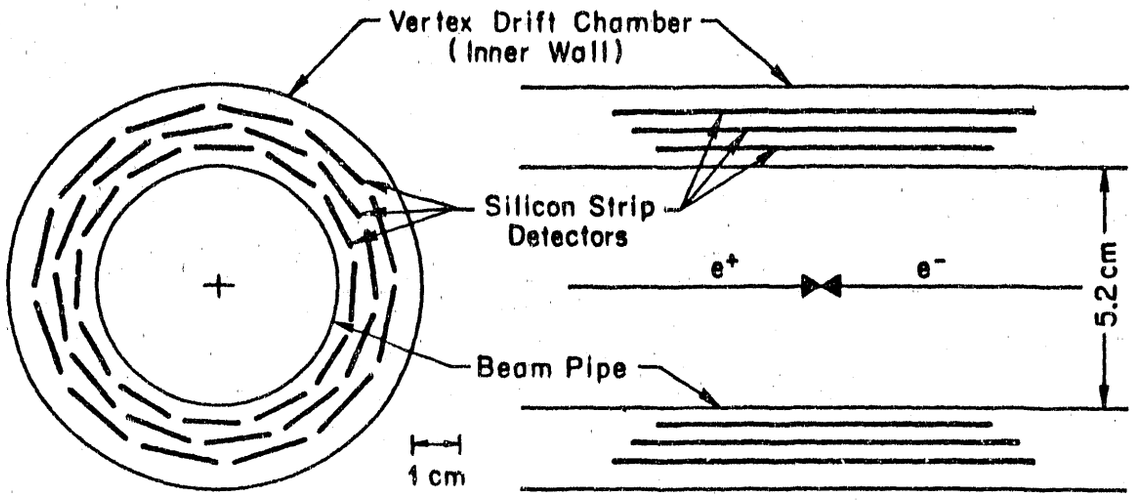

Figure 2.12: Layout of the silicon strip vertex detector.

2.12.2 Drift Chamber Vertex Detector

The DCVD provides vertexing information that is both independent and complementary to the SSVD, its main strength being powerful pattern recognition in a dense and noisy tracking environment. It also improves on the momentum measurements, the ionization loss measurements and the trigger noise rejection obtained from using only the central drift chamber.

The DCVD consists of a cylindrical chamber divided up into ten axial cells with a modified jet cell design. Each cell contains 40 sense wires running parallel to the beam pipe, providing position measurements in the r–ϕ plane. The sense wire planes are tilted by 15° to the radial direction to allow resolution of the left–right ambiguity and to ensure that radial tracks do not spend their entire length close to a wire plane. As can be seen in Figure 2.13, the wires run between Macor wedges, mounted 55 cm apart with micron-level precision onto the end-plates. The 20-μm sense wires are located 2.9 mm apart, within a few microns of their desired positions, alternating with potential wires. The sense wire planes are sandwiched between two grid wire planes which improve the electrostatic stability of the sense wires and focus drifted

low rate results from its small cross section, its reliance on slow BADCs and its limited live-time due to heat dissipation.

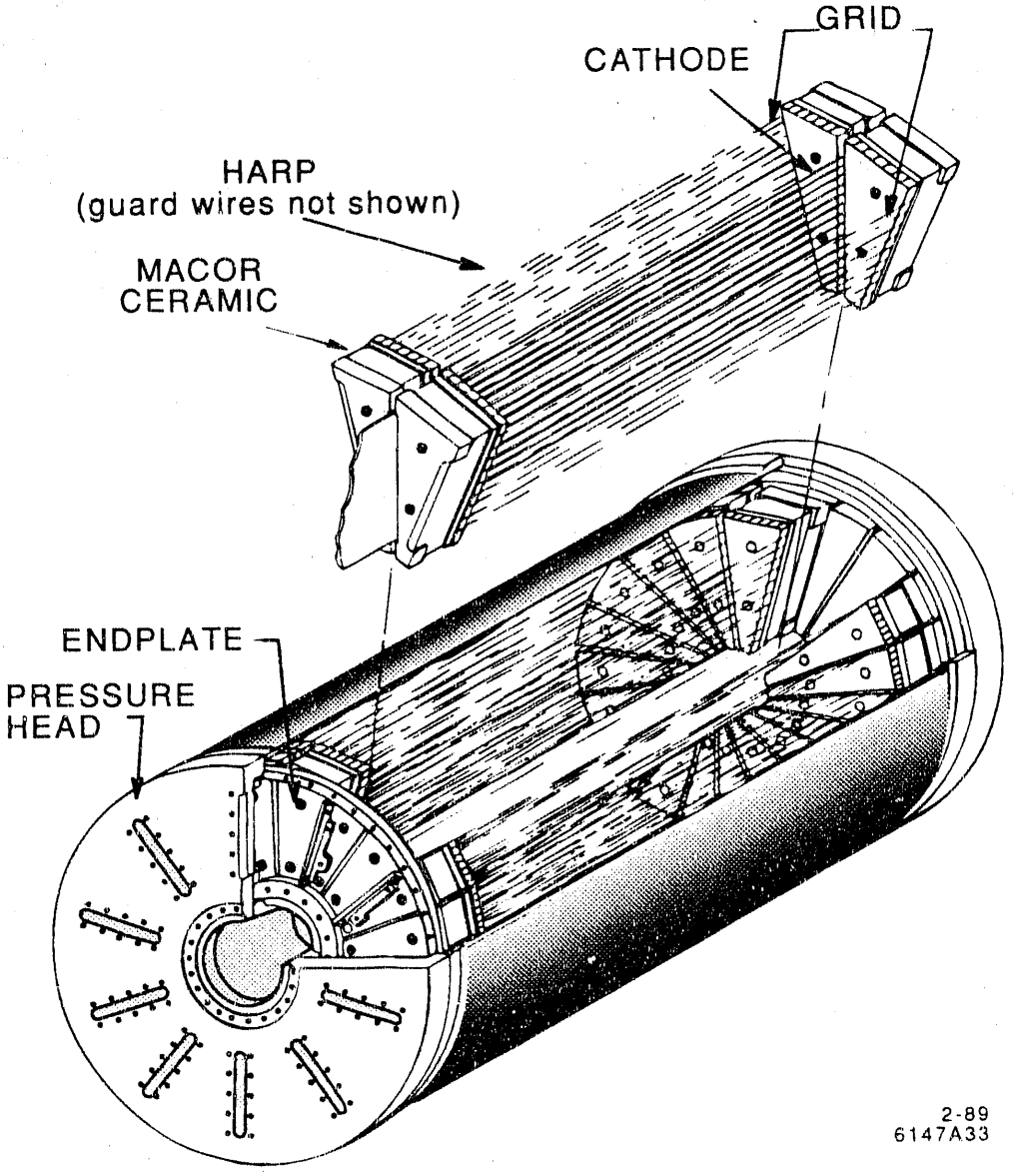

Figure 2.13: Cut-away drawing of the drift chamber vertex detector.

electrons onto the sense wires. The voltages on all wires are controlled to within one part in 10^4.

The middle 38 sense wires in each cell are instrumented with a fast integrating, charge-sensitive hybrid pre-amplifier. Signals from the 380 preamps are further amplified and shaped in post-amplifiers, digitized in FADCs and processed into time and charge measurements inside two SSPs. The linear 6-bit FADCs record pulse heights over 1024 10-ns buckets with calibration pedestals stable to $\pm 1/3$ of a least count and ± 0.3 ns.

To achieve the best spatial resolution, the DCVD gas (92% CO_2 and 8% C_2H_6) is run in the unsaturated regime, which provides low electron diffusion and a slow (6 μm/ns) drift velocity. A sufficient electron lifetime, in excess of 30 μs, is obtained by reducing oxygen contamination to less than 1 ppm. The temperature is kept stable to within 0.1° C and the pressure is regulated to within 10^{-3} atm.

The chamber is operated at 2 atm and is expected to achieve an impact-parameter resolution of 15 μm with a contribution of $60/p(\mathrm{GeV}/c)$ μm from multiple scattering. The spatial resolution is dominated by electron diffusion which increases by the square root of the drift distance, D. From cosmic ray measurements, the position resolution is determined to be 20 μm, added in quadrature to a diffusion contribution of $37\sqrt{D(\mathrm{cm})}$ μm for pure CO_2 gas at 2 atm or $26\sqrt{D(\mathrm{cm})}$ μm for DCVD gas at 3 atm [Alexander 89]. The dE/dx resolution is about 9% when using truncated means of more than half of the charge measurements per track. Analysis of the shapes of the recorded pulses allows distinction between tracks separated by less than 700 μm.

In Section 7.2 we show results on the calibration and performance of the vertex detectors inside the Mark II detector from the run in January 1990.

Chapter 3

Monte Carlo Simulation

Monte Carlo (MC) simulations are used to calculate the efficiencies for observing $udsc$ and $b\bar{b}$ events in the sample of hadronic events as well as in the subsample of events tagged by isolated leptons. In the simulation program, the bottom quarks produced in e^+e^- annihilation yield lepton signals in the detector at the end of five processes:

1. The electroweak interactions form Z bosons which decay to bottom quark–anti-quark pairs.
2. The strong interactions produce gluons and light quark pairs from the energetic primary b quark.
3. Fragmentation turns the quarks and gluons into hadrons, using different models for light and heavy quarks.
4. The weak interactions are responsible for the decay of B hadrons to leptons.
5. Electromagnetic interactions produce signals of electrons and muons in the detector that are distinct from the signals of hadrons interacting via the nuclear force.

The description of each of these processes incorporates a wealth of experimental data from previous experiments, including the Mark II. The process of $b\bar{b}$ production is described in Section 1.1.2. In this chapter, we describe the theoretical motivation for each of the four subsequent processes, the experimental data used to tune each simulation, and the implementation of the process in the Monte Carlo simulation of hadronic Z decays.

3.1 QCD and Fragmentation Models

The theory of the strong interactions in the standard $SU(3) \times SU(2) \times U(1)$ model, quantum chromodynamics (QCD), describes how quarks and gluons interact via their color charges. Just like its electromagnetic counterpart, quantum electrodynamics, QCD prescribes how the coupling strength varies with the momentum transfer of interactions considered, once the coupling has been specified at a fixed reference scale. The strength of the couplings of the two types of interaction and their energy evolution are very different, however. The electromagnetic coupling constant is small at low energies, $\alpha = 1/137$ below $2m_e = 1$ MeV, and it increases slowly with energy to $\alpha = 1/129$ at $M_Z = 91$ GeV, while the strong coupling constant is larger than unity below $m_p = 1$ GeV, decreasing rapidly to $\alpha_s = 0.12 \pm 0.01$ at 91 GeV [Akrawy 90, Komamiya 90].

Although quarks and gluons experience what is called asymptotic freedom at large energies, the strong interaction ensures that they are never observed as free particles at small energies. For example, when a single quark is separated far enough from other quarks, the increased strength of the color interaction will become large enough to produce a pair of light quarks from the vacuum, thus confining the single quark. Just as charged particles combine into electrically neutral states such as atoms, quarks combine into color-neutral states. The stable color-singlet states, hadrons, are either baryons, containing three quarks, or mesons, containing a quark and an anti-quark. While perturbative calculations in QCD are valid at large energies, they break down around 1 GeV, the energy that characterizes bound states of light quarks into mesons and baryons. Hence, we need models of fragmentation, the process which turns quarks and gluons into hadrons.

Figure 3.1 is a schematic picture of the processes involved in producing a bottom hadron from e^+e^- annihilation. The strong interactions are modelled in a two-stage process: first QCD-based models generate quarks and gluons, called partons, and then fragmentation models hadronize the partons. The QCD models that are commonly used for e^+e^- annihilation experiments at center-of-mass energies below the Z mass calculate the four-momenta of quarks and gluons to second order in α_s, allowing at

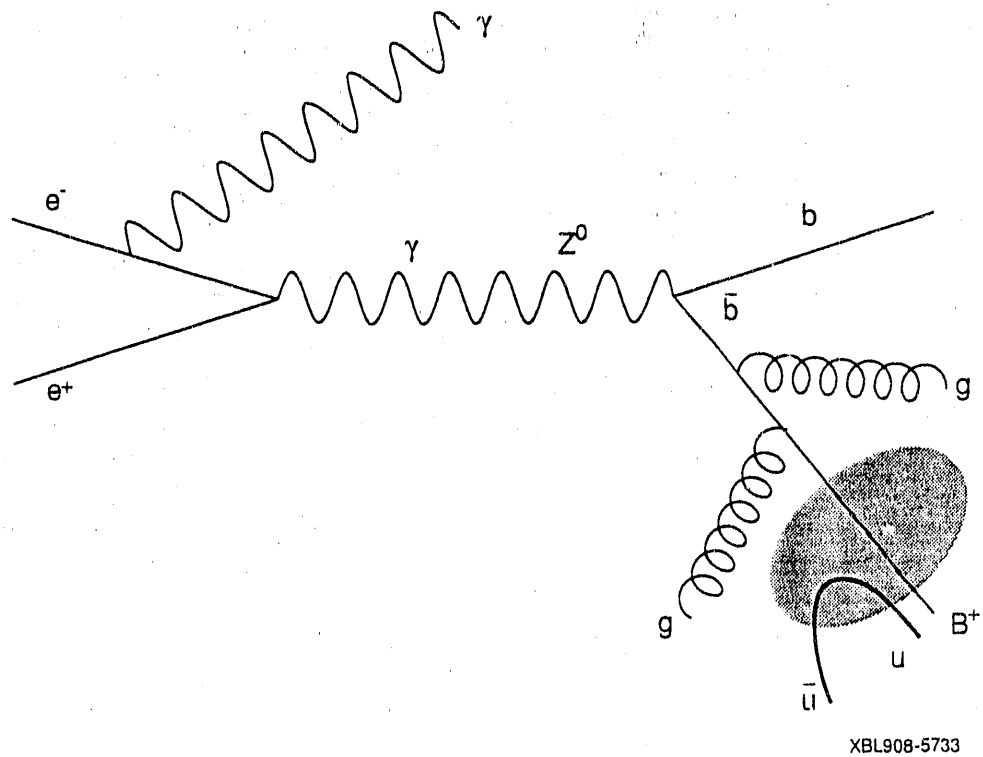

Figure 3.1: The annihilation of e^+e^- into $b\bar{b}$ and the subsequent fragmentation of a $\bar{b}$ quark into a B^+ meson. The shaded area around the $\bar{b}$ quark is described by fragmentation models, which also hadronize the other partons of the event, b, g and g.

most four final-state partons. To compute individual two-parton, three-parton and four-parton cross sections, a method called jet dressing is employed. Each pair of generated partons, i and j, are required to have a squared invariant mass, $(p_i + p_j)^2$, above some threshold, typically $0.01s$ or $0.015s$. If the invariant mass of two partons in a four-jet event fail the requirement, the event is considered a three-jet event, and if one more pair fails, the event becomes a two-jet event, $q\bar{q}$.

Recently, models have been constructed that better reproduce the data, including multi-jet final states of Z decays. These parton shower models, hybrids of QCD and classical physics, produce showers by successively splitting off gluons and quark–anti-quark pairs, starting with the original pair. The shower process, which is illustrated in Figure 3.2, is terminated when a mass cutoff is reached. This cutoff can be quite low, the quark mass itself for heavy quarks, or 1 GeV/c^2 for light quarks. Since the

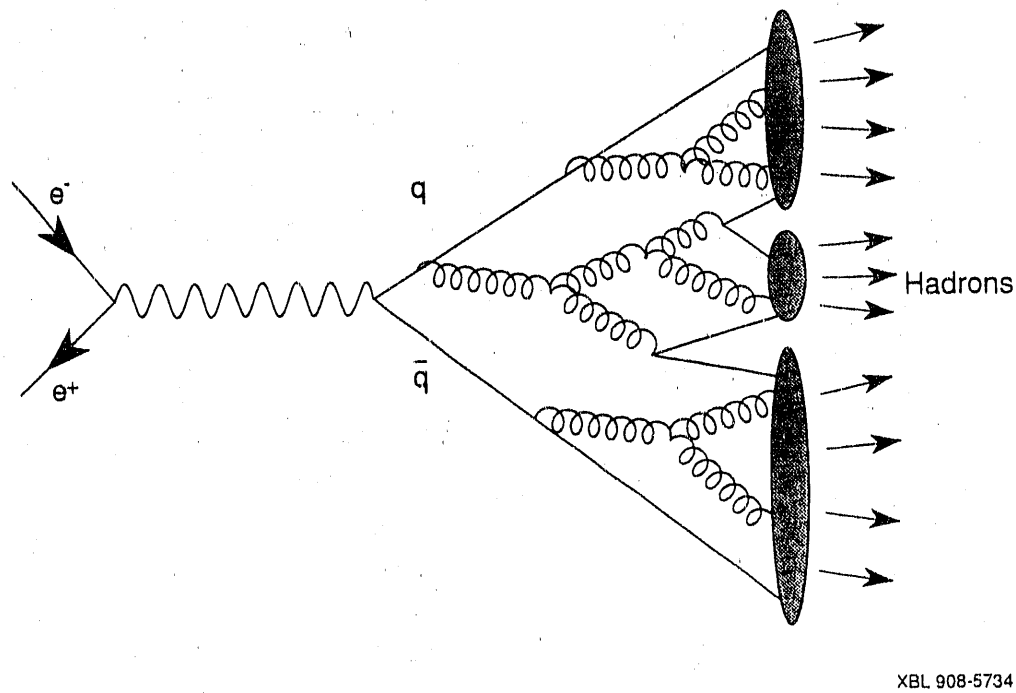

Figure 3.2: The evolution of a parton shower produced in e^+e^- annihilation. The shaded areas are described by fragmentation models.

cutoff is a fixed mass, the shower models do not require different fragmentation model parameters for data taken at different center-of-mass energies.

Among many models for fragmentation, the Webber cluster model [Webber 84] and the Lund string model [Andersson 83] are used most commonly. At the end of the parton shower, the Webber model forms color singlet clusters from nearby quarks and gluons. These clusters, which are thought of as superpositions of resonances, are made to decay into hadrons. There are no free parameters or fragmentation functions in this scheme for hadronization.

Quark confinement in the Lund model is pictured as arising from color strings between quarks and anti-quarks. When a string is stretched, it can break into new quark--anti-quark pairs which continue to fragment independently. The color flux lines are constrained in tubelike regions around the partons, the tubes being described by a longitudinal space dimension and time. Transverse momenta arise from a tunneling mechanism for $q\bar{q}$ production, which gives rise to a Gaussian distribution. The

transverse momenta of hadrons in jets, observed to be approximately 0.3 GeV, result from the vectorial sum of the transverse momenta of their constituent quarks.

The model for longitudinal fragmentation is derived in the light cone frame, i.e. assuming that the quarks have large energies compared to their masses, with the two transverse directions ignored, except that transverse masses are used everywhere, $m_\perp^2 = m^2 + p_\perp^2$. The fraction of energy-momentum that a quark passes on to a meson, z, is defined to be invariant under boosts along the quark momentum,

$$z = \frac{(E + p_{\|})_{\text{hadron}}}{(E + p)_{\text{quark}}}. \tag{3.1}$$

In the Lund model, the probability distribution as a function of z for a quark of flavor α to combine with an anti-quark of flavor β to give a meson is

$$f(z)dz \propto \frac{1}{z} z^{a_\alpha - a_\beta}(1-z)^{a_\beta} e^{-\frac{bm_\perp^2}{z}} dz, \tag{3.2}$$

where the flavor-dependent a_α and a_β and the flavor-independent b are parameters to be determined from data. In practice, only two parameters, a and b, are employed to describe hadronic events recorded at PEP and PETRA.

3.1.1 Hadronic Z-Decay Simulations

In our study of hadronic Z decays, we use the Monte Carlo simulations based on the Webber-Marchesini parton-shower model with cluster fragmentation (BIGWIG 4.1) [Marchesini 84, Webber 84] and the Lund parton-shower model with string fragmentation (JETSET 6.3 shower) [Sjöstrand 86, Sjöstrand 87, Bengtsson 87]. The parameters of these models were tuned on hadronic events recorded at PEP with both the original and upgraded Mark II detectors, as summarized in Table 3.1.

The global event properties used to determine these parameters are not found to be appreciably affected by the presence of different flavors, since the masses of the quarks are small compared to the center-of-mass energies and since the fraction of hadronic events which contain b quarks is relatively small.

Webber-Marchesini		
Parameter	Range tested	Best value
Λ_{LLA} QCD scale (GeV)	0.15–0.3	0.2
m_g cutoff for further parton evolution (GeV)	0.6–0.85	0.75
m_{cl} cutoff for string breaking of clusters (GeV)	2.5–3.8	3.0
Lund		
Parameter	Range tested	Best value
Λ_{LLA} QCD scale (GeV)	0.2–0.6	0.4
Q_0 cutoff for parton evolution (GeV)	1.0–2.0	1.0
a fragmentation-function parameter	0.1–0.5	0.45
b fragmentation-function parameter	0.8–1.2	0.9
$\sigma_q/\sqrt{2}$ parameter of the Gaussian $p_\perp$ (GeV/c)	0.18–0.27	0.23

Table 3.1: The parameters for the Webber-Marchesini and Lund models as determined from data at $E_{\mathrm{cm}} = 29$ GeV [Petersen 88].

3.2 Heavy-Quark Fragmentation

In studies of heavy quarks, however, the flavor dependence of fragmentation cannot be ignored. The heavier the quark, the more of the parent quark energy is carried by the hadron produced through fragmentation [Suzuki 77, Bjorken 78]. This hard fragmentation of charm [Bethke 85] and bottom quarks [Chrin 87] has been observed in many experiments. Instead of using the Lund fragmentation function (Equation 3.2) with flavor-dependent parameters, it has became customary to use a different fragmentation function for heavy quarks, the function formulated by Peterson *et al.* [Peterson 83].

The Peterson fragmentation function is derived under the assumptions that fragmentation depends on energy transfer q as $1/zq^2$, that the momentum along the quark direction is conserved and that the quark and hadron energies are high compared to the quark masses. Effectively, the heavy quark is boosted to infinite momentum, fragmented into a meson (containing the heavy quark and a light anti-quark) and a light quark, and then boosted back to its original momentum. These assumptions

lead to the distribution

$$D(z)dz \propto \frac{1}{z(1-\frac{1}{z}-\frac{\epsilon}{1-z})}dz, \tag{3.3}$$

where ϵ depends on the heavy-quark flavor. The parameter ϵ is different for b and c quarks since in this model

$$\epsilon = \frac{m_\perp^2(\text{light quark})}{M_\perp^2(\text{heavy quark})}, \tag{3.4}$$

where the transverse mass of the light quark is approximately 0.3 GeV/c^2, corresponding to the mean transverse momentum of jets or the binding energy per quark in light hadrons.

3.2.1 Experimental Determination of Mean z

In practice, because the Peterson fragmentation function is not expected to hold for ordinary quark energies, the Peterson function is regarded as little more than a convenient way to parameterize heavy quark fragmentation in terms of the single parameter ϵ which can be measured from data. With larger data samples than are currently available, more information could be extracted from the z distribution than its mean, $\langle z \rangle$, which is related to the ϵ parameter of the Peterson function (Equation 3.3). With reconstructed hadrons, it is possible to measure observables such as

$$x_p = \frac{p_{\text{hadron}}}{\sqrt{E_{\text{cm}}^2/4 - M_{\text{hadron}}^2}} \tag{3.5}$$

on an event-by-event basis. This direct method of determining the x_p spectra has been used for D^* mesons by many experiments [Bethke 85]. For other heavy-quark hadrons, which lack of large samples of reconstructed hadrons, fragmentation parameters are measured indirectly using leptons from semileptonic decays.

Experiments studying inclusive lepton production in hadronic events at the center-of-mass energies of the PEP and PETRA storage rings have measured the fragmentation function parameters and semileptonic branching ratios of charm and bottom hadrons. The momenta of the leptons are sensitive to the fragmentation functions and were thus used to determine the mean z of the heavy quarks. The heavy quarks

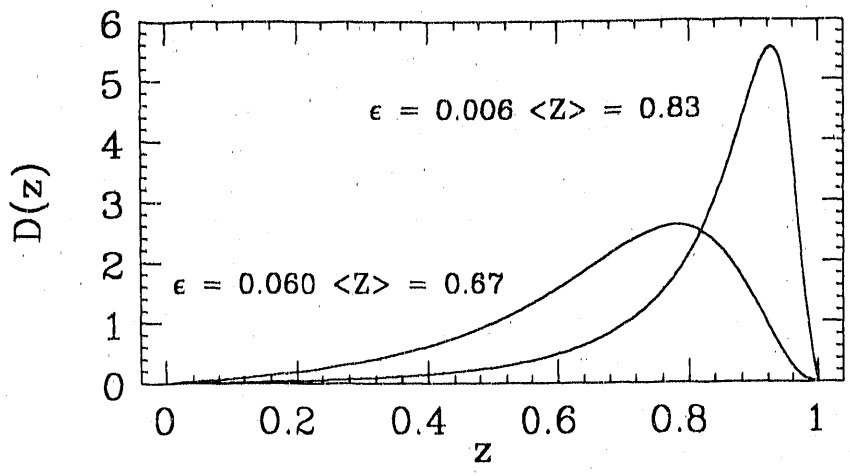

Figure 3.3: Peterson fragmentation functions corresponding to mean z values of 0.67 and 0.83.

were identified from the large the transverse momenta of leptons. The transverse momenta were defined with respect to the event thrust direction, which approximates the quark direction. The fragmentation function parameters and branching ratios were extracted from fits to the momentum and transverse momentum spectra of identified leptons. The fits included estimates of backgrounds to leptons from heavy quarks, misidentified hadrons and leptons from decays of hadrons containing light quarks [Nelson 83a].

Data from leptons in hadronic events produced at PEP and PETRA give the average values $\epsilon_c = 0.06^{+0.03}_{-0.01}$ and $\epsilon_b = 0.006^{+0.002}_{-0.002}$ [Chrin 87], whose ratio is consistent with the ratio of the squares of the b and c quark masses. These values of ϵ were obtained from measured mean values of z through the Peterson functions (Equation 3.3) plotted in Figure 3.3. The measurement of $\langle z \rangle$ depends to varying degrees on the value of the strong coupling constant, the models for QCD and fragmentation, and the mass cutoff for the transition from the QCD model to the fragmentation model.

3.2.2 Heavy Quarks in Z Decays

The fragmentation of bottom and charm quarks in the hadronic Z-decay Monte Carlo simulation is tuned to the data from the PEP and PETRA experiments. The simulations of Z decays are different from the simulations at lower $E_{\rm cm}$ in that shower models with a small mass cutoff are used instead of matrix-element models with a large mass cutoff. This means that the simulations of Z decays rely more upon the QCD-based shower models and less upon the phenomenological fragmentation models.

In tuning the Monte Carlo simulation, it is important to distinguish between the energy-momentum fraction distribution that is fed into the fragmentation model, z', and the distribution that results after fragmentation, z. To simulate heavy-quark fragmentation with the Peterson distribution, we specify the value ϵ', which generates a distribution of

$$z' = \frac{(E + p_{\|})_{\rm hadron}}{(E + p)_{\rm unfragmented\ system}}, \tag{3.6}$$

where the unfragmented system consists of the heavy quark and its nearby partons. The resulting distribution of z is different from the distribution of z', since the denominator of z (in Equation 3.1) only contains the heavy quark, in isolation from the other partons. In particular, sometimes $z > 1$, and the overall result is that $\langle z \rangle > \langle z' \rangle$, as shown in Figure 3.4.

Using the Lund model based on a second-order matrix-element QCD calculation (JETSET 6.3 matrix) with $E_{\rm cm} = 29$ GeV, $\alpha_s = 0.165$ and mass cutoff $= \sqrt{0.015s} = 3.55$ GeV/c^2, as in the simulation used by J. Chrin with version 5.2, we find that the experimentally measured averages $\langle z \rangle_c = 0.67 \pm 0.03$ and $\langle z \rangle_b = 0.83 \pm 0.02$ [Chrin 87], are obtained with $\epsilon'_c = 0.15$ and $\epsilon'_b = 0.020$. With these values for ϵ' in the Lund parton-shower model (JETSET 6.3 shower), at the same energy and mass cutoff, the experimental $\langle z \rangle$ values are reproduced to within ± 0.02 for a range of strong coupling constants (which are parameterized differently in the matrix and shower models). We use $\epsilon'_c = 0.15$ and $\epsilon'_b = 0.020$ in the Lund parton-shower simulation of hadronic Z decays, which leads to $\langle z \rangle_c = 0.78$ and $\langle z \rangle_b = 0.83$ for the model parameters given in Table 3.1. The difference between this value of $\langle z \rangle_c$ and the above measured value results mainly from the extrapolation to the small 1-GeV/c^2 shower-model mass cutoff.

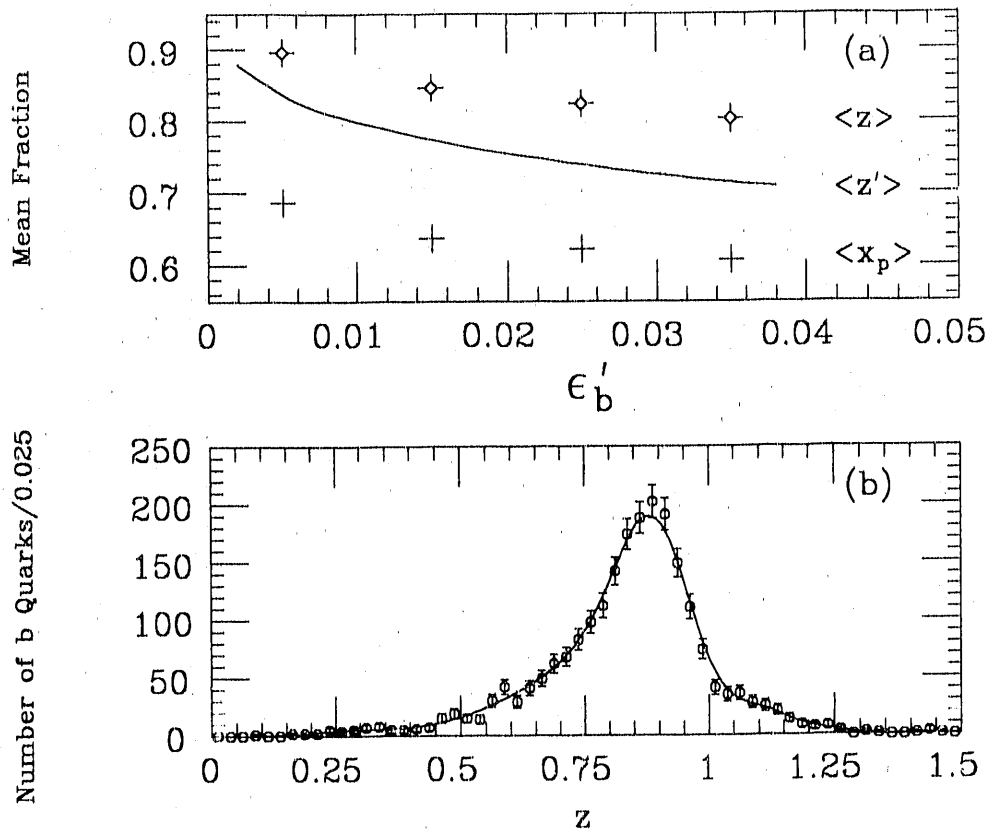

Figure 3.4: Energy-momentum fraction variables for bottom-quark fragmentation in the Lund parton-shower simulation of Z decays. Plotted are (a) the means $\langle z' \rangle$, $\langle z \rangle$ and $\langle x_p \rangle$ as a function of ϵ'_b and (b) the distribution of z for $\epsilon'_b = 0.020$.

3.3 B Decays

The bottom hadrons produced through e^+e^- annihilation to b quarks and their subsequent fragmentation are unstable. We use leptons from semileptonic B decays to tag b quarks, thus relying in our Monte Carlo simulation on lepton momentum spectra and branching ratios determined in other experiments. These experiments and our use of results from them are described in the sections following a brief introduction to B decays.

In the simplest theoretical model, the spectator model, the b quark in a B hadron decays into a W boson and a c or u quark as in the example of Figure 3.5. This model does not take into account strong or weak interactions between the light spectator quarks and the heavy quarks. These interactions are responsible for most of the

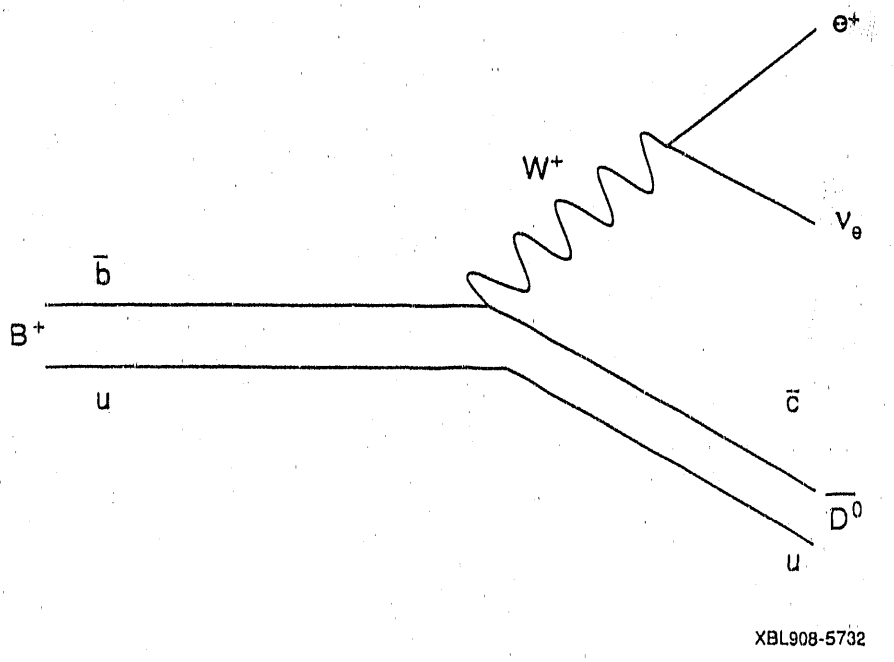

Figure 3.5: The decay $B^+ \to \overline{D^0} e^+ \nu_e$ in the spectator model.

measured difference between the D^+ lifetime, 1.06 ± 0.03 ps, and the D^0 lifetime, 0.42 ± 0.01 ps [Hernández 90]. For decays of hadrons containing the heavier b quark, the interactions of spectator quarks are expected to be less important than for charm hadrons and this is supported by evidence that the B^0 lifetime, $1.2^{+0.5}_{-0.4}$ ps [Wagner 90], agrees with the average lifetime for B hadrons, 1.2 ± 0.1 ps [Ong 87], a weighted average of many experiments.

The spectator-model decay width for b decay to c is analogous to that of muon decay,

$$\Gamma(b \to cW^*) = \frac{G_F^2 M_b^5}{192\pi^3} |V_{cb}|^2 \times \text{(phase space factor)}, \tag{3.7}$$

where M_b is the b-quark mass. The relatively long lifetime observed for B hadrons indicates that the magnitude of the KM matrix element V_{cb} is quite small, 0.05 ± 0.01 [Ong 87]. Even rarer, the decay of b quarks to u quarks has been observed in e^+e^- experiments at the $\Upsilon(4S)$ resonance to be suppressed by a factor proportional to the square of $|V_{ub}/V_{cb}| = 0.10 \pm 0.01$ [Albrecht 90a, Fulton 89]. This measurement

is model dependent and the error quoted is purely statistical. The presence of leptons with momenta too large to come from charm-less B decay indicates that the $\Upsilon(4S)$ decays to other final states than $B\overline{B}$, leading to unknown systematic errors in the determination of V_{ub}. The production of these non-$B\overline{B}$ states also affects the measurements of the B-hadron semileptonic branching ratio.

Using the spectator model, Figure 3.5, we estimate the B-hadron semileptonic branching ratio for comparison with the measured values in Sections 3.3.1 and 7.1. The final state of B-hadron decay consists of the decay products of the virtual W boson as well as one hadron containing the spectator quark(s) and either a c or a u quark. A W^+ can decay to a pair of leptons or quarks from any of the accessible doublets, $e^+\nu_e$, $\mu^+\nu_\mu$, $\tau^+\nu_\tau$, $u\bar{d}$ or $c\bar{s}$, where the quarks come in three different colors. If we naively count the number of final states, we expect one ninth of the decays to be semileptonic, for each lepton variety. When the model is corrected for phase-space suppression of the heavy tau and charm final states [Cortes 82] and for the QCD effects of first-order gluon radiation and hard gluon exchange, the predicted semi-electronic and semi-muonic branching ratios each become 15% [Gilman 86]. There are numerous more sophisticated models for B decay, motivated by the fact that the measured values for the semileptonic branching ratios are smaller than the spectator-model predictions.

3.3.1 Measurements of Leptons from B Decay

The semileptonic decays of B mesons have been extensively studied in e^+e^- annihilation near the $\Upsilon(4S)$ resonance, at the CESR and DORIS storage rings. We use the results from these studies in our simulation of B decays. The momentum spectra of electrons and muons are shown in Figure 3.6. There are contributions from both primary $b \to (c \text{ or } u)l\nu$ and secondary $b \to c \to sl\nu$ decays of B mesons. To extract the semileptonic branching ratios, $B(B \to Xl\nu)$, from such spectra, theoretical input is used to model the effect of leptons with momenta too small to measure and leptons from secondary decays. The average of the published branching-ratio measurements listed in Table 3.2, weighted by the statistical and systematic errors combined in

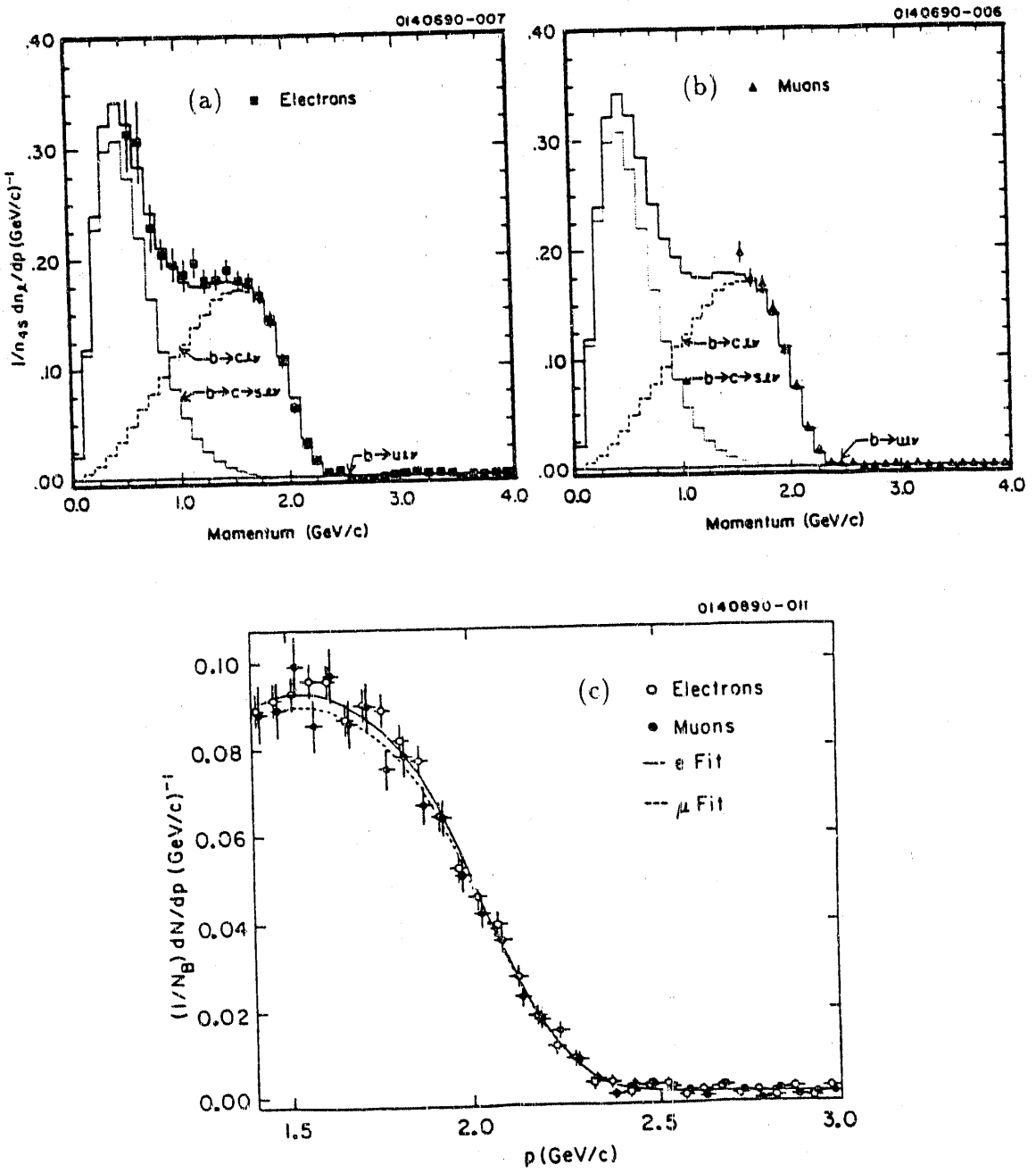

Figure 3.6: Lepton momentum distributions from the $\Upsilon(4S)$ and fits to the data for (a) e and (b) μ from CLEO and (c) from ARGUS. CLEO shows the sum (solid) of the theoretical predictions for the contributions from primary (dashed) and secondary (dotted) B decays to charm. ARGUS subtracts the estimated contributions from secondary B decays to charm. Both groups subtract estimates of the contributions from $B \to J/\psi \to l^+l^-$ [Cassel 90].

Experiment	Reference	$B(B \to Xl\nu)$ in %	l
CLEO	[Behrends 87]	$11.0 \pm 0.3 \pm 0.5 \pm 0.5$	$e\,\mu$
Crystal Ball	[Wachs 89]	$11.7 \pm 0.4 \pm 1.0$	μ
CUSB	[Klopfenstein 83]	$13.2 \pm 0.8 \pm 1.4$	e
CUSB	[Levman 84]	$11.2 \pm 0.9 \pm 1.0$	μ

Table 3.2: Measurements of the B meson semileptonic branching ratios at the CESR and DORIS storage rings. The first error is statistical and the second error is systematic. The third error listed by CLEO is the systematic error due to uncertainties in the theoretical models used to extract the branching ratio.

quadrature, is $11.3\% \pm 0.5\%$. Recent measurements from ARGUS and CLEO indicate that the semileptonic branching ratio is even smaller, $10.3\% \pm 0.1\% \pm 0.2\%$ [Albrecht 90b, Fulton 90a, Fulton 90b]. All of the above branching ratios are calculated with $B(\Upsilon(4S) \to B\overline{B}) = 100\%$. Preliminary CLEO results from dileptons lead to the upper limit, $B(\Upsilon(4S) \to \text{non-}B\overline{B}) < 12\%$ at 90% confidence level [Cassel 90].

The semileptonic branching ratios of B hadrons have also been measured in e^+e^- annihilation experiments at higher center-of-mass energy, assuming the standard-model value for the fraction of bottom-quark events, f_b (Equation 1.6). The weighted average of the PEP and PETRA measurements of the semileptonic branching ratios of B hadrons listed in Table 3.3 is* $11.9\% \pm 0.6\%$. Using the semileptonic branching ratios obtained at the $\Upsilon(4S)$, these measurements could be re-interpreted as measurements of the fraction of bottom-quark events in hadronic events at PEP and PETRA, f_b. The measured $b\bar{b}$ fraction is approximately $(11.9\% \pm 0.6\%)/(11.3\% \pm 0.5\%) = 1.05 \pm 0.07$ times the standard-model value. To make the comparison between the measurements at the $B\overline{B}$ threshold energy and those far above it, we assume that the compositions of B hadrons are similar at the two energies or that the semileptonic branching ratios of the produced B mesons and B baryons are approximately equal. This calculation ignores the small systematic effects due to charm in $c\bar{c}$ events and secondary b decays.

*The average of twelve out of the fourteen branching fraction measurements is $11.2\% \pm 0.6\%$, leaving out the high values obtained by TPC in the μ channel and by DELCO in the e channel.

Experiment	Reference	$B(B \to Xl\nu)$ in %	l
CELLO	[Behrend 83]	$14.1 \pm 5.8 \pm 3.0$	e
CELLO	[Behrend 83]	$8.8 \pm 3.4 \pm 3.5$	μ
DELCO	[Pal 86]	$14.9^{+2.2}_{-1.9}$	e
HRS	[Ng 88]	$10.8 \pm 0.8 \pm 1.3$	e
JADE	[Bartel 87]	$11.7 \pm 1.6 \pm 1.5$	μ
MAC	[Stone 83]	$11.3 \pm 1.9 \pm 3.0$	e
MAC	[Stone 83]	$12.4 \pm 1.8 \pm 2.2$	μ
MARK II	[Ong 88]	$11.2 \pm 0.9 \pm 1.1$	e
MARK II	[Ong 88]	$11.8 \pm 1.2 \pm 1.0$	μ
MARK J	[Adeva 83]	$10.5 \pm 1.5 \pm 1.3$	μ
TASSO	[Althoff 84b]	$11.1 \pm 3.4 \pm 4.0$	e
TASSO	[Althoff 84a]	$11.7 \pm 2.8 \pm 1.0$	μ
TPC	[Aihara 85a]	$11.0 \pm 1.8 \pm 1.0$	e
TPC	[Aihara 85b]	$15.2 \pm 1.9 \pm 1.2$	μ

Table 3.3: Measurements of the B-hadron semileptonic branching ratios at the PEP and PETRA storage rings. The first error is statistical and the second error is systematic.

3.3.2 Simulation of B Decay

We take the branching fraction for primary B-hadron decay to electrons or muons to be $B(B \to Xl\nu) = 11\% \pm 1\%$. The lepton momentum spectra in the Monte Carlo simulation of hadronic Z decays are tuned to agree with the spectra recorded by CLEO, shown in Figure 3.6(a) and (b).

3.4 Sources of Leptons in Hadronic Z Decays

The Monte Carlo simulation of hadronic Z decays contains leptons from many different sources. The simulated uds events contain electrons and muons from π and K decays as well as electrons from photon conversions in the material of the detector. The $c\bar{c}$ events additionally contain leptons from semileptonic decays of charm hadrons. Similarly, the additional sources of electrons and muons in $b\bar{b}$ events are

from primary semileptonic decays of bottom hadrons and from secondary cascade decays via charm hadrons or τ leptons.

The simulation includes hadrons misidentified as leptons for events of all flavors.

3.5 Detector Simulation

All the generated Monte Carlo events are passed through a simulation of the trigger and the detector. To mimic the effect of beam-induced backgrounds, we mix the signals from each MC event with the signals from one of many background events recorded at random beam crossings during the same time period as Z candidates.

The signals of particles passing through the various elements of the Mark II detector are simulated with the known uncertainties and inefficiencies. For the study of leptons, the responses of the liquid argon calorimeter and the muon system to leptons, photons and hadrons are especially important.

In the LA, electromagnetic energy deposits are obtained from a library of signals generated by a simulation of electron-photon cascades (EGS4) [Nelson 85]. Hadronic interactions are simulated with a library of signals from pions in tau-pair events recorded at PEP (HINT2) [Gan 87].

In the muon system, a simple model generates hits for muons and for hadrons which punch through the layers of absorber. To improve on this simulation, we apply corrections to the generated distribution of hits in the four layers. The corrections are based upon experimental data on the muon chamber efficiencies and the punch-through probabilities, as described in Chapter 5 and Appendix A. The resulting efficiencies for misidentifying hadrons as muons are then checked against a detailed simulation of hadronic interactions (FLUKA87) [Aarnio 86, Ranft 86, Nelson 85], which was found to describe well hadrons in hadronic events recorded with the Mark II detector at PEP.

Chapter 4

Hadronic Z Decays

Hadronic Z decays are characterized by high multiplicities of charged tracks and large fractions of the available energy deposited in the detector. Figure 4.1(a) shows a hadronic event with 21 charged tracks (prongs) and 70 GeV of reconstructed energy from charged and neutral particles forming back-to-back jets. Most hadronic Z decays are unmistakably distinct from events produced by other processes: events from Z decays to lepton pairs very rarely contain more charged tracks than the six-prong tau-pair event illustrated in Figure 4.1(b), and events from two-photon exchange and beam-gas interactions deposit energy at small angles with respect to the beam pipe, outside the fiducial volume of the calorimeters.

We select hadronic events with seven or more charged tracks and a visible energy greater than 15% of the center-of-mass energy, $E_{\rm cm}$. The visible energy is the sum of the energies from both the momentum measurements of charged particles and the energy measurements of neutral particles. Charged tracks in the DC are selected if they originate within a cylinder of radius 1 cm and length 6 cm along the beam axis, centered at the e^+e^- collision point. These tracks are used only if they are measured to have $|\cos\theta| < 0.85$, momenta transverse to the beam axis greater than 0.150 GeV/c and total momenta, p, less than the beam energy. Tracks with $p > 10$ GeV/c are constrained to originate from the e^+e^- interaction point. Showers in the LA and EC calorimeters are required to have an energy greater than 1 GeV and to satisfy $|\cos\theta| < 0.68$ in the LA and $0.70 < |\cos\theta| < 0.95$ in the EC. We do not include energy deposits which have been associated with a charged track if the energy of the

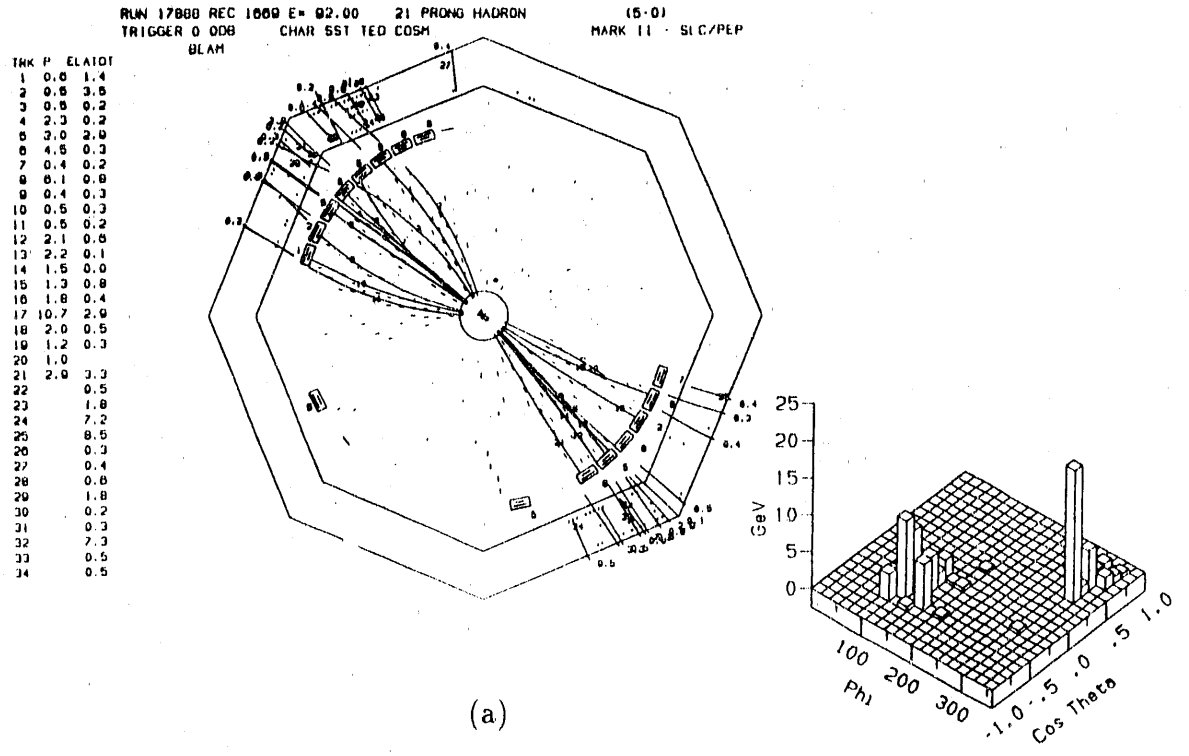

(a)

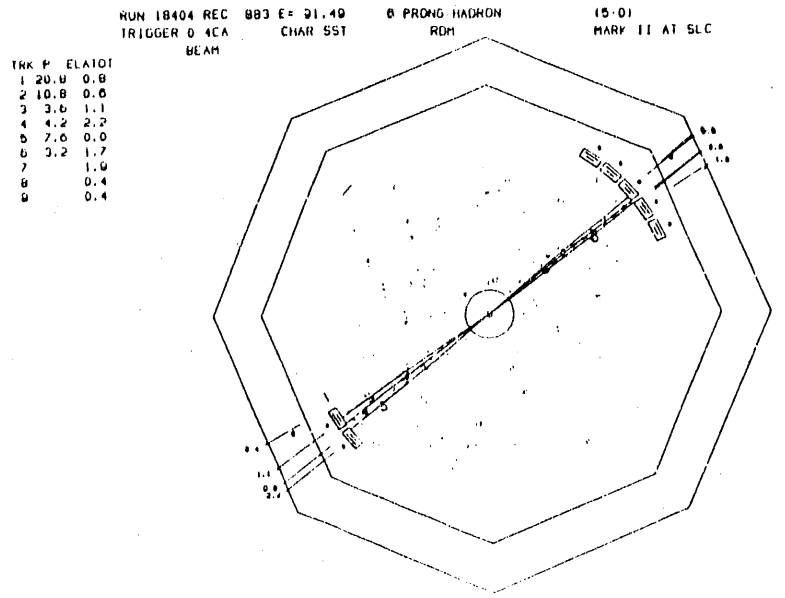

(b)

Figure 4.1: Two Z-decay events: (a) a hadronic event showing charged tracks in the r-ϕ plane and reconstructed energy in the ϕ-$\cos\theta$ grid, and (b) an event with a pair of tau leptons decaying to three prongs each.

shower corresponds to less than twice the momentum of the charged track.

These cuts select 413 hadronic events. The corresponding efficiencies are estimated by Monte Carlo simulations based on the Webber-Marchesini parton-shower model with cluster fragmentation (BIGWIG 4.1) [Marchesini 84, Webber 84] and the Lund parton-shower model with string fragmentation (JETSET 6.3 shower) [Sjöstrand 86, Sjöstrand 87, Bengtsson 87]. We use the average of the two models as the prediction to be compared with data, and the difference between the two models as the estimate of the systematic error due to model dependence. The resulting efficiencies are 0.86 ± 0.02 for detecting produced *udsc* events and 0.88 ± 0.02 for produced $b\bar{b}$ events, as calculated from the numbers of hadronic Monte Carlo events in Table 4.1.

Flavor	Webber-Marchesini	Lund	Both models
udsc	$14149/16804 = 0.842$	$14731/16855 = 0.874$	$28880/33659 = 0.858 \pm 0.002$
$b\bar{b}$	$4130/4704 = 0.878$	$4321/4870 = 0.887$	$8451/9574 = 0.883 \pm 0.003$
udscb	$18279/21508 = 0.850$	$19052/21725 = 0.877$	$37331/43233 = 0.863 \pm 0.002$

Table 4.1: The numbers of generated Monte Carlo events passing the hadronic event selection and the resulting efficiencies. The statistical errors for ratios of numbers, shown here and in the following chapters, are obtained from the binomial distribution [James 80]. In calculating the systematic error on the ratio, we use the largest model difference of ± 0.016, found for *udsc* events.

Using other Monte Carlo simulations [Jadach 85, Behrends 86], we estimate the numbers of events from non-hadronic Z decays and two-photon interactions in the sample to be 0.04 and 0.01, respectively. We estimate that the number of events due to beam-gas interactions and cosmic rays in the sample is < 0.4, based on observing no events when we displace the center of the cylinder defined for the origin of charged tracks by more than its full length along the beam axis.

Chapter 5

Inclusive Lepton Analysis

We tag bottom-hadron event candidates in the hadronic event sample with isolated charged tracks identified as leptons. This chapter describes the isolation criterion for charged tracks reconstructed in the central drift chamber and the methods for identifying leptons. Electrons are identified as tracks with large energy-deposits in the front of the liquid argon barrel calorimeters and muons are identified as tracks which penetrate through the hadron absorber to the outer layers of the muon system. First for electrons and then for muons, we calculate the probability for an isolated lepton track to be identified as a lepton, the probability for an isolated hadron track to be misidentified as a lepton, and the errors on these probabilities, to be used in Chapter 6 for the determination of the efficiency for tagging $b\bar{b}$ events.

5.1 Track Isolation Criterion

We define the track isolation criterion to separate $b\bar{b}$ events from *udsc* events. Because of the larger rest mass of the b quark as compared to *udsc* quark masses, leptons from semileptonic B hadron decays receive larger momenta in the parent hadron rest frame than those from decays of hadrons containing the lighter quarks. This results in larger momenta transverse to the direction of the parent hadron for leptons in b jets than for leptons in *udsc* jets.

To determine transverse momenta, we approximate the directions of the parent b quarks with the directions of the hadronic jets. In the analysis done at $E_{\rm cm} = 29$ GeV

[Nelson 83a], the jet directions were defined to be along the direction of the thrust axis. Because the jets are more collimated and the strong coupling constant is smaller, the angular error introduced by reconstructing the parent hadron direction is smaller at 91 GeV than at 29 GeV, as can be seen in the second and third columns of Table 5.1.

	Thrust axis		Nearest cluster	
Events	29 GeV	91 GeV	29 GeV	91 GeV
$udscb$	20°	14°	11°	6°
$b\bar{b}$	14°	11°	11°	5°
2-jet	13°	7°	11°	6°

Table 5.1: Average angle between the reconstructed jet direction and the parent hadron direction. The jet direction is estimated by either the thrust axis or the nearest cluster for simulated events for $E_{\rm cm}$= 29 GeV and for $E_{\rm cm}$= 91 GeV. The events labelled '2-jet' are events for which the Lund cluster algorithm found two clusters.

However, at 91 GeV, the lepton momenta are larger by about a factor of three compared to those at 29 GeV, and the effect of these angular errors on the transverse momenta becomes significant. To reduce these errors, instead of using the thrust axis, we use the Lund cluster algorithm [Sjöstrand 83] to find the jet directions from the momentum vectors of the charged and neutral particles in each event. When the jet resolution parameter is set equal to its default value, $d_{\rm join} = 2.5$, we observe an average jet multiplicity of 3.0, with 21% of the detected hadronic events having 4 or more jets. The last two columns of Table 5.1 show that the added degrees of freedom, obtained from using clusters rather than the thrust axis to reconstruct the jet directions, substantially reduce the errors in estimating the parent hadron direction.

We then define the transverse momentum of each track with respect to the nearest cluster formed by the other charged and neutral particles in the event, $p_t = p \sin\theta_j$, where θ_j is the angle between the track and the cluster (j) closest to the track. To separate leptons that are products of bottom-hadron decay from leptons that are products of primary charm-hadron decay, we choose a cut in p_t from the spectra of

Figure 5.1. We call a track isolated if it has $p_t > 1.25$ GeV/c.

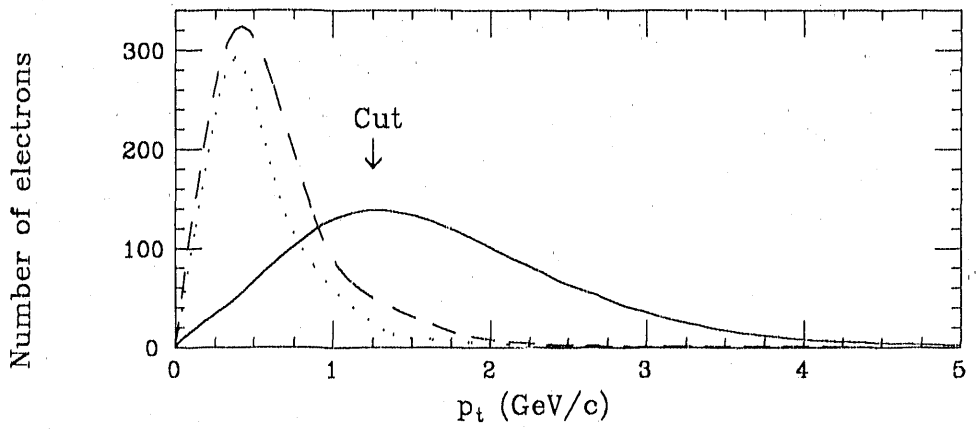

Figure 5.1: Transverse momentum spectra of Monte Carlo-generated electrons from primary bottom-hadron decay (solid line), secondary bottom-hadron decay (dashes) and primary charm-hadron decay (dots). We define isolated electrons to have $p_t > 1.25$ GeV/c.

For electron and muon identification, we consider isolated reconstructed charged tracks (defined in Chapter 4) which have momenta greater than 2 GeV/c and which point from the DC to either the LA calorimeter or the muon system.* The p_t distribution of all tracks with $p > 2$ GeV/c pointing to the LA or muon systems in the data is compared with predictions from the two Monte Carlo models in Figure 5.2. Because the amount of data is insufficient to distinguish between the models, we use the average of the two models as the prediction to be compared with data, and the difference between the two models as the estimate of the systematic error due to model dependence.

5.2 Electron Identification

To obtain a pure sample of electrons, we need to efficiently identify electrons while rejecting hadrons. Separation is possible since electrons lose energy differently from other stable charged particles while passing through matter. Our method is adapted

*The minimum momentum required for a muon to penetrate to the outer layer of the muon system at normal incidence is about 1.8 GeV/c.

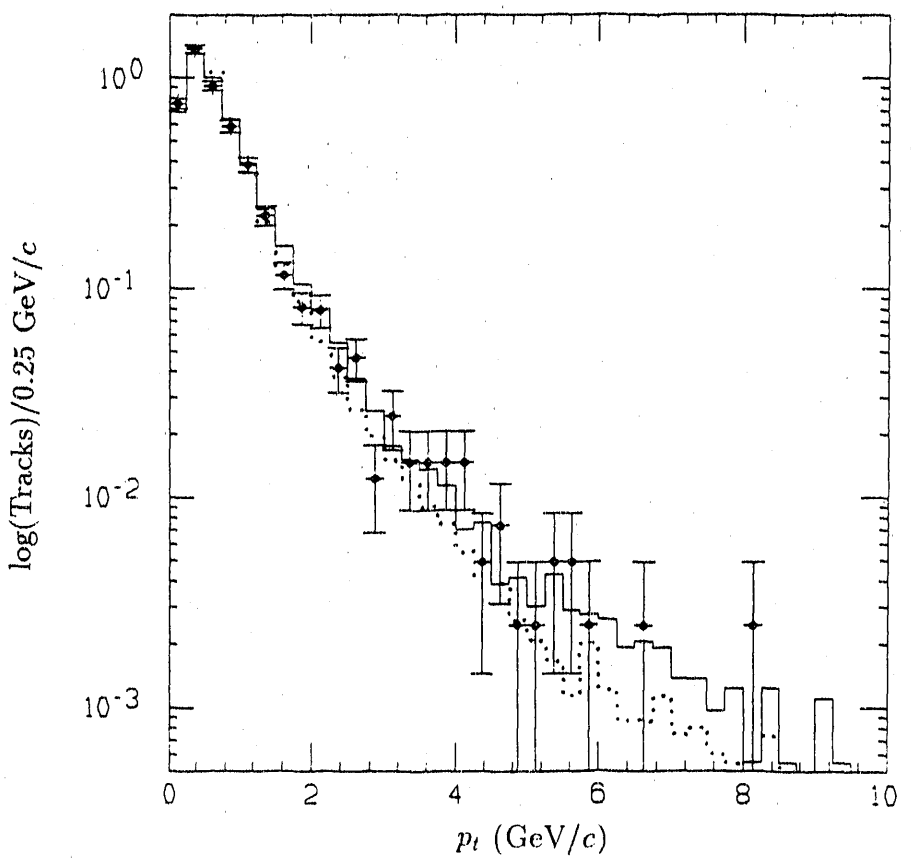

Figure 5.2: The p_t spectra of tracks with $p > 2$ GeV/c pointing to the LA or muon systems in the data (circles), the Webber-Marchesini model (solid), and the Lund model (dots). Isolated tracks considered for lepton identification have $p_t > 1.25$ GeV/c.

from the procedures developed for electron identification with the LA calorimeter at PEP [Nelson 83a, Nelson 83b].

5.2.1 Method for Identifying Electrons

Electrons above the critical energy, 7 MeV in lead, lose energy principally by bremsstrahlung, radiating photons which in turn interact with matter to either create electron-positron pairs or to eject single electrons from atoms via Compton scattering. The result is an electromagnetic cascade shower. The length of such a shower is related to the radiation length in the absorber, namely 0.56 cm in lead. The energy lost through bremsstrahlung is inversely proportional to the square of the mass of the particle; hence, little energy is lost through this process for charged particles heavier than the electron. Instead, hadrons lose their energy by nuclear interactions, producing hadronic showers with a longitudinal extent related to the nuclear interaction length, namely 17 cm in lead.

To distinguish between electrons and hadrons, the electron identification algorithm uses the fact that hadronic showers are spatially much more extended than electromagnetic showers. Electrons are identified by requiring that a large fraction of their energy, as determined from the momentum measurement in the DC, is deposited in the front half (seven radiation lengths) of the LA calorimeter. This requirement works well for identifying single electrons, but leads to too many hadrons misidentified as electrons in hadronic jets. Misidentification in jets comes largely from overlap of charged particles with electromagnetic deposits from photons, most of which are decay products of neutral pions. To reduce this background from overlapping neutral deposits, we require large energy-deposits in narrow roads around the DC track extrapolation in all three orientations of strips in the front section of the calorimeter.

After a discussion of the calibration of the electron identification algorithm, we calculate the identification efficiency and misidentification probability for isolated tracks in hadronic Z decays.

5.2.2 Calibration of the Electron Algorithm

We calibrate the identification algorithm on known electrons from Bhabha scattering, recorded in the upgraded Mark II detector at the PEP storage ring. For each track, we calculate $r_i = E_i/p$, where E_i is the energy deposited in a particular strip orientation of the front half of the calorimeter and $i = 1$–3 represents the readout layers F1+F2, T1 and U (which measure the ϕ, θ and u coordinates as shown in Table 2.1 of Section 2.6). The energies E_i are calculated by adding the energies deposited in a narrow road around the DC track extrapolation. The width of the road is calculated from the formula

$$w_{\text{road}} = w_{\text{shower}} + w_{\text{gang}} |\tan(\psi)|, \tag{5.1}$$

where w_{shower} represents the typical width of an electromagnetic shower ($\simeq$ 3 cm), w_{gang} reflects the additional width arising from the separation of the front and back of a ganged layer ($\simeq$ 4–7 cm), and ψ is the angle, between the track extrapolation and the normal of the layer, projected onto the plane perpendicular to the orientation of the strips.† To reduce misidentification from overlap in the denser jets at the SLC, we have narrowed w_{gang} by a factor 0.6 from the values used at PEP, leading to the widths in Table 5.2. The resulting distributions of r_i for the Bhabha electrons are

Layer	w_{shower}	w_{gang}	Strip width
F1, F2	0.75	0.5	3.5 cm
T1	0.75	0.9	3.5 cm
U	0.70	0.9	5.4 cm

Table 5.2: Values used to define w_{road} in units of strip width.

shown in Figure 5.3.

The electron identification criteria are defined with respect to the median values of r_i and $\sum r_i$ for the calibration electrons, since these medians represent typical electron signals. The medians of the r_i distributions and of $\sum r_i$ are given for three different momentum ranges in Table 5.3. We require each value r_i to be at least 55%

†We use $|\tan(\psi)| = |\tan(\phi - \frac{\pi}{4}m + \frac{\pi}{8})|$, $|\tan(\theta - \frac{\pi}{2})|$ and $|\tan(\phi - \frac{\pi}{4}m + \frac{\pi}{8}) - \tan(\theta - \frac{\pi}{2})|$ for the respective layers F, T and U, where $m = 1$–8 is the LA cryostat module number.

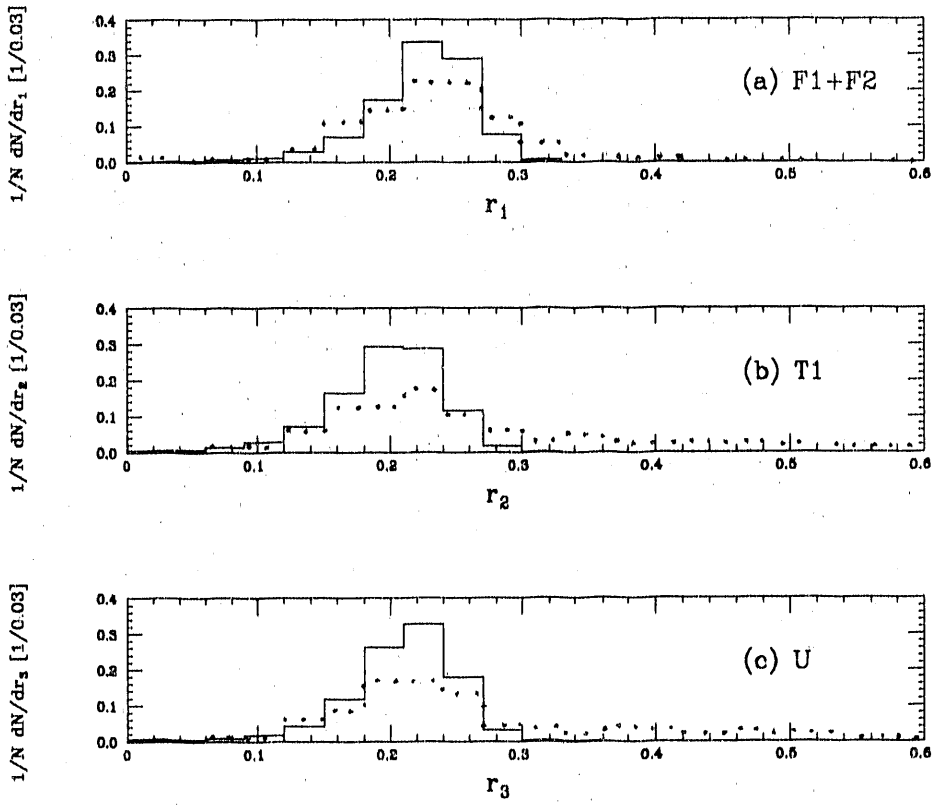

Figure 5.3: The ratios E/p in the layers (a) F1+F2, (b) T1 and (c) U for Bhabha electrons with $13 < p < 16$ GeV/c (solid) and radiative Bhabha electrons with $3 < p < 8$ GeV/c (dots) recorded with the upgraded Mark II detector at PEP.

p range (GeV/c)	r_1 (F1+F2)	r_2 (T1)	r_3 (U)	$\sum r_i$ (F1+F2+T1+U)
3–8	0.235	0.235	0.235	0.725
8–13	0.235	0.210	0.220	0.665
13–16	0.230	0.205	0.215	0.645

Table 5.3: Median r_i and $\sum r_i$ for radiative ($p < 13$ GeV/c) and non-radiative ($p > 13$ GeV/c) Bhabha electrons at PEP used in defining electron identification cuts.

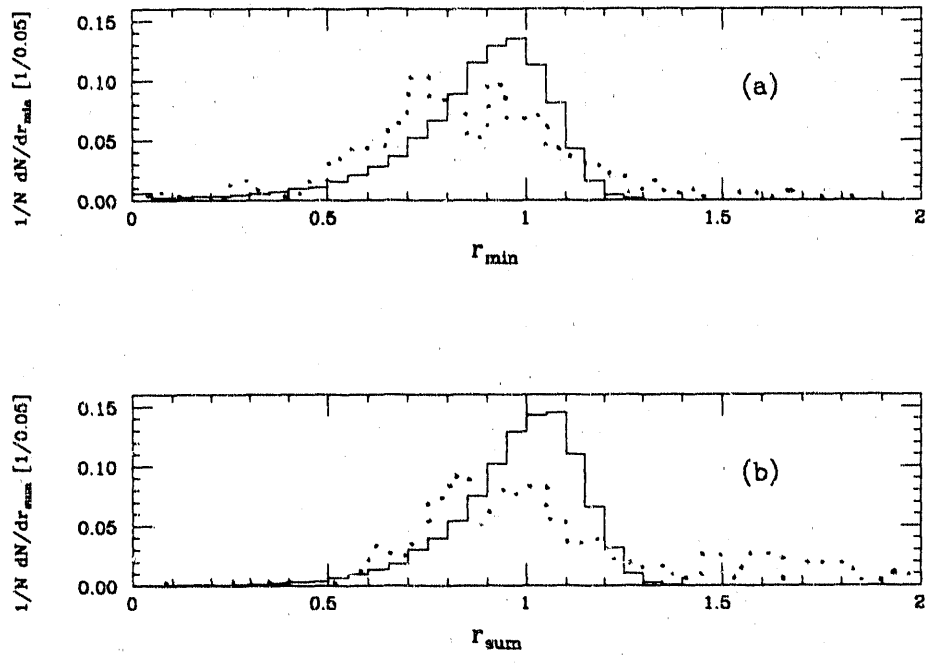

Figure 5.4: Distributions of (a) $r_{\rm min}$ and (b) $r_{\rm sum}$ for Bhabha electrons with $13 < p < 16$ GeV/c (solid) and radiative Bhabha electrons with $3 < p < 8$ GeV/c (dots) recorded with the upgraded Mark II detector at PEP. Identified electrons satisfy $r_{\rm min} > 0.55$ and $r_{\rm sum} > 0.65$.

of the median value for the calibration electrons and $\sum r_i$ to be at least 65% of the median value for the sum.[‡] These requirements can be concisely stated as $r_{\rm min} > 0.55$ and $r_{\rm sum} > 0.65$, where $r_{\rm min} = \min(r_i/\text{median } r_i)$ and $r_{\rm sum} = (\sum r_i/\text{median } \sum r_i)$ are shown in Figure 5.4.

5.2.3 Electron Identification Efficiency

A large fraction of tracks in hadronic events fail electron identification by failing the LA fiducial criterion, that the DC track extrapolation be contained within 1.5 units of strip width from the edges of the F1, F2 and T1 layers. This criterion is well-simulated in the Monte Carlo: the fraction of reconstructed tracks[§] with $p > 2$ GeV/c which are inside the LA fiducial volume is 0.726 ± 0.001 in the MC and 0.74 ± 0.01 in the

[‡] For tracks with $p < 3$ GeV/c or with $p > 16$ GeV/c, we use the normalization constants from the 3 GeV/$c < p < 8$ GeV/c or 13 GeV/$c < p < 16$ GeV/c ranges, respectively.

[§] Reconstructed tracks satisfy $|\cos\theta| < 0.85$ as defined in Chapter 4.

data.

The efficiency for identifying isolated electron tracks pointing to the LA in hadronic events is 0.83 ± 0.05, as calculated from the numbers of isolated MC electron tracks in Table 5.4.

Particle	Webber-Marchesini	Lund	Both models
Electron	$388/465 = 0.834$	$292/356 = 0.820$	$680/821 = 0.828 \pm 0.014$
Non-electron	$91/13192 = 0.0069$	$76/10709 = 0.0071$	$167/23901 = 0.0070 \pm 0.0006$

Table 5.4: The numbers of isolated electron and non-electron tracks identified as electrons in the Monte Carlo. The denominators are the numbers of tracks with $p > 2$ GeV/c and $p_t > 1.25$ GeV/c which point to the LA fiducial volume, and the numerators are the subsets of these tracks which satisfy $r_{\rm min} > 0.55$ and $r_{\rm sum} > 0.65$.

5.2.4 Electron Misidentification Probability

The main source of contamination of the electron sample is a combination of interacting hadrons and overlapping neutral deposits. We represent this background in the MC hadronic events by combining signals from pions in tau-pair events recorded at PEP with simulations of electron-photon cascades (ECS4) [Nelson 85]. Figure 5.5 is a comparison between the cut in the identification variables $r_{\rm min}$ and $r_{\rm sum}$ for isolated tracks in the data and in the MC, indicating the predicted contribution from real electrons.

The probability for isolated non-electron tracks to be misidentified as electrons is 0.007 ± 0.004, as calculated from the numbers of isolated MC non-electron tracks in Table 5.4.

The p_t spectrum for tracks identified as electrons is shown in Figure 5.6, together with predictions for the contributions from real electrons and hadrons misidentified as electrons. There are 10 isolated tracks identified as electrons in the data, two of which are in the same event. Of these 10 tracks, 2.0 are expected to come from hadrons misidentified as electrons. Figure 5.7 is a picture of an event with an isolated electron.

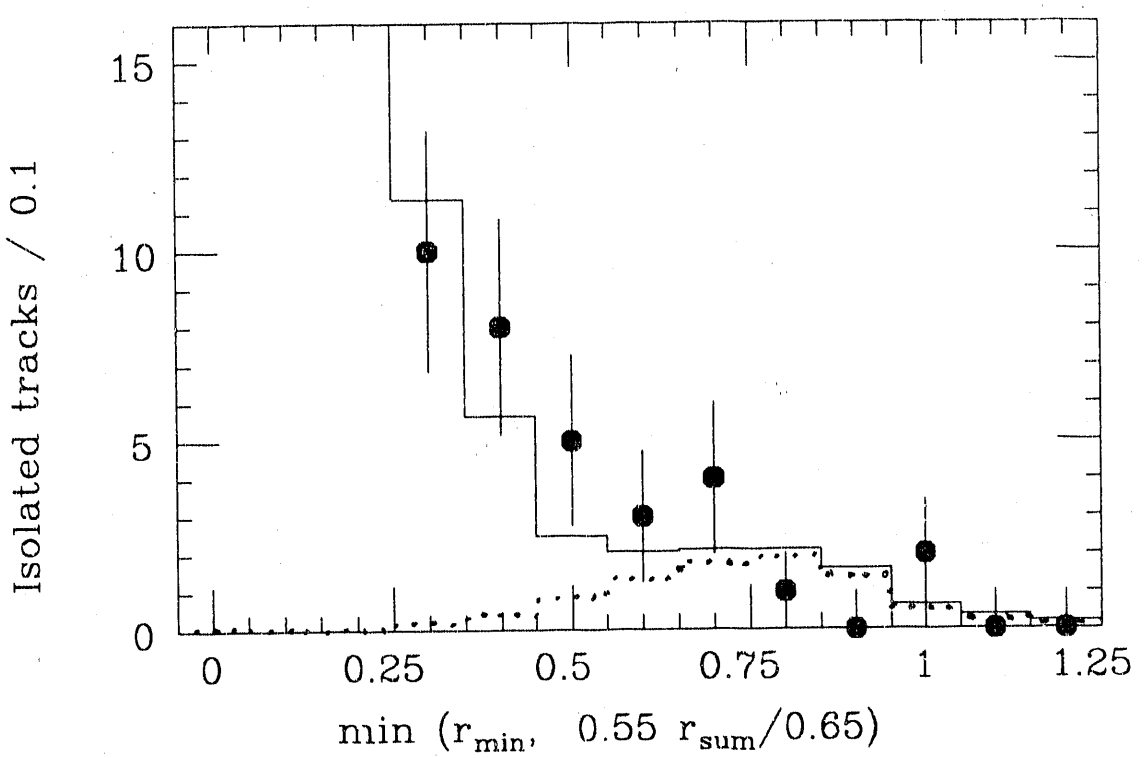

Figure 5.5: Comparison of electron identification variable in the data (circles) and the MC (solid) for isolated tracks. The dotted histogram is the prediction for real electrons. Identified electrons have $\min(r_{\rm min}, 0.55 r_{\rm sum}/0.65) > 0.55$.

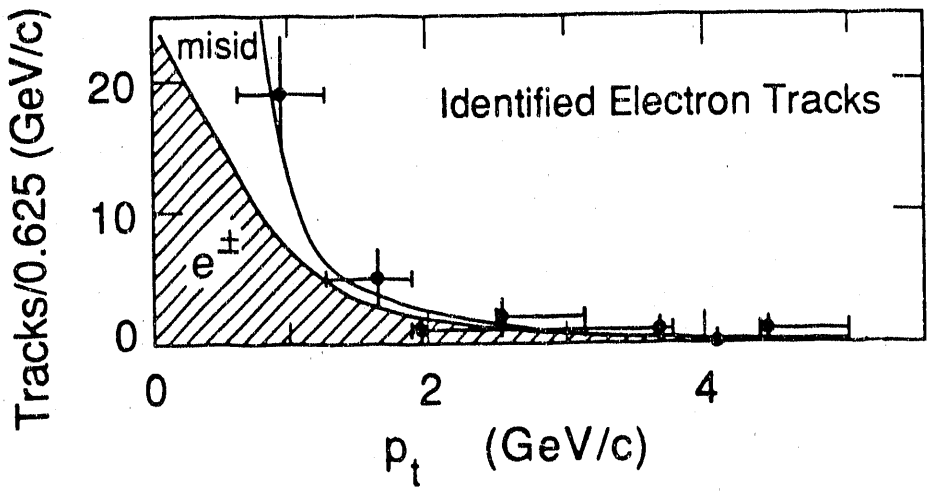

Figure 5.6: The p_t spectrum for tracks identified as electrons. The shaded and unshaded regions show the expected contributions from real electrons and hadrons misidentified as electrons, respectively. The predictions come from MC simulations normalized to 413 observed hadronic events, assuming $r_b = 0.22$. Isolated electron tracks have $p_t > 1.25$ GeV/c.

5.3 Muon Identification

To obtain a pure sample of muons, we need to efficiently identify muons while rejecting hadrons. Separation is possible since muons penetrate matter further than other stable charged particles. Our method is adapted from the procedures developed for muon identification with the muon system at PEP [Nelson 83b, Ong 88].

5.3.1 Method for Identifying Muons

Muons with energies above a few hundred MeV experience energy loss, dE/dx, by ionizing atoms and molecules in a material at an approximately uniform rate, which is 12 MeV/cm in iron. Since the relatively large mass of the muon suppresses bremsstrahlung, muons do not deposit their energy in electron-photon showers like electrons do. Although both muons and charged hadrons undergo similar dE/dx losses, only charged hadrons lose energy through nuclear interactions, since muons do not interact strongly. The nuclear interaction length in iron is the same as in lead, 17 cm. Thus, while 2-GeV muons penetrate more than seven interaction lengths of iron, most

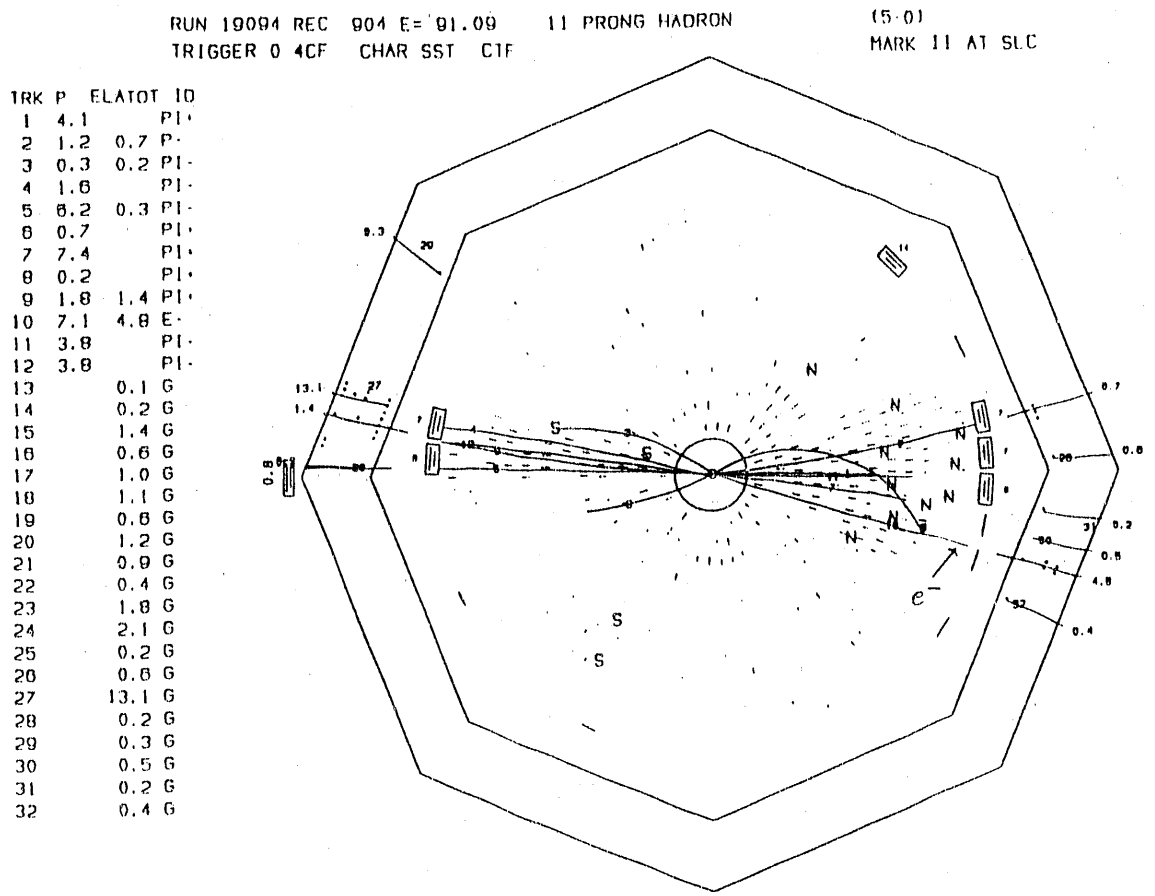

Figure 5.7: Hadronic Z-decay event with an isolated electron shown with charged tracks and neutral showers in the r-ϕ plane. Track number 10 has $p = 7.1$ GeV/c, $p_t = 1.5$ GeV/c, $r_{\rm min} = 0.73$ and $r_{\rm sum} = 0.75$.

charged hadrons are absorbed in this amount of iron, in which they produce hadronic showers.

To distinguish between muons and hadrons, the muon identification algorithm uses the fact that while muons penetrate matter, hadrons produce showers in matter. Muons are identified as tracks which penetrate through the seven interaction lengths of absorber, leaving hits in all four layers of the muon system. Misidentification comes from hadron punch through, track overlap and noise hits. Requiring that each of the hits be located near the DC track extrapolation greatly reduces these backgrounds. We also require correlated hits in the outer three layers of the muon system, thereby further reducing misidentification from beam-induced noise in these layers.

After a discussion of the calibration of the muon identification algorithm, we calculate the identification efficiency and misidentification probability for isolated tracks in hadronic Z decays.

5.3.2 Calibration of the Muon Algorithm

We calibrate the identification algorithm on known muons from cosmic-ray events and on muon-pair events recorded in the upgraded Mark II detector at the PEP storage ring. For each track, we look for hits in the muon-chamber proportional tubes (which are described in Section 2.8) within a search region around the DC track extrapolation. The search region width is 3σ, where σ is the rms error of track extrapolation.¶

We use $\sigma^2 = \sigma^2_{\text{scatt}} + \sigma^2_{\text{res}}$, where σ_{scatt} is the error due to multiple Coulomb scattering and σ_{res} is the combined resolution of the muon chambers and the DC tracking. The amount of multiple Coulomb scattering for a particle incident on a piece of material in the detector depends on the particle momentum as well as the material thickness. The rms scattering angle is approximated as

$$\Theta = \frac{21\,\text{MeV}/c}{p\beta}\sqrt{\frac{t}{X_0}}, \tag{5.2}$$

¶In the analyses done at PEP [Nelson 83b, Ong 88], the search region was defined to be 2σ. Our wider region (3σ) is less sensitive to misalignments. The beam-induced noise levels in the outer layers of the muon system are much higher at the SLC than at PEP. To better reject noise hits in layers 2–4, we have added the requirement that these hits be correlated, as is explained on pages 64–66 of this section.

where β is the velocity of the incident particle, t is the thickness of the material and X_0 is its radiation length. The multiple-scattering contributions due to each of the detector elements, the magnet coil ($1.3X_0$), the LA calorimeter ($15X_0$) and the hadron absorbers (14–$18X_0$/layer), are added in quadrature. The error in the measured coordinate is

$$\sigma^2_{\text{scatt}} = \frac{1}{2}\sum_i \Theta_i^2(\frac{t_i^2}{3} + t_i d_i + d_i^2), \tag{5.3}$$

where d_i is the distance following element i to the given layer and the factor 1/2 arises from projecting Θ onto a plane. The typical position error for a 2-GeV muon due to multiple scattering is 5 cm at the first layer of the muon system and 10 cm at the fourth layer.

We use cosmic rays, recorded with the Mark II at the SLC, to calculate the error at each layer due to the resolution of the muon chambers (about 2.5 cm/$\sqrt{12}$ = 0.7 cm) and the DC track extrapolation. These resolution errors are smaller than at PEP, due to the superior drift chamber at the SLC, especially in the z coordinate. Figure 5.8 shows the distance between the track extrapolation and the nearest hit, divided by σ, for cosmic-ray muons. The values of σ_{res} for each layer and chamber orientation were adjusted to produce an rms hit-to-track distance of 1σ. The resulting σ_{res} obtained from a fit of the peak position and width of a Gaussian to the hit-distance distributions of Figure 5.8 are listed in Table 5.5. The offsets of about $+\sigma/2$ in the peak position of the y-coordinate measurements are the same for the chambers in both the East and the West walls. The effect of these offsets on the muon identification efficiency is small for the large (3σ) search width used here.

The search width around the DC track extrapolation in the outer layer can be quite large for tracks with small momenta. Empirically, for $p < 10$ GeV/c, $\sigma \simeq 20/p(\text{GeV}/c)$ cm in the fourth layer. To better reject noise hits in the outer layer, which is important in the noisy SLC environment, we use a smaller search region about the path defined by the associated hits in the second and third layers, thus demanding that the hits in the outer layers be correlated [Weir 88]. This search region is $3\sigma_{\text{corr}}$, where σ_{corr}, the rms deviation of hits in the fourth layer from this path, is typically 1 to 3 cm.

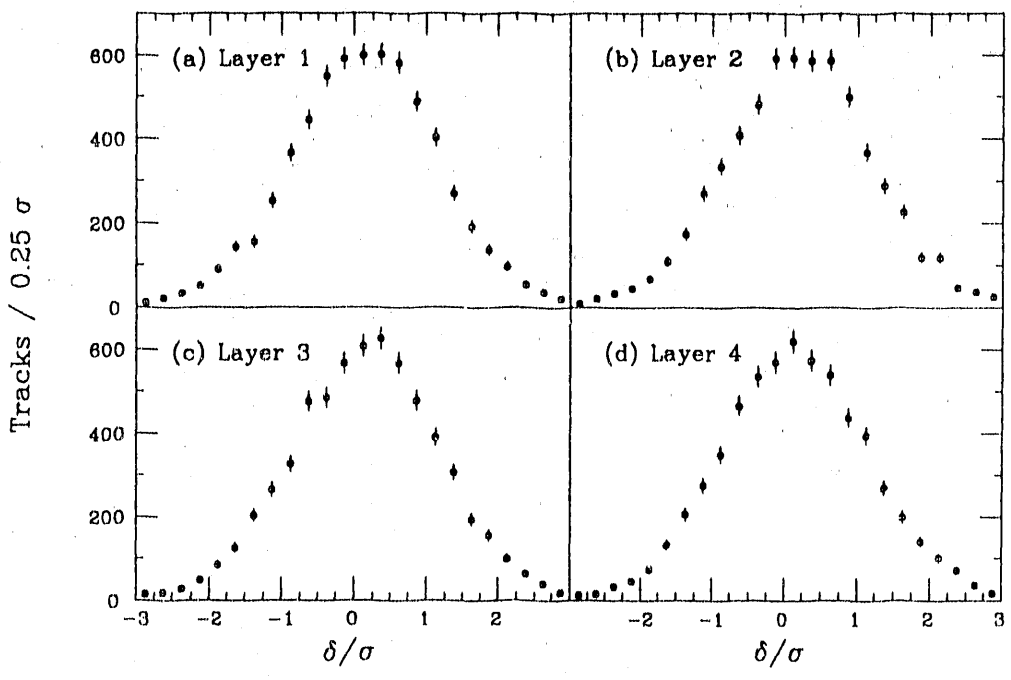

Figure 5.8: The distance between the track extrapolation and the nearest muon-chamber hit, δ, divided by σ for cosmic-ray muons. The values of $\sigma_{\rm res}$ used to calculate σ are listed in Table 5.5.

Layer number	Chamber orientation	Measured coordinate	$\sigma_{\rm res}$ (cm)	Peak (σ)	Width (σ)
1	East/West	z	1.1	0.02	0.98
2	East/West	y	1.4	0.68	1.02
3	East/West	y	1.4	0.53	1.00
4	East/West	y	1.7	0.46	1.00
1	Top/Bottom	z	0.9	0.14	0.98
2	Top/Bottom	x	0.8	0.23	0.99
3	Top/Bottom	x	0.8	0.15	0.98
4	Top/Bottom	x	0.9	0.13	0.99

Table 5.5: The values for $\sigma_{\rm res}$ in each layer for the fits that give unit-width Gaussians in the cosmic-ray hit-distance distributions (Figure 5.8).

We determine $\sigma_{\rm corr}$ from cosmic-ray tracks recorded with the Mark II at the SLC, and the result agrees well with muon-pair events recorded at PEP. The rms deviation is parameterized as

$$\sigma_{\rm corr} = \frac{1.47 + 0.74 p_{\rm ext}^{-1.78}}{\cos^{2.68}(\psi)} \text{ cm}, \tag{5.4}$$

where $p_{\rm ext}$ is the geometric mean of the extrapolated momenta at layers 3 and 4 in GeV/c, and where ψ is the angle in radians, between the track extrapolation and the normal of layer 4, projected onto the plane perpendicular to the orientation of the proportional tubes.

The deviations, divided by $\sigma_{\rm corr}$, are shown for cosmic rays in Figure 5.9. Part of

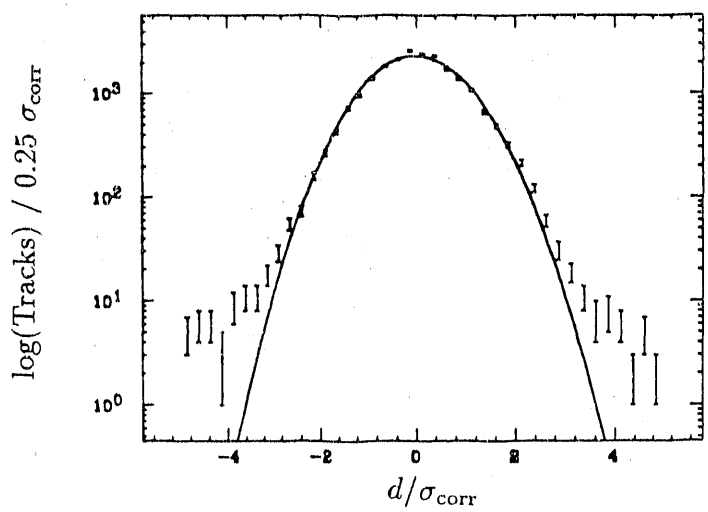

Figure 5.9: The deviation between the path defined by the associated hits in layers 2 and 3 and the associated hit in layer 4, d, divided by $\sigma_{\rm corr}$ for cosmic-ray muons. The solid line is a unit-width Gaussian [Weir 88].

the non-Gaussian tails are due to tracks with multiple hits in a layer.

A track is identified as a muon if hits are found in all four layers of the muon system within 3σ of the extrapolated DC track and if the associated hit in the fourth layer is within $3\sigma_{\rm corr}$ of the path defined by the second and third layers. In the following sections, we estimate the identification efficiencies and punch-through probabilities using the variable `MUSTAT` which contains a bit pattern of the layers which have associated hits within 3σ of the DC extrapolation. The bits are ordered such that the least significant bit corresponds to the first layer. That is, tracks with a hit in

only the first layer have MUSTAT $= 1 = 0001_2$, tracks with hits in the first three layers have MUSTAT $= 7 = 0111_2$, and muon candidates are required to have MUSTAT $= 15 = 1111_2$. In addition, muon candidates need to have a correlated hit in layer four, described by defining the variable $\mathtt{MUSTAT}_{cr}$, whose most significant bit also reflects this additional requirement. The values of the variable $\mathtt{MUSTAT}_{cr}$ are the same as those of MUSTAT when MUSTAT < 8. For $\mathtt{MUSTAT}_{cr}$ to be ≥ 8, the fourth hit has to be both within 3σ and within $3\sigma_{corr}$. Thus, identified muons satisfy $\mathtt{MUSTAT}_{cr} = 15$.

5.3.3 Muon Identification Efficiency

The majority of tracks in hadronic events fail muon identification by failing the muon-system fiducial criteria, that the DC track extrapolation be contained within the edges of the fourth layer and that the track momentum be sufficient to penetrate to the fourth layer. The minimum momentum for tracks at normal incidence to the absorbers is about 1.8 GeV/c. These criteria are well-simulated in the Monte Carlo: the fraction of reconstructed tracks[‖] with $p > 2$ GeV/c which are inside the muon fiducial volume is 0.429 ± 0.002 in the MC and 0.42 ± 0.01 in the data.

Muons that satisfy the fiducial criteria can fail to be identified if they scatter out of the active volume or the 3σ search region in some layer, if they fail to penetrate to the outer layer because of larger-than-average dE/dx losses, if their trajectory is poorly reconstructed in the DC, or if the proportional tubes fail to fire due to electronic inefficiencies. All of these effects are incorporated in the Monte Carlo simulation. However, the proportional-tube inefficiency was set to 1% per layer in the MC, significantly smaller than the $3\% \pm 1\%$ measured with muon-pair events at PEP [Nelson 83b].

We estimate the difference in efficiencies between the data and the MC by counting the number of tracks failing in only one layer, tracks with MUSTAT $= 14$, 13, 11 or 7. In Table 5.6, we calculate the efficiencies in each layer for MC Z decays to muon pairs and for energetic cosmic rays recorded at the SLC. The average per-layer inefficiency is 0.013 ± 0.007 in the MC and 0.041 ± 0.004 in the cosmic-ray data. To account for this difference, we add the inefficiency $\epsilon_{add} = 0.029 \pm 0.008$ per layer to

[‖]Reconstructed tracks satisfy $|\cos\theta| < 0.85$ as defined in Chapter 4.

Layer	$\mu^+\mu^-$ MC			Cosmic-ray data		
number	One missing	Ineff'cy	Efficiency	One missing	Ineff'cy	Efficiency
1	0.020	0.020	0.980	0.036	0.040	0.960
2	0.009	0.009	0.991	0.042	0.048	0.952
3	0.005	0.006	0.994	0.036	0.040	0.960
4	0.016	0.016	0.984	0.032	0.037	0.963
Ave/Tot		0.013	0.950		0.041	0.845

Table 5.6: Calculation of muon-chamber efficiencies in each layer for tracks from simulated muon pairs and observed cosmic rays with $32 < p < 64$ GeV/c. The inefficiency for a layer is defined as the number of tracks with the given layer missing (including tracks missing multiple hits) divided by the total number of tracks. It is obtained by iteration from the ratio labelled 'One missing,' which is defined as the number of tracks with exactly one hit missing in the given layer (i.e. with `MUSTAT` = 14, 13, 11 or 7) divided by the total number of tracks.

the MC, thereby reducing the simulated muon identification efficiency by the factor $(0.845 \pm 0.014)/(0.950 \pm 0.027) = 0.89 \pm 0.03$.

The efficiency for identifying isolated muon tracks that satisfy the muon-system fiducial criteria in hadronic events is 0.79 ± 0.05, as calculated from the corrected numbers of isolated MC muon tracks in Table 5.7.

5.3.4 Muon Misidentification Probability

Misidentification in the muon sample comes from track overlap, noise hits and hadron punch through. The data also contain muons from hadron decay in flight; these muons are realistically simulated in the Monte Carlo [Nelson 83b] and are part of the sample of real muons, as a background to prompt muons from heavy-quark decay. Beam-induced noise hits are simulated well by mixing the signals from each MC event with the signals from a background event; the fraction of tracks inside the muon fiducial volume with an associated hit in the fourth layer, i.e. with `MUSTAT` > 7, is 0.233 ± 0.001 in the MC and 0.23 ± 0.01 in the data. The simulation of hadron punch through is only good to a factor of two, as was learned from studies with a detailed hadronic interaction simulation (FLUKA87) [Aarnio 86, Ranft 86, Nelson 85], which was found

Particle	Webber-Marchesini	Lund	Both models
Muon	238.3/297 = 0.802	207.1/266 = 0.779	445.4/563 = 0.791 ± 0.013
Non-muon	49.1/7917 = 0.0062	42.1/6328 = 0.0067	91.2/14245 = 0.0064 ± 0.0007

Table 5.7: Corrected numbers of isolated muon and non-muon tracks identified as muons in the Monte Carlo. The corrections, for the additional proportional-tube inefficiencies calculated in Section 5.3.3 (on page 67), and for the additional hadron punch-through probabilities outlined in Section 5.3.4 (on pages 69–70), are described in detail in Appendix A. The denominators are the numbers of tracks with $p > 2$ GeV/c and $p_t > 1.25$ GeV/c which satisfy the muon-system fiducial criteria, and the numerators are the subsets of these tracks which satisfy $\texttt{MUSTAT}_{cr} = 15$. The uncorrected ratios are $501/563 = 0.890 \pm 0.014$ for MC muons and $91/14245 = 0.0064 \pm 0.0007$ for MC non-muons. MC muons from hadron decay in flight are categorized as real muons.

to describe well hadrons in hadronic events recorded with the Mark II detector at PEP [Weir 87].

Using tracks in the data which penetrate to the inner three layers of the muon system, we determine the additional hadron punch-through probabilities to these layers, thus correcting the MC MUSTAT distribution. Table 5.8 lists the probabilities for tracks to reach each layer. The differences between the probabilities in the middle two columns (2 and 3) of Table 5.8 indicate that the punch through to the first three layers is underestimated in the MC by about a factor two. To calculate the effect of this underestimate on the punch through reaching the MUSTAT = 15 signal population, we fit the MC MUSTAT < 15 distribution to the data, resulting in the higher probabilities listed in the last column (4) of Table 5.8. The corrections, for the additional hadron punch-through probabilities outlined here and for the additional proportional-tube inefficiencies calculated in the previous section (on page 67), to the numbers of identified muons predicted by the Monte Carlo are described in detail in Appendix A.

To estimate the number of isolated hadrons misidentified as muons, we correct the numbers of such tracks in the MC by using the probabilities for additional hadrons

Layer number	Probability per track		
	Data	MC	MC fit
1	0.174 ± 0.013	0.118 ± 0.001	0.187 ± 0.001
2	0.064 ± 0.009	0.039 ± 0.001	0.066 ± 0.001
3	0.023 ± 0.006	0.011 ± 0.000	0.025 ± 0.001
4	0.028 ± 0.006	0.026 ± 0.001	0.029 ± 0.001

Table 5.8: Probabilities for tracks to reach each layer of the muon system in the data, the uncorrected MC and the corrected MC. The probabilities are calculated by dividing the numbers of tracks which leave hits (within 3σ) in all layers preceding and including the given layer but not in subsequent layers (i.e. tracks with MUSTAT = 1, 3, 7 or 15) by the total numbers of $p > 2$ GeV/c tracks satisfying the muon fiducial criteria. The majority of tracks reaching the fourth layer are real muons.

to punch through to layers 1 to 3 obtained from a fit to the distribution of the non-signal values of the muon identification variable ($\mathtt{MUSTAT}_{cr}$ = 0–14) for all tracks** as well as the additional proportional-tube inefficiencies. The probability for isolated hadrons to punch through to layer 4 is consistent with the probabilities obtained from a detailed study with the full FLUKA87 simulation [Weir 87]. Figure 5.10 is a comparison between $\mathtt{MUSTAT}_{cr}$ for isolated tracks in the data and in the corrected MC, indicating the predicted contribution from real muons.

The probability for isolated non-muon tracks to be misidentified as muons is $0.006^{+0.006}_{-0.003}$, as calculated from the corrected numbers of isolated MC non-muon tracks in Table 5.7. This probability does not include muons from π or K decays in flight, which are categorized as real muons.

The p_t spectrum for tracks identified as muons is shown in Figure 5.11, together with predictions for the contributions from real muons and hadrons misidentified as muons. There are 6 isolated tracks identified as muons in the data. Of these 6 tracks, 0.9 are expected to come from hadrons misidentified as muons. Figure 5.12 is a picture

**To determine the additional inner-layer punch-through probabilities, we use a fit to $\mathtt{MUSTAT}_{cr}$ for *all* tracks instead of the subset of *isolated* tracks, in order to enhance the statistics for the fit. Within our limited statistics, insignificant differences in the estimated misidentification probability for isolated tracks result from using the additional punch-through probabilities obtained from fits to either MUSTAT or $\mathtt{MUSTAT}_{cr}$ and from using either all tracks or only isolated tracks. See Appendix A for details.

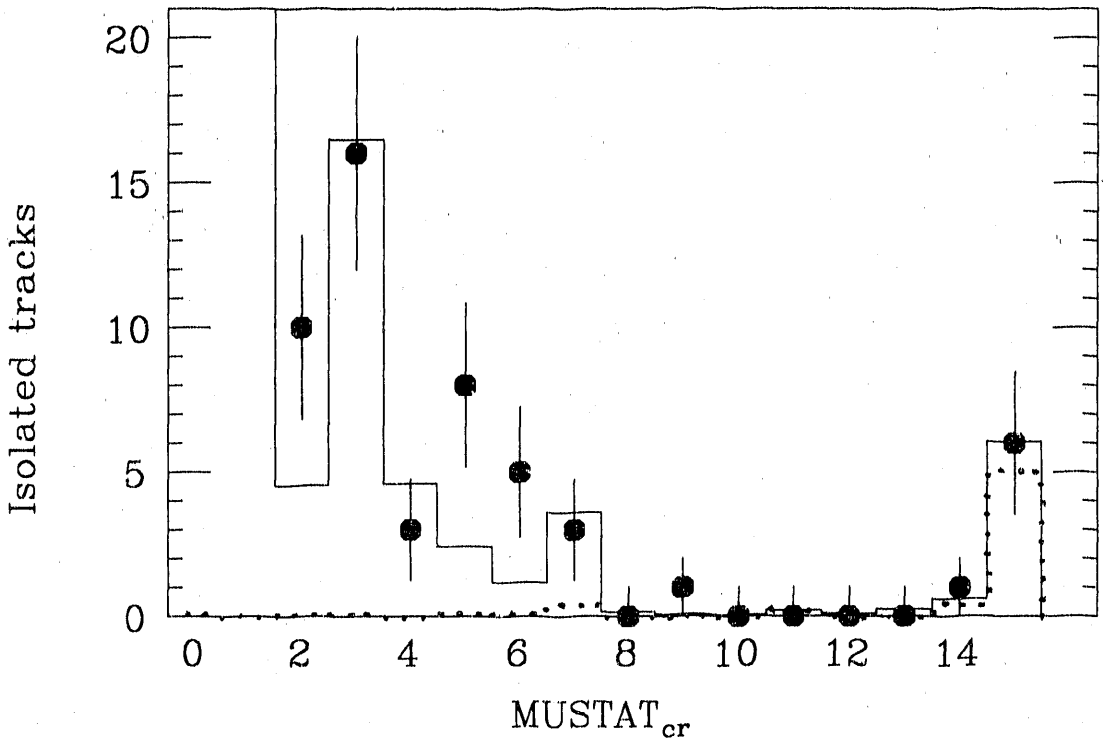

Figure 5.10: Comparison of muon identification variable in the data (circles) and the corrected MC (solid) for isolated tracks. The dotted histogram is the prediction for real muons. Identified muons have $\texttt{MUSTAT}_{cr} = 15$.

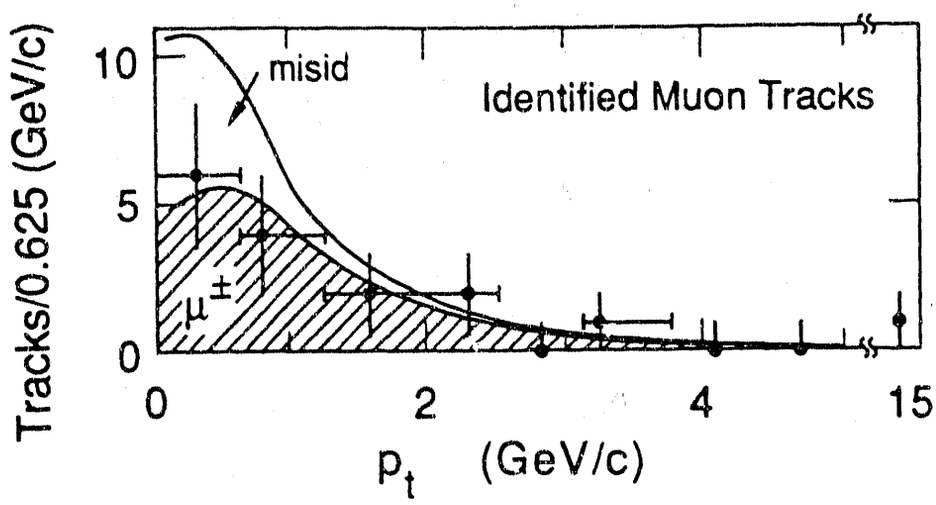

Figure 5.11: The p_t spectrum for tracks identified as muons. The shaded and unshaded regions show the uncorrected expected contributions from real muons and hadrons misidentified as muons, respectively. The predictions come from MC simulations normalized to 413 observed hadronic events, assuming $r_b = 0.22$. The numbers of identified muons have not been corrected for additional inefficiencies or punch through. The net effect of these corrections, evaluated in the footnote on page 92 in Appendix A, is to multiply the numbers of real muons and hadrons identified as muons by the relatively small overall factors of $(1 - \epsilon_{\rm add})^4 = 0.89$ and $652.2/616 = 1.06$, respectively. The reasons for the disagreement between MC and data for tracks with small values of p_t are not understood. For isolated non-muon tracks identified as muons, i.e. misidentified hadrons with $p_t > 1.25$ GeV/c, the overall correction factor is $91.2/91 = 1.00$, as shown in Table 5.7.

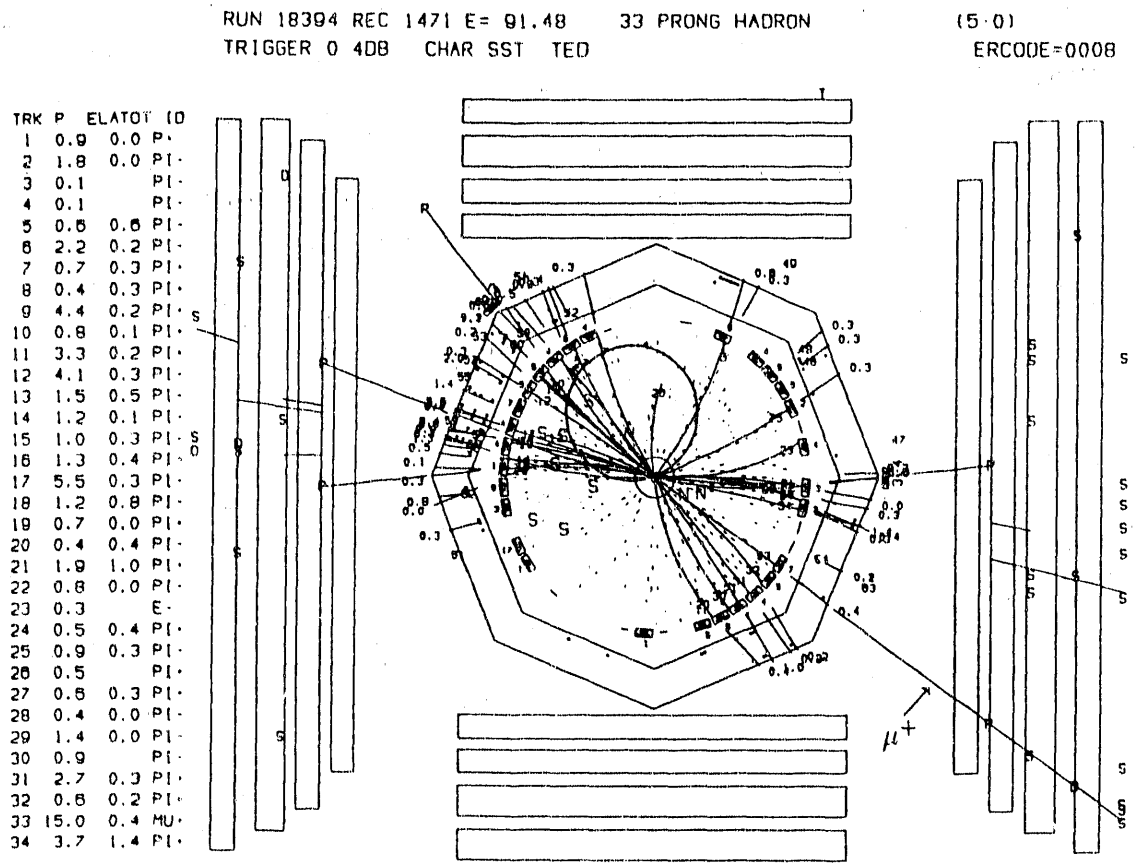

Figure 5.12: Hadronic Z-decay event with an isolated muon shown with charged tracks, neutral showers and muon-chamber hits in the r-ϕ plane. Track number 33 has $p = 15.7$ GeV/c, $p_t = 2.2$ GeV/c, all four associated hits $< 1.3\sigma$ from the DC track extrapolation and a fourth-layer hit at $-1.2\sigma_{\rm corr}$ from the path defined by the associated hits in layers 2 and 3.

of an event with an isolated muon.

Chapter 6

Branching Fraction to B Hadrons

Using the efficiencies for selecting hadronic events calculated in Chapter 4 and the efficiencies for tagging events with isolated leptons calculated here, we determine the bottom-quark fraction in hadronic Z decays, $r_b = \Gamma(Z \to b\bar{b})/\Gamma(Z \to \text{had})$, from its product with the B-hadron semileptonic branching ratio, $B(B \to Xl\nu) \cdot r_b$. The measurement of r_b is used to estimate the Z-boson partial width, vector coupling constant and branching fraction into bottom hadrons.

6.1 Event tagging efficiencies

To separate $b\bar{b}$ events from $udsc$ events, we assign a p_t value to each event containing an identified lepton, and, if an event contains more than one lepton track, we choose the highest value of p_t. Hadronic events which contain at least one identified lepton which is isolated, i.e. has $p_t > 1.25$ GeV/c, are considered tagged. The overall efficiency for tagging produced $b\bar{b}$ events is $0.101^{+0.013}_{-0.012}$. This efficiency, which includes contributions from all sources of identified leptons, results from the combined effects of the hadronic event-selection efficiency, the semileptonic branching ratios, the fiducial acceptances of the detector, the lepton identification efficiencies and the isolation cut. The effect of the cut on p_t, after all other cuts, is to select 46% of $b\bar{b}$ events with a real lepton track identified as a lepton. The cuts retain only a small fraction, $0.011^{+0.004}_{-0.003}$, of produced $udsc$ events. The efficiencies for tagging produced events are calculated from the numbers of tagged Monte Carlo events in Table 6.1. The systematic errors

Flavor	Webber-Marchesini	Lund	Both models
uds	$139/13025 = 0.0107$	$97/13057 = 0.0074$	$236/26082 = 0.0090 \pm 0.0006$
$c\bar{c}$	$69/3779 = 0.0183$	$55/3798 = 0.0145$	$124/7577 = 0.0164 \pm 0.0015$
$udsc$	$208/16804 = 0.0124$	$152/16855 = 0.0090$	$360/33659 = 0.0107 \pm 0.0006$
$b\bar{b}$	$527/4704 = 0.1120$	$438/4870 = 0.0899$	$965/9574 = 0.1008 \pm 0.0032$

Table 6.1: The numbers of generated Monte Carlo events passing the tagged event selection and the resulting efficiencies. The numbers of events tagged by muons are corrected according to the procedure described in Chapter 5 and Appendix A.

for the efficiencies are the sums in quadrature of the uncertainties from the MC statistics, from the MC model differences, and from the identification efficiencies and misidentification probabilities of isolated tracks identified as leptons (in Chapter 5).

6.2 r_b and $B(B \to Xl\nu) \cdot r_b$

Among the 413 hadronic events in the data, we observe 15 high-p_t events, 9 tagged by electrons and 6 by muons. The standard-model prediction is 14.7 tagged events, with 8.3 events from primary B-hadron decays to real leptons and with the quark-flavor and lepton-type composition shown in Table 6.2. Figure 6.1(c) shows the

Event	Leptons		Hadrons		Total
Flavor	e	μ	e	μ	$e+\mu$
uds	0.34	0.23	1.37	0.69	2.63
$c\bar{c}$	0.58	0.39	0.25	0.17	1.38
$b\bar{b}$	6.29	4.03	0.20	0.15	10.68
$udscb$	7.21	4.65	1.83	1.01	14.69

Table 6.2: The predicted quark-flavor and lepton-type composition of tagged events. The columns labelled e and μ contain either real leptons identified as leptons or hadrons misidentified as leptons. The predictions assume $r_b = 0.22$ and are normalized by multiplying the number of MC events by $413/37331 = 0.0111$, the ratio of the number of observed hadronic events in the data to the number in the MC.

observed p_t spectrum together with the expected quark-flavor composition of events

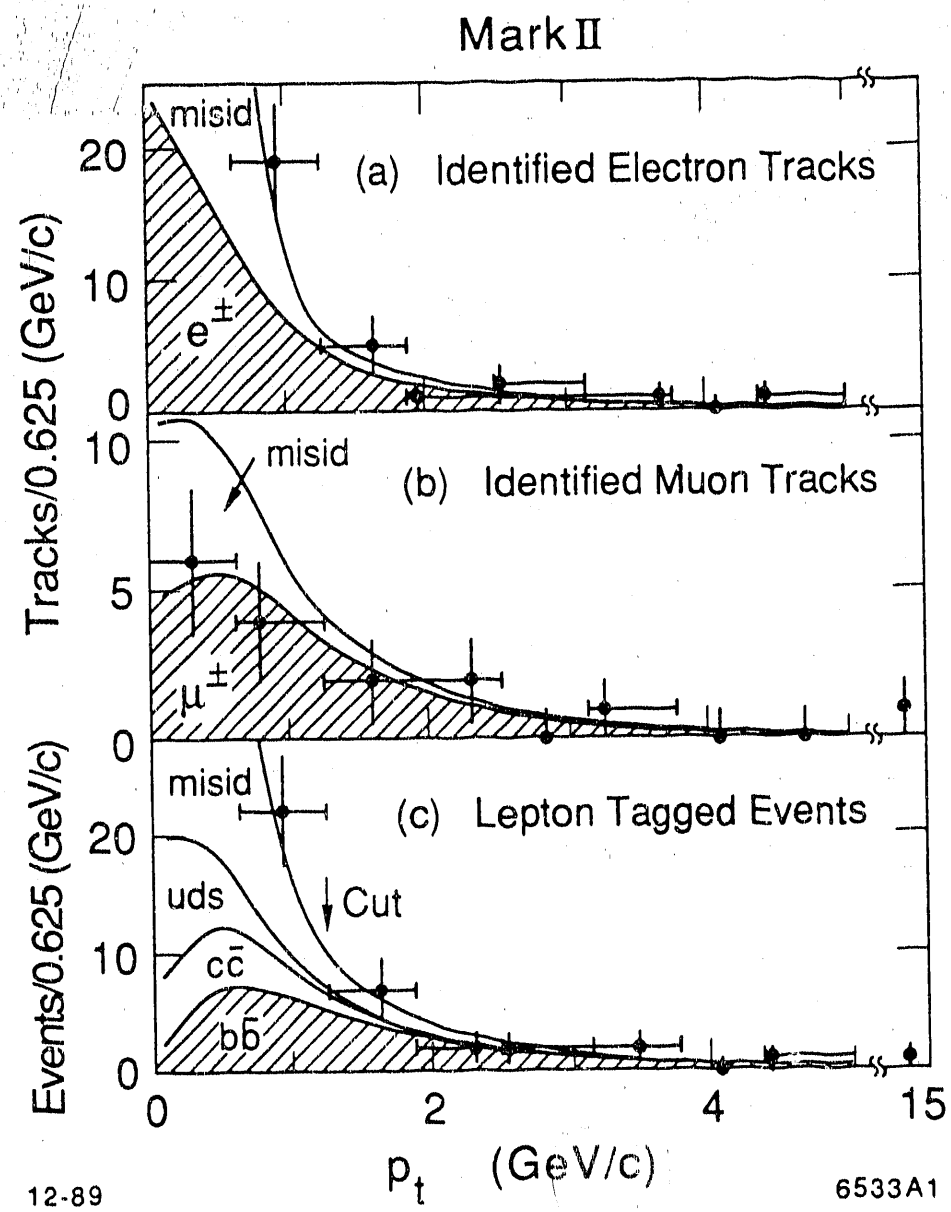

Figure 6.1: The p_t spectra for tracks identified as (a) electrons and (b) muons, reproduced from Figures 5.6 and 5.11. The shaded and unshaded regions show the expected contributions from real leptons and hadrons misidentified as leptons, respectively. (c) The p_t distribution for leptons ($e^{\pm}$ or $\mu^{\pm}$) with one entry per event. The shaded region is the expected contribution from $b\bar{b}$ events with real leptons. Also indicated are the contributions from $c\bar{c}$ and uds events, as well as events tagged by hadrons misidentified as leptons. These predictions come from Monte Carlo simulations normalized to 413 observed events, assuming $r_b = 0.22$. In these spectra, the identified MC muons are uncorrected except in part (c), where the numbers of events tagged by real muons have been corrected for the additional inefficiencies described in Chapter 5.

with a track identified as a lepton. From the observed numbers of hadronic events and tagged events, together with the efficiencies described above, we construct two equations to be solved for the unknown $udsc$ and $b\bar{b}$ populations, as described in Appendix B. The resulting value of $r_b = 0.23^{+0.10}_{-0.08}{}^{+0.05}_{-0.04} \pm 0.02$, where the errors are, in the order quoted, the statistical errors using Poisson statistics, the systematic errors from uncertainties in the event efficiencies and the systematic error from the uncertainty in the B semileptonic branching ratio. The product $B(B \to Xl\nu) \cdot r_b = 0.025^{+0.010}_{-0.009} \pm 0.005$ is independent of the assumed branching ratio* $B(B \to Xl\nu) = 11\% \pm 1\%$. As shown in Figure 6.1, our measurements are in good agreement with the standard-model predictions for which $r_b = 0.22$.

6.3 $\Gamma(Z \to b\bar{b})$, v_b and $B(Z \to b\bar{b})$

The Z-boson partial width, vector coupling constant and branching fraction into bottom hadrons are obtained from the measurement of r_b. We multiply r_b by the average of hadronic-width measurements from the LEP experiments ALEPH, DELPHI, L3 and OPAL, $\Gamma(Z \to \text{had}) = 1.76 \pm 0.02$ GeV [Fernandez 90], to obtain $\Gamma(Z \to b\bar{b}) = 0.40^{+0.17}_{-0.14}{}^{+0.09}_{-0.08}$ GeV. Essentially the same value for the partial width is obtained from the measurements of the total number of produced $b\bar{b}$ events and the luminosity, as is shown in Appendix C. The measured partial width agrees with the standard-model width $\Gamma(Z \to b\bar{b}) = 0.38$ GeV calculated in Table 1.2. Using this calculation, we estimate v_b from $\Gamma(Z \to b\bar{b}) \propto a_b^2 + v_b^2$ by setting the axial coupling constant equal to its standard-model value, $a_b = -1$, as suggested by measurements [Marshall 89] at lower E_{cm}, and arrive at $v_b^2 = 0.56^{+0.65}_{-0.55}{}^{+0.34}_{-0.32}$, in agreement with the standard-model value of 0.48.

We find the Z-boson branching fraction into hadrons containing bottom quarks to be $B(Z \to b\bar{b}) = \Gamma(Z \to b\bar{b})/\Gamma_Z = 16\%^{+7\%}_{-6\%} \pm 3\%$, where the average measured total width $\Gamma_Z = 2.50 \pm 0.02$ GeV [Fernandez 90]. The measured branching fraction is in good agreement with the standard-model value of 15% calculated in Section 1.1.1.

*The relation between r_b and $B(B \to Xl\nu)$ is given in Appendix B.

Chapter 7

Conclusion

In conclusion, we summarize isolated-lepton measurements of the Z-boson branching fraction into bottom hadrons and show progress from bottom-hadron tagging studies with the Mark II vertex detectors, as an example of a future direction for B physics with Z decays.

7.1 Measurements with Isolated Leptons

Before our direct measurement of the bottom-quark fraction in hadronic Z decays, the Z coupling to b quarks was determined from the electroweak induced charge asymmetry. A fit to the measured charge asymmetries for hadronic events enriched in b quarks,* i.e. containing leptons with momenta and transverse momenta above some cuts, from many experiments at PEP and PETRA yields $a_b = -1.02 \pm 0.15$ and $v_b = -0.35 \pm 0.95$ [Marshall 89], as compared to the respective standard-model values of -1 and -0.69.

Direct measurements of the Z coupling to bottom hadrons through isolated leptons from semileptonic B-decays have been performed at SLC and LEP. The weighted average of the measurements of the B-hadron semileptonic branching ratio times the bottom-quark fraction in hadronic Z decays listed in Table 7.1 is $B(B \to Xl\nu) \cdot r_b =$

*Although the fit is actually for the coupling to the quarks d, s and b, it is essentially a determination of a_b and v_b since the b-quark data dominate the result.

Experiment	Reference	$B(B \to Xl\nu) \cdot r_b$	l
Mark II	[Kral 90] (publication of this work)	$0.0252^{+0.0105}_{-0.0089}{}^{+0.0050}_{-0.0049}$	$e\,\mu$
L3	[Adeva 90] updated in [Innocente 90]†	$0.0248^{+0.0008}_{-0.0008}{}^{+0.0012}_{-0.0012}$	μ
ALEPH	[Decamp 90]	$0.0217^{+0.0019}_{-0.0019}{}^{+0.0010}_{-0.0010}$	e
ALEPH	[Decamp 90]	$0.0238^{+0.0028}_{-0.0028}{}^{+0.0012}_{-0.0012}$	μ

Table 7.1: Measurements of the B meson semileptonic branching ratio times the bottom-quark fraction in hadronic Z decays at the SLC and at the LEP storage ring. The first error is statistical and the second error is systematic.

0.0238 ± 0.0011. Dividing by $B(B \to Xl\nu) = 11\% \pm 1\%$, we get $r_b = 0.22 \pm 0.02$, where the error is dominated by the uncertainty in $B(B \to Xl\nu)$. Since measurements of the B-meson semileptonic branching ratios at the $\Upsilon(4S)$ depend on theoretical input to model the effect of leptons with momenta too small to measure and leptons from secondary decays, the uncertainty in r_b could be reduced somewhat by tuning the hadronic Z-decay Monte Carlo to the well-measured high-momentum parts of the lepton spectra, which are the parts that give rise to the high-p_t leptons used to tag B hadrons. The error on r_b will have to be reduced substantially for us to indirectly probe the effect of the top-quark mass on $\Gamma(Z \to b\bar{b})$. The predicted decrease in $\Gamma(Z \to b\bar{b})$ between $m_t = 100$ GeV/c^2 and $m_t = 200$ GeV/c^2 is 2% [Consoli 89].

If we divide the average for $B(B \to Xl\nu) \cdot r_b$ by the standard-model $r_b = 0.217$ [Behrends 89], we obtain an average semileptonic branching ratio of $B(B \to Xl\nu) = 11.0\% \pm 0.5\%$, in good agreement with the previous measurements summarized in Section 3.3.1, $11.3\% \pm 0.5\%$ at CESR and DORIS and $11.9\% \pm 0.6\%$ at PEP and PETRA. The accuracy on the measured value of this branching ratio may be improved through studies of hadronic Z decays containing two isolated leptons.

†Preliminary L3 result.

7.2 Mark II Vertex Tagging

A different approach to studying bottom-hadron production in Z decays is to use the vertex detectors[‡] that were installed and tested inside the Mark II detector during January 1990.

Vertex tagging is possible because of the relatively long average lifetime, large charged-particle multiplicity and large mass of the B hadron. An example of a method for tagging B hadrons is to require three or more tracks in the same hemisphere with impact parameters of more than $+3\sigma$ from the primary vertex position and with an invariant mass larger than 1.95 GeV/c^2 [Hayes 84]. An event is divided into hemispheres by the plane that is perpendicular to the thrust axis and that passes through the primary vertex position. The primary vertex is taken to be the interaction point, as determined from tracks in events recorded during the same time period as the candidate event and from the locations of the electron and positron beams. A positive value for the impact parameter is assigned if the track crosses the two-dimensional projection of the thrust axis in the half-plane containing the track; tracks with large positive impact parameters indicate the presence of long-lived particles. Monte Carlo simulations of the SSVD and the DCVD are used to determine the efficiencies for tagging. The overall efficiency for tagging produced $b\bar{b}$ events is about 0.36 ± 0.03. The cuts retain only a small fraction, approximately 0.009 ± 0.001, of produced $udsc$ events [Weber 89].

While installed inside the Mark II, the DCVD is calibrated using cosmic ray tracks. The position resolution is determined to be 15 μm, added in quadrature to a diffusion contribution of $37\sqrt{D(\text{cm})}$ μm for DCVD gas at 2 atm. To estimate the impact-parameter resolution, we use the distribution of miss distances at the origin for the pair of track-segments formed by cosmic rays traversing the drift chamber. We find an impact-parameter resolution of 30 μm. The pattern-recognition algorithm used to find hits is optimized to provide the best suppression of fake hits while maintaining a single-hit efficiency in excess of 98%. The double-track resolution is studied by superposing pulses recorded from different cosmic-ray events, and then measuring

[‡] Refer to Section 2.12 for descriptions of the silicon strip and drift chamber vertex detectors.

the efficiency of finding the second hit as the separation between the superposed hits is increased. When the separation is larger than about 700 μm, the efficiency for finding the second hit is $> 95\%$ while the probability for finding a fake hit is $< 10\%$ [Durrett 90].

The data sample recorded during January 1990 consists of about 30 hadronic Z events. Within the limited statistics, we find the performances of the SSVD and DCVD to be consistent with expectations from previous tests.

We illustrate the complementary information obtained from lepton identification and vertex reconstruction with two events that are likely to contain B hadrons: a vertex-tagged event and a lepton-tagged event. Figure 7.1 shows an event tagged by three tracks in the upper hemisphere with large impact-parameter significances. The event contains a secondary vertex in the lower hemisphere and two back-to-back muons (μ^+ and μ^-) with moderately large transverse momenta. Figure 7.2 shows an event tagged by an isolated electron (e^-). Back-to-back with the isolated electron is a muon (μ^+) with moderately large transverse momentum. The electron and two other tracks in the upper hemisphere form a secondary vertex.

The Mark II is currently recording SLC data, totalling about 40 hadronic events during July and August, and is scheduled to finish running in October 1990 with a total of 3000 hadronic events. We hope to use the lepton-tagged and vertex-tagged events from this final Mark II data sample to improve our measurements of the average B-hadron lifetime and of the Z-boson branching fraction into hadrons containing bottom quarks.

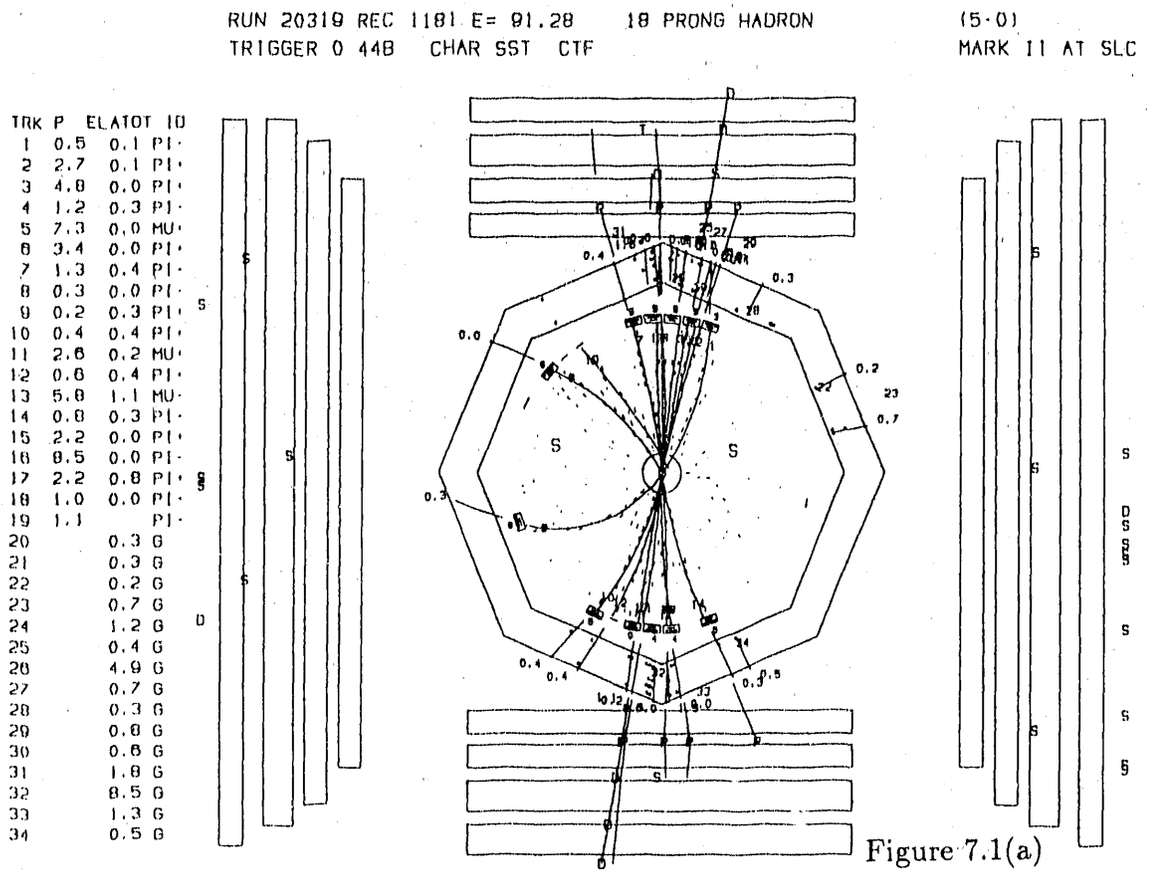

Figure 7.1(a)

Figure 7.1: Vertex-tagged hadronic Z-decay event shown in the r-ϕ plane with (a) charged tracks, neutral showers and muon-chamber hits; (b) charged tracks, DCVD hits and SSVD hits; and (c) track extrapolations to the interaction point. Tracks number 2, 3 and 8 have impact parameters $> +3.6\sigma$ and tracks number 14, 15 and 18 form a secondary vertex. Track number 5 (μ^+) has $p = 7.3$ GeV/c, $p_t = 0.8$ GeV/c, all four associated hits $< 1.4\sigma$ from the DC track extrapolation and a fourth-layer hit at $0.1\sigma_{\rm corr}$ from the path defined by the associated hits in layers 2 and 3. Similarly, track number 13 (μ^-) has $p = 5.8$ GeV/c, $p_t = 1.1$ GeV/c, $> -2.7\sigma$ and $0.3\sigma_{\rm corr}$. Tracks number 13 and 11 (μ_2^+) share associated hits in the outer three layers; we assign these hits to track 13, because its extrapolation is closer to the hits than that of track 11.

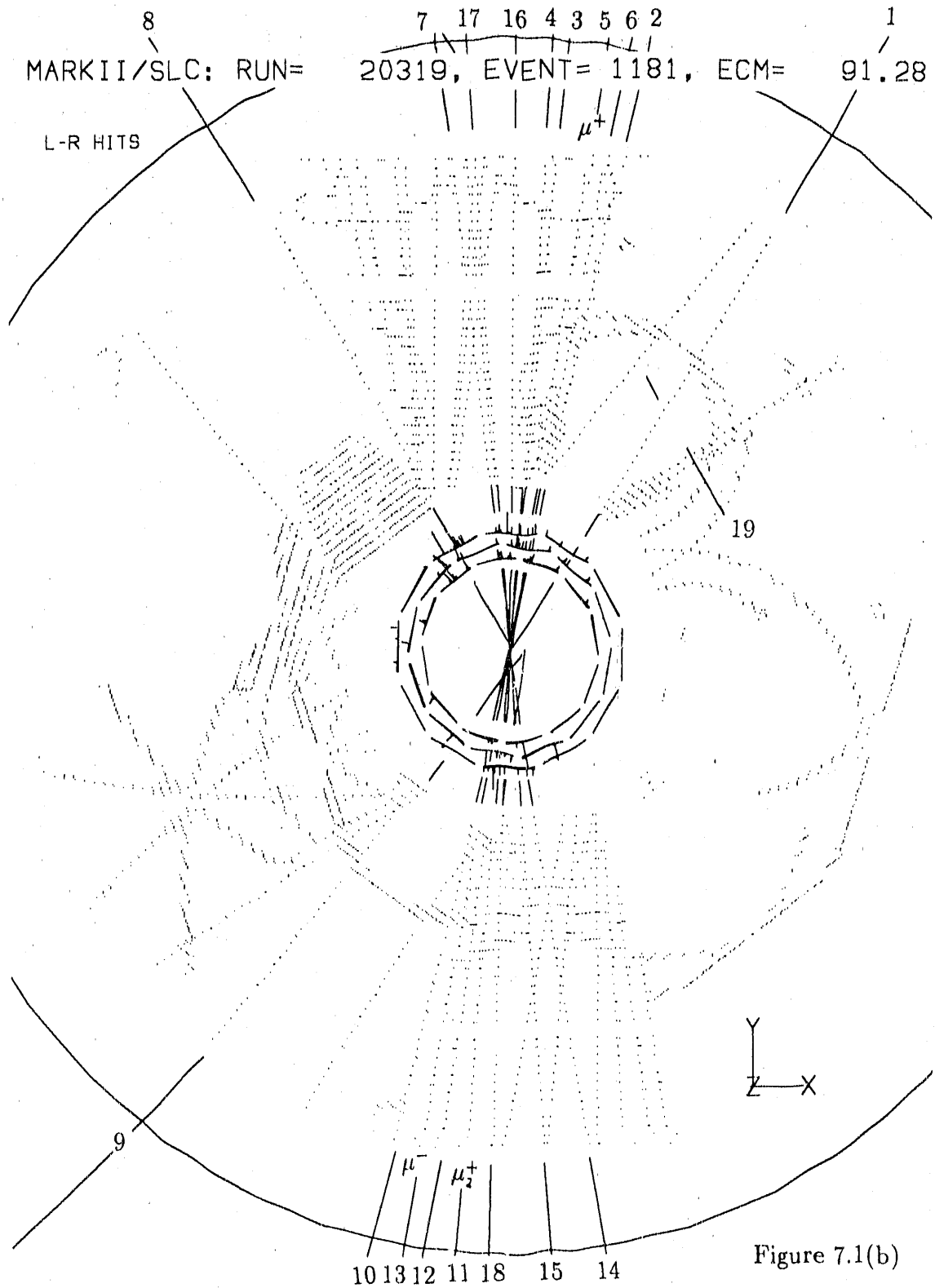
8
7 17 16 4 3 5 6 2
1
MARKII/SLC: RUN= 20319, EVENT= 1181, ECM= 91.28
L-R HITS
μ^+
19
Y
Z
X
9
μ^-
μ_2^+
10 13 12 11 18 15 14

Figure 7.1(b)

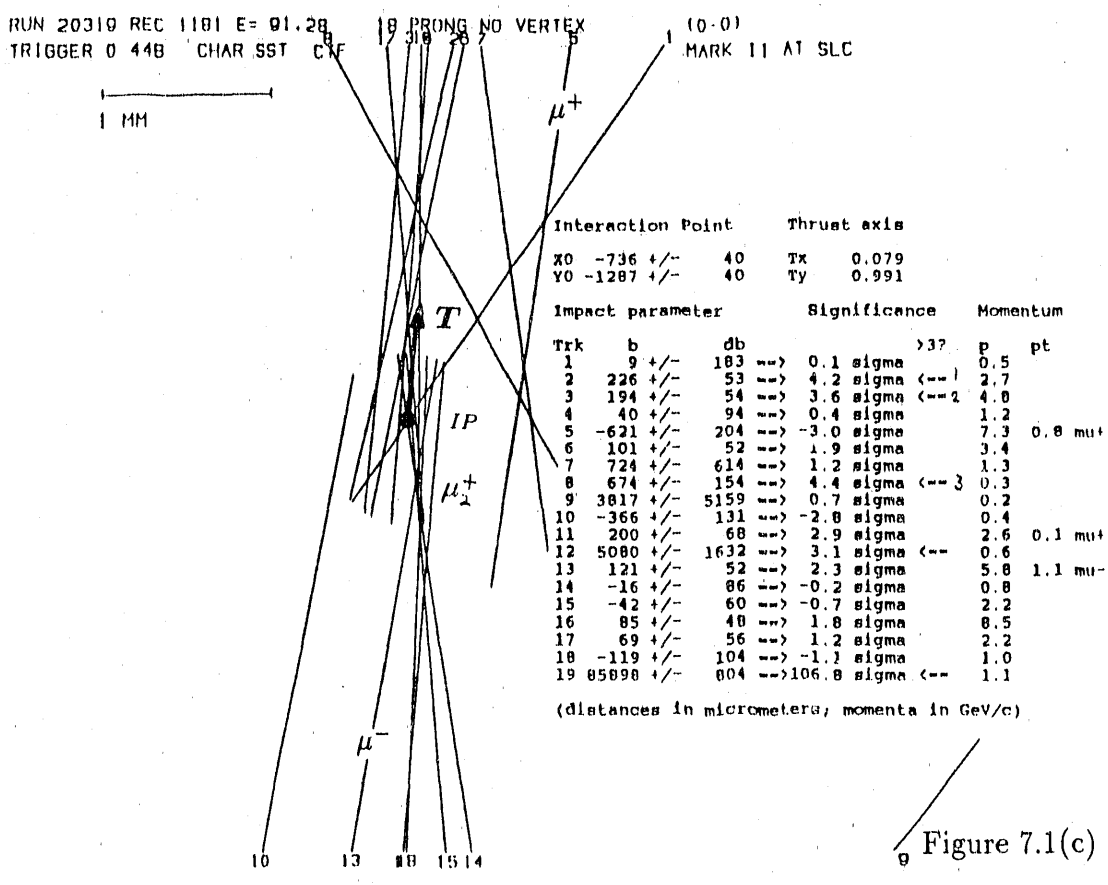
RUN 20319 REC 1181 E= 91.28
TRIGGER 0 448 CHAR SST CVF
19 PRONG NO VERTEX
(0-0)
MARK II AT SLC
1 MM
μ^+
T
IP
μ_2^+
μ^-
10 13 18 15 14 9
Interaction Point Thrust axis
X0 -736 +/- 40 Tx 0.079
Y0 -1287 +/- 40 Ty 0.991
Impact parameter Significance Momentum
Trk b db >3? p pt
1 9 +/- 183 --> 0.1 sigma 0.5
2 226 +/- 53 --> 4.2 sigma <--1 2.7
3 194 +/- 54 --> 3.6 sigma <--2 4.0
4 40 +/- 94 --> 0.4 sigma 1.2
5 -621 +/- 204 --> -3.0 sigma 7.3 0.8 mu+
6 101 +/- 52 --> 1.9 sigma 3.4
7 724 +/- 614 --> 1.2 sigma 1.3
8 674 +/- 154 --> 4.4 sigma <--3 0.3
9 3817 +/- 5159 --> 0.7 sigma 0.2
10 -366 +/- 131 --> -2.8 sigma 0.4
11 200 +/- 68 --> 2.9 sigma 2.6 0.1 mu+
12 5080 +/- 1632 --> 3.1 sigma <-- 0.6
13 121 +/- 52 --> 2.3 sigma 5.8 1.1 mu-
14 -16 +/- 86 --> -0.2 sigma 0.8
15 -42 +/- 60 --> -0.7 sigma 2.2
16 85 +/- 48 --> 1.8 sigma 8.5
17 69 +/- 56 --> 1.2 sigma 2.2
18 -119 +/- 104 --> -1.1 sigma 1.0
19 85898 +/- 804 -->106.8 sigma <-- 1.1
(distances in micrometers; momenta in GeV/c)

Figure 7.1(c)

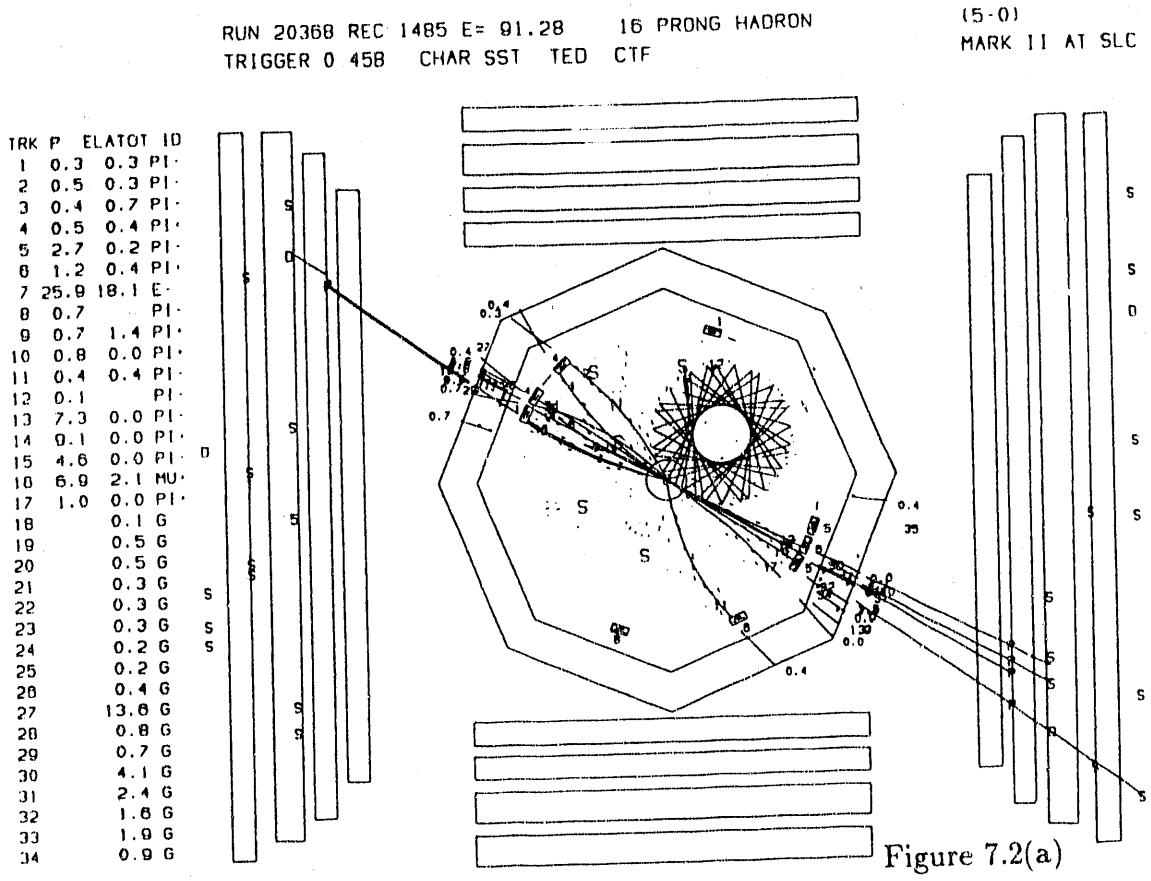

Figure 7.2(a)

Figure 7.2: Lepton-tagged hadronic Z-decay event shown in the r-ϕ plane with (a) charged tracks, neutral showers and muon-chamber hits; (b) charged tracks, DCVD hits and SSVD hits; and (c) track extrapolations to the interaction point. Track number 7 (isolated e^-) has $p = 24$ GeV/c, $p_t = 1.9$ GeV/c, $r_{\rm min} = 0.60$ and $r_{\rm sum} = 0.91$. Track number 16 (μ^+) has $p = 6.9$ GeV/c, $p_t = 0.7$ GeV/c, all four associated hits $< 1.0\sigma$ from the DC track extrapolation and a fourth-layer hit at $2.2\sigma_{\rm corr}$ from the path defined by the associated hits in layers 2 and 3. Tracks number 5, 6 and 7 form a secondary vertex.

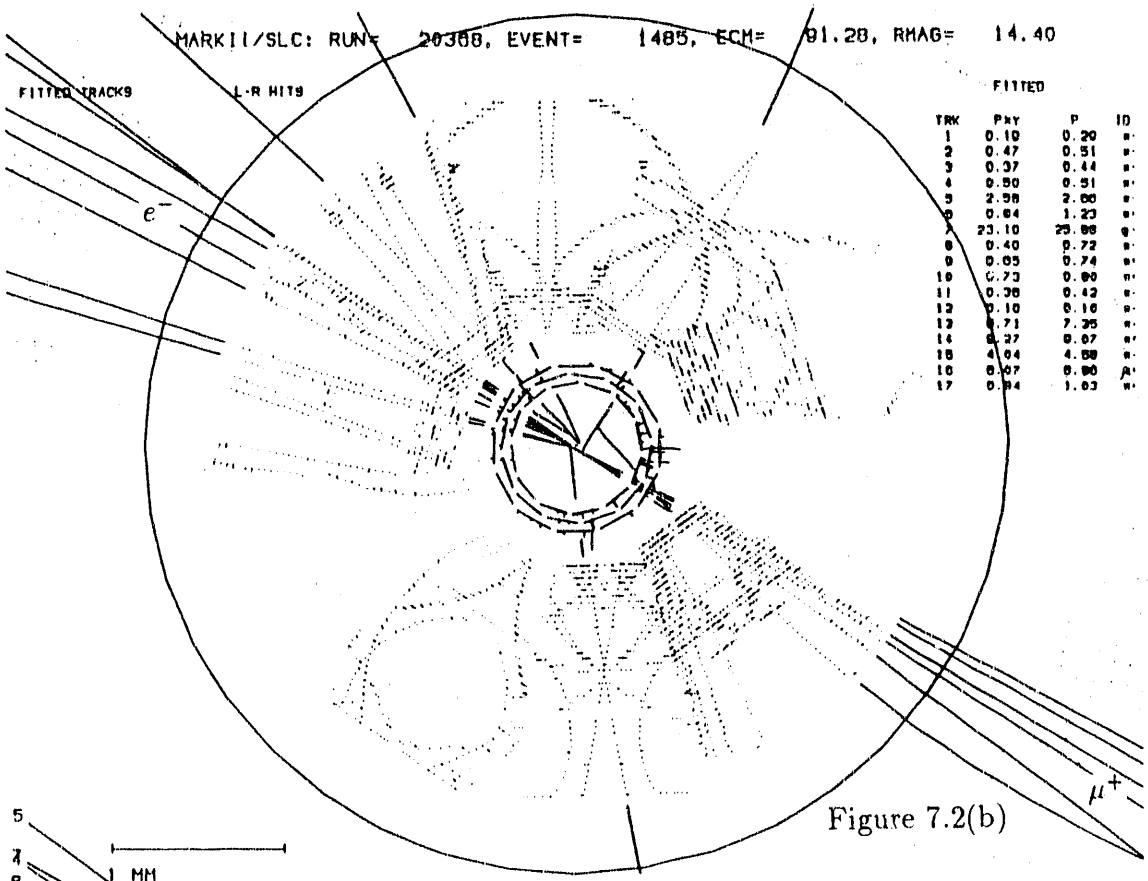

Figure 7.2(b)

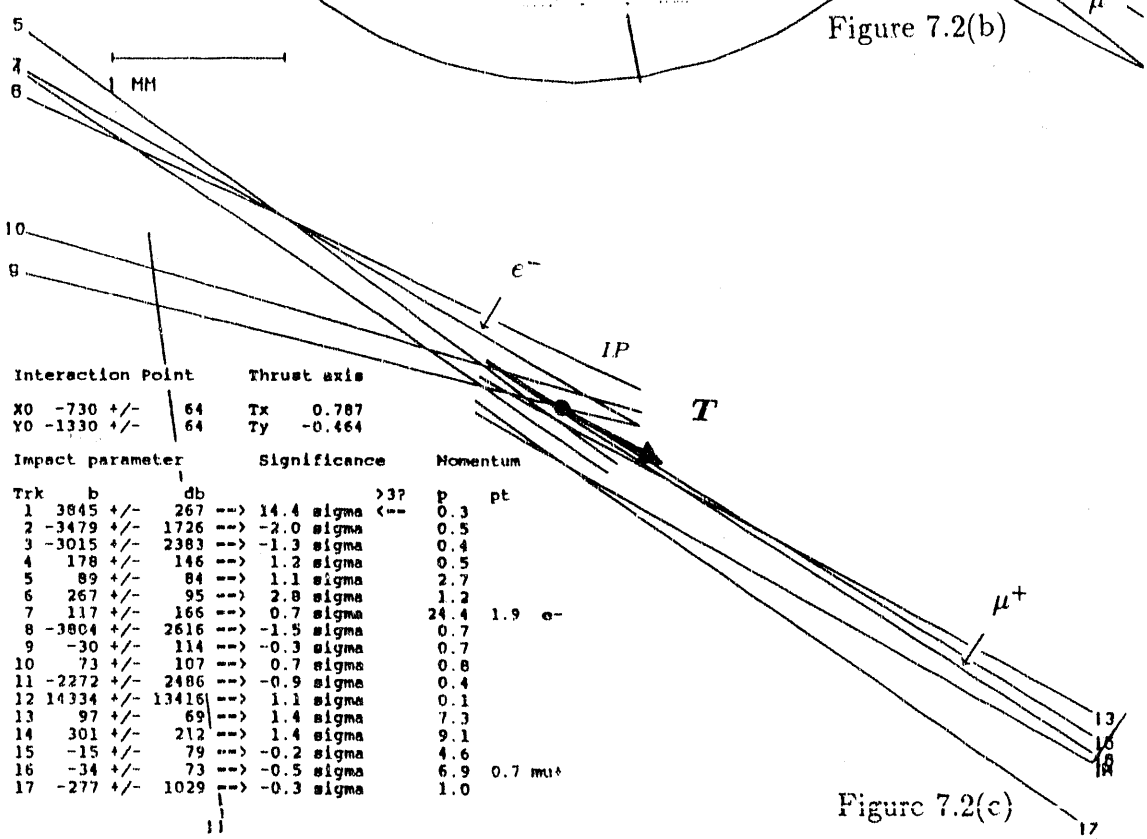

Figure 7.2(c)

Appendix A

Muon Monte Carlo Corrections

To estimate the muon misidentification probability in Chapter 5, we use data to correct the muon Monte Carlo simulation for additional hadron punch-through probabilities and additional proportional-tube inefficiencies. We obtain the corrected punch-through probabilities for the inner three layers from a fit to the distribution of hits for tracks which do not reach the outer layer [Nelson 83b]. The distribution of hits is then corrected for the measured tube inefficiency. The correction procedure outlined in Section 5.3.4 is described in detail here.

The pattern of hits in the four layers of the muon system for each track is represented in the binary variable MUSTAT, for which the least significant bit represents the first layer. E.g., a track penetrating to the third layer without reaching the fourth has MUSTAT $= 0111_2 = 7$. The values of the variable $\mathtt{MUSTAT}_{cr}$ are the same as those of MUSTAT when MUSTAT < 8. For $\mathtt{MUSTAT}_{cr}$ to be ≥ 8, the fourth hit has to be both within 3σ and within $3\sigma_{corr}$. Hence, identified muons have $\mathtt{MUSTAT}_{cr} = 1111_2 = 15$.

The probabilities $P_{add}^{(i)}$ measure how much extra punch through we need to add to each of the inner three layers, $i = 1$–3. Using the fraction $P_{add}^{(i)}$ of the tracks with a given value of MUSTAT, we perform the logical operation MUSTAT OR $\mathtt{MASK}^{(i)}$, where $\mathtt{MASK}^{(1)} = 0001_2$, $\mathtt{MASK}^{(2)} = 0011_2$ and $\mathtt{MASK}^{(3)} = 0111_2$. Thus, $P_{add}^{(1)}$ of the tracks with MUSTAT $= 0$ change to MUSTAT $= 1$, since 0000_2 OR $0001_2 = 0001_2$. Similarly, $P_{add}^{(1)}$ of the tracks with MUSTAT $= 2$ change to MUSTAT $= 3$, since 0010_2 OR $0001_2 = 0011_2$, whereas the tracks with MUSTAT $= 1$ do not change, since they already contain a hit in

the first layer. Starting with k_j tracks having MUSTAT $= j$, we end up with l_j tracks,

$$
\begin{aligned}
l_0 &= [1 - P_{\text{add}}^{(1)} - P_{\text{add}}^{(2)} - P_{\text{add}}^{(3)}]k_0 \\
l_1 &= P_{\text{add}}^{(1)}k_0 + [1 - P_{\text{add}}^{(2)} - P_{\text{add}}^{(3)}]k_1 \\
l_2 &= [1 - P_{\text{add}}^{(1)} - P_{\text{add}}^{(2)} - P_{\text{add}}^{(3)}]k_2 \\
l_3 &= P_{\text{add}}^{(1)}k_2 + P_{\text{add}}^{(2)}[k_0 + k_1 + k_2] + [1 - P_{\text{add}}^{(3)}]k_3 \\
l_4 &= [1 - P_{\text{add}}^{(1)} - P_{\text{add}}^{(2)} - P_{\text{add}}^{(3)}]k_4 \\
l_5 &= P_{\text{add}}^{(1)}k_4 + [1 - P_{\text{add}}^{(2)} - P_{\text{add}}^{(3)}]k_5 \\
l_6 &= [1 - P_{\text{add}}^{(1)} - P_{\text{add}}^{(2)} - P_{\text{add}}^{(3)}]k_6 \\
l_7 &= P_{\text{add}}^{(1)}k_6 + P_{\text{add}}^{(2)}[k_4 + k_5 + k_6] + P_{\text{add}}^{(3)}[k_0 + k_1 + k_2 + k_3 + k_4 + k_5 + k_6] \\
&\cdots \\
l_{15} &= P_{\text{add}}^{(1)}k_{14} + P_{\text{add}}^{(2)}[k_{12} + k_{13} + k_{14}] \\
&+ P_{\text{add}}^{(3)}[k_8 + k_9 + k_{10} + k_{11} + k_{12} + k_{13} + k_{14}].
\end{aligned}
\tag{A.1}
$$

Then we apply the layer inefficiency $\epsilon_{\text{add}} = 0.029$, as calculated in Table 5.6, to each of these MUSTAT populations, obtaining the corrected populations m_j for each MUSTAT value $j = 0$–15,

$$
\begin{aligned}
m_0 &= l_0 + \epsilon_{\text{add}}(l_1 + l_2 + l_4 + l_8) + \epsilon_{\text{add}}{}^2(l_3 + l_5 + l_6 + l_9 + l_{10} + l_{12}) \\
&+ \epsilon_{\text{add}}{}^3(l_7 + l_{11} + l_{13} + l_{14}) + \epsilon_{\text{add}}{}^4 l_{15} \\
m_1 &= (1 - \epsilon_{\text{add}})[l_1 + \epsilon_{\text{add}}(l_3 + l_5 + l_9) + \epsilon_{\text{add}}{}^2(l_7 + l_{11} + l_{13}) + \epsilon_{\text{add}}{}^3 l_{15}] \\
m_2 &= (1 - \epsilon_{\text{add}})[l_2 + \epsilon_{\text{add}}(l_3 + l_6 + l_{10}) + \epsilon_{\text{add}}{}^2(l_7 + l_{11} + l_{14}) + \epsilon_{\text{add}}{}^3 l_{15}] \\
m_3 &= (1 - \epsilon_{\text{add}})^2[l_3 + \epsilon_{\text{add}}(l_7 + l_{11}) + \epsilon_{\text{add}}{}^2 l_{15}] \\
&\cdots \\
m_{15} &= (1 - \epsilon_{\text{add}})^4 l_{15}.
\end{aligned}
\tag{A.2}
$$

To determine the probabilities $P_{\text{add}}^{(i)}$, we perform a fit to the observed MUSTAT distribution, excluding the MUSTAT $= 15$ population since it consists mostly of real muons. For each of the 15 remaining values of MUSTAT $= 0$–14, we form the Poisson

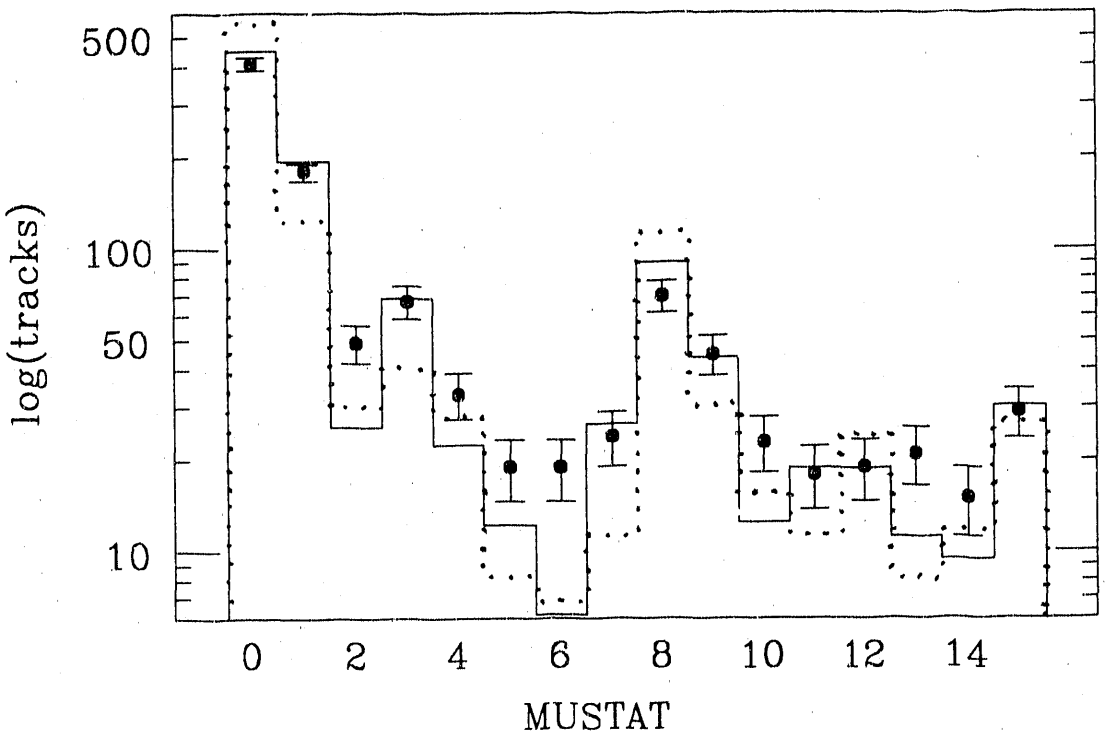

Figure A.1: Result of fit for hadron punch through to pattern of muon hits. Shown are the MUSTAT distributions for tracks satisfying the muon fiducial criteria in the Monte Carlo, before (dots) and after (solid) the corrections, and in the data (circles).

probability,

$$P_j = \frac{r_j^{n_j} e^{-r_j}}{n_j!}, \tag{A.3}$$

corresponding to the Poisson probability of observing n_j tracks with j = MUSTAT, when r_j are predicted. The predictions are the corrected MC populations normalized to the total number of tracks, $r_j = \frac{\sum_{j=0}^{15} n_j}{\sum_{j=0}^{15} m_j} m_j$. We maximize the likelihood

$$\mathcal{L} = \prod_{j=0}^{14} P_j, \tag{A.4}$$

which implicitly depends on the punch-through probabilities $P_{\text{add}}^{(i)}$ through the number of predicted tracks r_j. The fit is performed by minimizing $-\log \mathcal{L}$ using the computer program MINUIT [James 75]. The observed MUSTAT distribution for all tracks is compared to the simulated distributions before and after the fit in Figure A.1. To make sure that the fit yields consistent results, we also fit $P_{\text{add}}^{(i)}$ to the distributions of

$\texttt{MUSTAT}_{cr}$ using all tracks and using only isolated tracks and the results are given in Table A.1.

Fit results	MUSTAT	$\texttt{MUSTAT}_{cr}$	
	all	all	isolated
$P_{add}^{(1)}$	0.147 ± 0.020	0.147 ± 0.020	0.162 ± 0.047
$P_{add}^{(2)}$	0.039 ± 0.011	0.039 ± 0.011	0.045 ± 0.030
$P_{add}^{(3)}$	0.018 ± 0.007	0.021 ± 0.007	0.003 ± 0.030

Table A.1: Additional punch-through probabilities obtained from fits to MUSTAT and $\texttt{MUSTAT}_{cr}$ for all tracks and to $\texttt{MUSTAT}_{cr}$ for the subset of isolated tracks.

To calculate the muon misidentification probability for isolated tracks, we correct the $\texttt{MUSTAT}_{cr}$ distribution for these tracks using the additional punch-through probabilities obtained from the fit to $\texttt{MUSTAT}_{cr}$ for the larger sample containing all tracks,* $P_{add}^{(1)} = 0.147$, $P_{add}^{(2)} = 0.039$ and $P_{add}^{(3)} = 0.021$. Table A.2 shows the corrections to the MC for each $\texttt{MUSTAT}_{cr}$ bin. The resulting $\texttt{MUSTAT}_{cr}$ distribution, indicating the contribution from real muons, is compared with the observed distribution in Figure 5.10.

Out of the 563 isolated real muons in the MC, 501 are identified as muons. The inefficiency correction changes the number of identified muons to 445.4, leading to the identification efficiency of 0.79, as quoted in Section 5.3.3. Similarly, out of the 14245 isolated non-muons in the MC, 91 are misidentified as muons. The punch-through correction adds 11.6 non-muon tracks while the inefficiency corrections subtracts 11.4 non-muon tracks, yielding the essentially unchanged number of 91.2 tracks misidentified as muons and the misidentification probability of 0.006, as quoted in Section 5.3.4. The change in the misidentification probability when results from the other fits in Table A.1 are used is insignificant.

*This fit is to 1419 real muons and 616 hadrons identified as muons in the MC. The number of tracks from additional punch through is +117.7 hadrons and the numbers of tracks from additional inefficiencies are −157.6 muons and −81.5 hadrons. The net effect of these corrections is to multiply the numbers of real muons and hadrons by the overall factors of $(1 - \epsilon_{add})^4 = 0.89$ and $652.2/616 = 1.06$, respectively, as is suggested for the uncorrected p_t spectrum of Figure 5.11 (reproduced in Figure 6.1). The overall correction factor is equal to unity for misidentified isolated hadrons, as is shown here.

j	Before	Punch.	Ineff.	After	r_j	n_j
0	9882	−2045.6	+117.0	7953.4	89.7	82
1	1848	+1341.8	−45.2	3144.5	35.5	32
2	464	−96.0	+33.4	401.4	4.5	10
3	923	+524.4	−66.6	1380.8	15.6	16
4	518	−107.2	−2.6	408.2	4.6	3
5	141	+67.7	+4.3	213.0	2.4	8
6	125	−25.9	+11.5	110.6	1.2	5
7	230	+340.9	−32.2	538.7	6.1	3
8	17	−3.5	+0.0	13.5	0.2	0
9	3	+2.3	+0.4	5.7	0.1	1
10	2	−0.4	+1.5	3.1	0.0	0
11	1	+1.1	+15.8	18.0	0.2	0
12	7	−1.4	+1.4	7.0	0.1	0
13	5	+0.7	+15.5	21.3	0.2	0
14	50	−10.4	+12.7	52.3	0.6	1
15	592	+11.6	−67.0	536.5	6.1	6
$\sum_j$	14808	0.0	0.0	14808.0	167.0	167.0

Table A.2: The Monte Carlo $\texttt{MUSTAT}_{\rm cr}$ distributions for isolated tracks before and after corrections for punch through and inefficiency. The predicted total numbers of tracks r_j are compared to the observed numbers of tracks n_j for each value of $j = \texttt{MUSTAT}_{\rm cr}$.

Appendix B

Solving for the $b\bar{b}$ fraction

The equations used to determine r_b in Section 6.2 are described in detail here.

To solve for the bottom-quark fraction in hadronic Z decays, r_b, we use two numbers observed in the data: the number of hadronic events, $n_{\rm had}$, and the number of hadronic events tagged by an isolated lepton, $n_{\rm tag}$. We have two unknowns, namely the number of produced $udsc$ events and the number of produced $b\bar{b}$ events, which are equivalently expressed as the number of produced hadronic events, n_{udscb}, and r_b. We solve for r_b using four efficiencies obtained from the Monte Carlo, the efficiency for $udsc$ ($b\bar{b}$) events to pass our hadronic event cuts, $\epsilon_{\rm had}^{udsc}$ ($\epsilon_{\rm had}^{b\bar{b}}$), and the efficiency for $udsc$ ($b\bar{b}$) events to be tagged in our high-p_t sample, $\epsilon_{\rm tag}^{udsc}$ ($\epsilon_{\rm tag}^{b\bar{b}}$). We thus have two equations with two unknowns,

$$n_{\rm had} = \epsilon_{\rm had}^{udsc}(1 - r_b)n_{udscb} + \epsilon_{\rm had}^{b\bar{b}} r_b n_{udscb} \tag{B.1}$$

and

$$n_{\rm tag} = \epsilon_{\rm tag}^{udsc}(1 - r_b)n_{udscb} + \epsilon_{\rm tag}^{b\bar{b}} r_b n_{udscb}, \tag{B.2}$$

from which we find the solution

$$r_b = \frac{\epsilon_{\rm had}^{udsc}\frac{n_{\rm tag}}{n_{\rm had}} - \epsilon_{\rm tag}^{udsc}}{\epsilon_{\rm tag}^{b\bar{b}} - \epsilon_{\rm tag}^{udsc} - (\epsilon_{\rm had}^{b\bar{b}} - \epsilon_{\rm had}^{udsc})\frac{n_{\rm tag}}{n_{\rm had}}}. \tag{B.3}$$

Using the values for the efficiencies found in Chapters 4 and 6, we obtain,

$$\begin{aligned} r_b &= \frac{0.858^{+0.016}_{-0.016}\left(\frac{15}{413}\right) - 0.0107^{+0.0038}_{-0.0032}}{0.1008^{+0.0125}_{-0.0121}{}^{+0.0072}_{-0.0072} - 0.0107^{+0.0038}_{-0.0032} - \left(0.883^{+0.016}_{-0.017} - 0.858^{+0.016}_{-0.016}\right)\left(\frac{15}{413}\right)} \\ &= 0.229^{+0.095}_{-0.081}{}^{+0.045}_{-0.044}{}^{+0.020}_{-0.017}, \end{aligned} \tag{B.4}$$

where the errors are, in the order quoted, the statistical errors using the Poisson distribution, the systematic errors from uncertainties in the event efficiencies and the systematic error from the second error in $\epsilon_{\mathrm{tag}}^{b\bar{b}}$, which represents the uncertainty in the B-hadron semileptonic branching ratio. As a function of this branching ratio, $\epsilon_{\mathrm{tag}}^{b\bar{b}} = 0.7150 \cdot B(B \to Xl\nu) + 0.0221$. We factor out the dependence on the assumed branching ratio $B(B \to Xl\nu) = 11\% \pm 1\%$ by forming the product $B(B \to Xl\nu) \cdot r_b = 0.0252^{+0.0105\ +0.0050\ +0.0002}_{-0.0089\ -0.0049\ -0.0003}$.

The measured number of produced $b\bar{b}$ events in the data, $n_{b\bar{b}} = 110^{+46}_{-39} \pm 23$, where the first errors are statistical and the second is systematic.

Appendix C

The Bottom-quark Cross Section

After a description of the radiatively corrected e^+e^- annihilation cross section near the Z pole, we show here the alternate method of calculating $\Gamma(Z \to b\bar{b})$ mentioned in Section 6.3. We also estimate the peak $b\bar{b}$ cross section.

We determine the Z-boson partial width into bottom hadrons $\Gamma(Z \to b\bar{b})$ from the measurements of the average center-of-mass energy (E_i) and integrated luminosity ($\mathcal{L}_i$) for each energy-scan point (i), and the total number of produced $b\bar{b}$ events ($n_{b\bar{b}}$). With average values for M_Z, Γ_Z and $\Gamma(Z \to e^+e^-)$ inserted into the radiatively corrected Breit-Wigner Z^0 line-shape formula for $\sigma(E)$, we solve for $\Gamma(Z \to b\bar{b})$ using $n_{b\bar{b}} = \sum \sigma(E_i) \cdot \mathcal{L}_i$.

C.1 Cross Section for $e^+e^- \to Z \to b\bar{b}$

An analytic formula for the radiative corrections is obtained [Cahn 87] by substituting the Breit-Wigner resonance

$$\sigma_0(E) = \sigma_{\max} \frac{\Gamma_Z^2/4}{(E - M_Z)^2 + \Gamma_Z^2/4} \tag{C.1}$$

with

$$\sigma_{\max} = \frac{12\pi}{M_Z^2 \Gamma_Z^2} \Gamma(Z \to e^+e^-)\Gamma(Z \to b\bar{b}), \tag{C.2}$$

into

$$\begin{aligned} \sigma(E) &= \left(1 + \tfrac{3t}{4}\right) t \int_0^E \tfrac{dk}{k} \left(\tfrac{2k}{E}\right)^t \\ &- \sigma_0(E^2 - 2kE) t \int_0^E \tfrac{2dk}{E} \left(1 - \tfrac{k}{E}\right) \sigma_0(E^2 - 2kE), \end{aligned} \tag{C.3}$$

where k is the energy radiated by photons, and where the strength of the radiative corrections is characterized by

$$t(E) = \frac{2\alpha}{\pi}\left(\ln\frac{E^2}{m_e^2} - 1\right), \tag{C.4}$$

with the typical value $t(M_Z) = 0.108$. The radiatively corrected cross section

$$\begin{aligned}\sigma(E) &= \left(1+\tfrac{3t}{4}\right)\left(\tfrac{\Gamma_Z}{M_Z}\right)^t \tfrac{\pi t}{\sin \pi t}\left(1+\lambda^2\right)^{(t-1)/2} \\ &\times \sin\left[(1-t)\arccos\left(\tfrac{-\lambda}{(1+\lambda^2)^{1/2}}\right)\right]\sigma_{\max} \\ &- \tfrac{t\Gamma_Z}{E}\left(\arctan\tfrac{2M_Z}{\Gamma_Z} + \arctan\lambda\right)\sigma_{\max},\end{aligned} \tag{C.5}$$

where $\lambda = 2(E - M_Z)/\Gamma_Z$. The correction due to initial-state radiation is large, as can be seen in Figure C.1, which compares σ_0 to $\sigma(E)$.

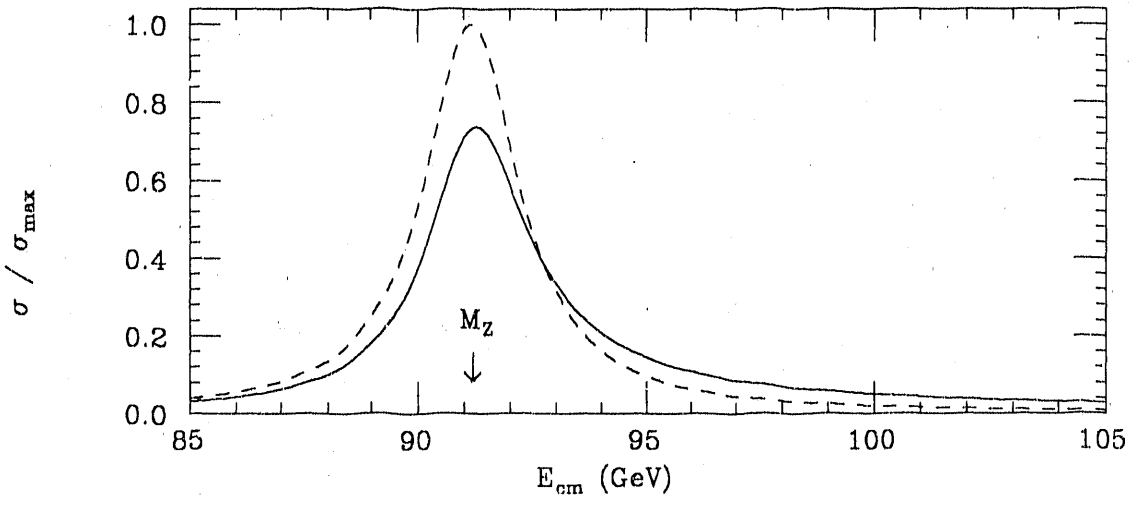

Figure C.1: The Breit-Wigner (dashed) and the radiatively corrected (solid) cross sections divided by the maximum uncorrected value.

C.2 Measuring $\sigma_{\max}(Z \to b\bar{b})$

Using the measured values for $\mathcal{L}_i$ and the calculated values for $\sigma(E_i)$ listed in Table C.1, we find

$$\Gamma(Z \to b\bar{b}) = \frac{n_{b\bar{b}}}{\left(\frac{\sum_i \sigma(E_i)\cdot\mathcal{L}_i}{\Gamma(Z\to b\bar{b})}\right)} = \frac{110^{+46}_{-39} \pm 23}{282 \pm 14\ \mathrm{GeV}^{-1}} = 0.39^{+0.16}_{-0.14} \pm 0.08\ \mathrm{GeV}, \tag{C.6}$$

i	E_i (GeV)	$\mathcal{L}_i$ (nb^{-1})	$\delta\mathcal{L}_i^{\mathrm{stat}}$ (nb^{-1})	$\sigma(E_i)/\sigma_{\mathrm{max}}$	$\sigma(E_i)\cdot\mathcal{L}_i/\sigma_{\mathrm{max}}$ (nb^{-1})	$\sigma(E_i)\cdot\mathcal{L}_i$
3	89.24	0.672	0.049	0.2119	0.142	1.29
5	89.98	0.776	0.054	0.3687	0.286	2.60
10	90.35	2.944	0.106	0.4911	1.446	13.14
2	90.74	1.214	0.067	0.6318	0.767	6.97
7	91.06	4.101	0.128	0.7184	2.946	26.78
8	91.43	4.194	0.134	0.7281	3.054	27.76
4	91.50	1.262	0.070	0.7198	0.908	8.26
1	92.16	0.595	0.050	0.5412	0.322	2.93
9	92.22	3.098	0.112	0.5229	1.620	14.73
6	92.96	1.111	0.069	0.3444	0.382	3.48
$\sum_i$		19.964	0.283	5.2783	11.873	107.93

Table C.1: Measured luminosities [Abrams 89d] and calculated cross sections (Equation C.5). The maximum cross section (Equation C.2) is calculated using the average of measurements by Mark II at SLC and by ALEPH, DELPHI, L3 and OPAL at LEP, $M_Z = 91.17\pm0.03$ GeV/c^2, $\Gamma_Z = 2.50\pm0.02$ GeV and $\Gamma(Z \to e^+e^-) = 0.0840\pm0.0009$ GeV [Fernandez 90] together with the standard-model value $\Gamma(Z \to b\bar{b}) = 0.383$ GeV (Table 1.2). The expected number of events divided by $\Gamma(Z \to b\bar{b})$ is 282 ± 14 GeV^{-1}, where the error includes the uncertainties from the averaged Z-boson resonance parameters and the measurements of the luminosity. For the uncertainty in the luminosity, we have used the error in the total luminosity, $\mathcal{L} = 20.0\pm0.9$ nb^{-1}, which is dominated by an overall error of 4.1% due to the SAM detector resolution, statistics in the precise region of the SAM and unknown radiative corrections [Harral 90].

where the second error is the combined systematic error dominated by the uncertainties in $n_{b\bar{b}}$ calculated in Appendix B. By comparison, we found in Section 6.3 that $\Gamma(Z \to b\bar{b}) = r_b \cdot \Gamma(Z \to \mathrm{had}) = 0.40^{+0.17}_{-0.14}{}^{+0.09}_{-0.08}$ GeV. The maximum cross section in the absence of radiative corrections is $\sigma_{\mathrm{max}} = 9.2^{+4.4}_{-3.8}$ nb, in good agreement with the standard-model value of 9.1 nb.

Bibliography

[Aarnio 86] P. A. Aarnio *et al.*, CERN–TIS–RP/168, January 1986 (unpublished).

[Aarnio 89] P. A. Aarnio *et al.*, Phys. Lett. **231B**, 539 (1989).

[Abe 89a] F. Abe *et al.*, Phys. Rev. Lett. **62**, 1005 (1989).

[Abe 89b] F. Abe *et al.*, Phys. Rev. Lett. **63**, 720 (1989).

[Abe 90] F. Abe *et al.*, Phys. Rev. Lett. **64**, 142 (1990).

[Abrams 89a] G. S. Abrams *et al.*, Phys. Rev. Lett. **63**, 724 (1989).

[Abrams 89b] G. Abrams *et al.*, Nucl. Instrum. Methods A **281**, 55 (1989).

[Abrams 89c] G. S. Abrams *et al.*, Phys. Rev. Lett. **63**, 1558 (1989).

[Abrams 89d] G. S. Abrams *et al.*, Phys. Rev. Lett. **63**, 2173 (1989).

[Abrams 89e] G. S. Abrams *et al.*, Phys. Rev. Lett. **63**, 2447 (1989).

[Adeva 83] B. Adeva *et al.*, Phys. Rev. Lett. **51**, 443 (1983).

[Adeva 89] B. Adeva *et al.*, Phys. Lett. **231B**, 509 (1989).

[Adeva 90] B. Adeva *et al.*, Phys. Lett. **241B**, 416 (1990).

[Aihara 85a] H. Aihara *et al.*, Z. Phys. C **27**, 39 (1985).

[Aihara 85b] H. Aihara *et al.*, Phys. Rev. D **31**, 2719 (1985).

[Akrawy 89] M. Z. Akrawy *et al.*, Phys. Lett. B **231**, 530 (1989).

[Akrawy 90] M. Z. Akrawy *et al.*, Phys. Lett. B **235**, 389 (1990).

[Alexander 89] J. P. Alexander *et al.*, Nucl. Instrum. Methods A **283**, 519 (1989).

[Albrecht 90a] H. Albrecht *et al.*, Phys. Lett. B **234**, 410 (1990).

[Albrecht 90b] H. Albrecht *et al.*, DESY-90-088, July 1990.

[Althoff 84a] M. Althoff *et al.*, Z. Phys. C **22**, 219 (1984).

[Althoff 84b] M. Althoff *et al.*, Phys. Lett. **146B**, 443 (1984).

[Andersson 83] B. Andersson *et al.*, Phys. Rep. **97**, 31 (1983).

[Arnison 83a] G. Arnison *et al.*, Phys. Lett. **122B**, 103 (1983).

[Arnison 83b] G. Arnison *et al.*, Phys. Lett. **126B**, 398 (1983).

[Aubert 74] J. J. Aubert *et al.*, Phys. Rev. Lett. **33**, 1404 (1974).

[Augustin 74] J.-E. Augustin *et al.*, Phys. Rev. Lett. **33**, 1406 (1974).

[Banner 83] M. Banner *et al.*, Phys. Lett. **122B**, 476 (1983).

[Bagnaia 83] P. Bagnaia *et al.*, Phys. Lett. **129B**, 130 (1983).

[Bartel 87] W. Bartel *et al.*, Z. Phys. C **33**, 339 (1987).

[Behrend 83] H. J. Behrend, Z. Phys. C **19**, 291 (1983).

[Behrends 86] F. A. Behrends, P. H. Daverveldt and R. Kleiss, Comput. Phys. Commun. **40**, 309 (1986).

[Behrends 87] S. Behrends, Phys. Rev. Lett. **59**, 407 (1987).

[Behrends 89] F. A. Behrends *et al.*, in *Z Physics at LEP*, CERN-89-08, edited by G. Altarelli *et al.*, 1989 (unpublished) Vol. I, p. 89.

[Bengtsson 87] M. Bengtsson and T. Sjöstrand, Nucl. Phys. **B289**, 810 (1987).

[Bethke 85] S. Bethke, Z. Phys. C **29**, 175 (1985).

[Bjorken 78] J. D. Bjorken, Phys. Rev. D **17**, 171 (1978).

[Cahn 87] R. N. Cahn, Phys. Rev. D **36**, 2666 (1987).

[Cahn 90] R. N. Cahn, lecture at *The Eighteenth SLAC Summer Institute on Particle Physics*, Stanford, July 16, 1990.

[Cassel 90] David G. Cassel, CLNS–90/1014, August 1990 (to be published in the *Proceedings of the Tenth International Conference on Physics in Collision*, Duke Univ., June 21–23, 1990).

[Chrin 87] J. Chrin, Z. Phys. C **36**, 163 (1987).

[Consoli 89] M. Consoli, W. Hollik and F. Jegerlehner, *Workshop on Z Physics at LEP*, CERN–TH–5527/89, edited by G. Altarelli *et al.*, September 1989 (unpublished).

[Cortes 82] J. L. Cortes *et al.*, Phys. Rev. D **25**, 188 (1982).

[Decamp 89] D. Decamp *et al.*, Phys. Lett. **234B**, 209 (1989).

[Decamp 90] D. Decamp *et al.*, Phys. Lett. **244B**, 551 (1989).

[Durrett 90] D. Durrett *et al.*, SLAC–PUB–5259, May 1990 (to be published in the *Proceedings of the Fifth International Conference on Instrumentation for Colliding Beam Physics*, Novosibirsk, March 15–21, 1990).

[Fernandez 90] E. Fernandez, lecture at *The Neutrino 90 Conference*, Geneva, June 11, 1990.

[Fulton 89] R. Fulton *et al.*, CLNS–89/951, November 1989.

[Fulton 90a] R. Fulton *et al.*, CLNS–90/989, August 1990.

[Fulton 90b] R. Fulton *et al.*, CLNS–90/988, 1990.

[Gan 87] K. K. Gan, Mark II/SLC Note #195, December 1987 (unpublished).

[Gilman 86] F. J. Gilman, in *Proceedings of the Fourteenth SLAC Summer Institute on Particle Physics*, edited by E. Brennan (Stanford, 1986), p. 191.

[Glashow 61] S. L. Glashow, Nucl. Phys. **22**, 579 (1961).

[Glashow 70] S. L. Glashow, J. Iliopoulos and L. Maiani, Phys. Rev. D **2**, 1285 (1970).

[Harral 90] B. D. Harral, Ph.D. Thesis, Johns Hopkins University, August 1990 (unpublished).

[Hasert 73] F. J. Hasert *et al.*, Phys. Lett. **45B**, 138 (1973).

[Hayes 84] K. Hayes, Mark II/SLC Note #73, May 1984 (unpublished).

[Herb 77] S. W. Herb *et al.*, Phys. Rev. Lett. **39**, 252 (1977).

[Hernández 90] Particle Data Group, J. J Hernández *et al.*, Phys. Lett. B **239**, 1 (1990).

[Innocente 90] V. Innocente, lecture at *The Twenty-fifth International Conference on High Energy Physics*, Singapore, August, 1990.

[Jadach 85] S. Jadach and Z. Was, Comput. Phys. Commun. **36**, 191 (1985).

[James 75] F. James and M. Roos, Comput. Phys. Commun. **10**, 343 (1975).

[James 80] F. James and M. Roos, Nucl. Phys. **B172**, 475 (1980),

[Klopfenstein 83] C. Klopfenstein, Phys. Lett. **130B**, 444 (1983).

[Kobayashi 73] M. Kobayashi and T. Maskawa, Prog. Theor. Phys. **49**, 652 (1973).

[Komamiya 90] S. Komamiya *et al.*, Phys. Rev. Lett. **64**, 987 (1990).

[Kral 90] J. F. Kral *et al.*, Phys. Rev. Lett. **64**, 1211 (1990).

[Levman 84] G. Levman, Phys. Lett. **141B**, 271 (1984).

[Lamport 86] L. Lamport, LaTeX: *A Document Preparation System* (Addison-Wesley, Menlo Park, California, 1986).

[Marchesini 84] G. Marchesini and B. R. Webber, Nucl. Phys. **B238**, 1 (1984).

[Marshall 89] R. Marshall, Z. Phys. C **43**, 607 (1989).

[Nelson 83a] M. E. Nelson *et al.*, Phys. Rev. Lett. **50**, 1542 (1983).

[Nelson 83b] M. E. Nelson, LBL–16724, Ph.D. Thesis, October 1983 (unpublished).

[Nelson 85] W. R. Nelson *et al.*, SLAC–265, December 1985 (unpublished).

[Ng 88] C. R. Ng *et al.*, ANL–HEP–PR–88–11, November 1988 (submitted to Phys. Rev. D).

[Ong 87] R. A. Ong, SLAC–320, Ph.D. Thesis, September 1987 (unpublished).

[Ong 88] R. A. Ong *et al.*, Phys. Rev. Lett. **60**, 2587 (1988).

[Pal 86] T. Pal *et al.*, Phys. Rev. D **33**, 2708 (1986).

[Perl 75] M. L. Perl *et al.*, Phys. Rev. Lett. **35**, 1489 (1975).

[Petersen 88] A. Petersen *et al.*, Phys. Rev. D **37**, 1 (1988).

[Peterson 83] C. Peterson *et al.*, Phys. Rev. D **27**, 105 (1983).

[Prescott 78] C. Y. Prescott *et al.*, Phys. Lett. **77B**, 347 (1978).

[Ranft 86] J. Ranft *et al.*, SLAC–TN–86–3, April 1986 (unpublished).

[Salam 68] A. Salam, in *Elementary Particle Theory: Relativistic Groups and Analyticity (Nobel Symposium No. 8)*, edited by N. Swartholm (Almquist and Wiksell, Stockholm, 1968), p. 367.

[Sjöstrand 83] T. Sjöstrand, Comput. Phys. Commun. **28**, 229 (1983).

[Sjöstrand 86] T. Sjöstrand, Comput. Phys. Commun. **39**, 347 (1986).

[Sjöstrand 87] T. Sjöstrand and M. Bengtsson, Comput. Phys. Commun. **43**, 367 (1987).

[Stone 83] S. Stone, in *Proceedings of the 1983 International Symposium on Lepton Photon Interactions at High Energies*, edited by D. G. Cassel and D. L. Kreinick (Cornell Univ., Ithaca, 1983), p. 203.

[Suzuki 77] M. Suzuki, Phys. Lett. **71B**, 139 (1977).

[Wachs 89] K. Wachs, Z. Phys. C **42**, 33 (1989).

[Wagner 90] S. R. Wagner *et al.*, Phys. Rev. Lett. **64**, 1095 (1990).

[Webber 84] B. R. Webber, Nucl. Phys. **B238**, 492 (1984).

[Weinberg 67] S. Weinberg, Phys. Rev. Lett. **19**, 1264 (1967).

[Weinberg 71] S. Weinberg, Phys. Rev. Lett. **27**, 1688 (1971).

[Weinberg 72] S. Weinberg, Phys. Rev. D **5**, 1412 (1972).

[Weber 89] P. Weber, Mark II/SLC Note #244, August 1989 (unpublished).

[Weir 87] A. J. Weir, Mark II/SLC Note #193, December 1987 (unpublished).

[Weir 88] A. J. Weir, Mark II/SLC Note #213, May 1988 (unpublished).

END

DATE FILMED

11 / 28 / 90